Optical Properties of Lead Magnesium Niobate-Lead Titanate (PMN-PT) and Strontium Barium Niobate (SBN) Thin Films

Submitted by

Chan Ka Yi

A Thesis Submitted in Partial Fulfilment of the Requirements

for the Degree of Master of Philosophy in Physics

At

The Department of Applied Physics

The Hong Kong Polytechnic University

October 2004

Certificate of Originality

I hereby declare that this thesis is my own work and that, to the best of my knowledge and belief, it reproduces no material previously published or written nor material which has been accepted for the award of any other degree or diploma, except where due acknowledgement has been made in the text.

_____ (Signed)

CHAN KA YI (Name of student)

ABSTRACT

Epitaxial (1-x)$Pb(Mg_{1/3}Nb_{2/3})O_3$-x$PbTiO_3$ ((1-x)PMN–xPT) films x = 0.1, 0.3, 0.35 and 0.4 grown under different deposition temperatures (630°C to 710°C) were fabricated on MgO substrates using pulsed laser deposition (PLD). X-ray diffraction (XRD), scanning electron microscopy (SEM) and atomic force microscopy (AFM) were employed to characterize the structural properties of these (1-x)PMN–xPT films. Our results show that these films possess excellent structural properties and are cube-on-cube grown on MgO substrates. Spectroscopic ellipsometer (SE) was used to characterize the depth profiles, the microstructural inhomogeneities, including void and surface roughness, refractive indicies and extinction coefficients of the films. In the analysis of the measured SE spectra, a double-layer Lorentz model was adopted to represent the optical properties of the (1-x)PMN–xPT films. On the basis of these results, the effects of PT composition and deposition temperature on the optical properties of (1-x)PMN–xPT were revealed.

Our measurements show that the refractive indices of the (1-x)PMN–xPT films increase with PT contents. This dependence is consistent with our optical transmission measurements which revealed decreasing energy band gaps of the (1-x)PMN–xPT films with increasing PT content. Our ellipsometric measurements show that a maximum refractive index of the (1-x)PMN–xPT films is obtained at a deposition temperature of 670°C. No observable change in the band gap energy for various deposition temperatures is detected. This last feature is also confirmed by our independent optical

transmission measurements. Thus the change in refractive index due to deposition temperature is attributed to the change in structural properties.

$Sr_{0.6}Ba_{0.4}Nb_2O_6$ (SBN60) films of different annealing temperature (200°C to 700°C) and durations (0.5 h to 10 h) were fabricated by the sol-gel technique. Our structural characterizations show that these films are amorphous for annealing temperatures ≤ 500°C, and polycrystalline for annealing temperatures ≥ 600°C. In the analysis of the measured SE spectra, a triple-layer Lorentz model was used to interpret the optical properties of the SBN60 films. SE measurements reveal that the refractive indices of SBN60 films increase with annealing temperature. The increase is more significant at around the crystallization temperature of the films, i.e. between 500°C and 600°C. The extinction coefficients also possess a similar trend showing zero values for amorphous films and large values (for example, 0.1 at 2.5 eV) for films annealed above 600°C. Our results demonstrate that the crystallization of the films has an important influence on the refractive index as well as extinction coefficient. Although crystallization can raise the refractive index of the film because of the film densification, it also promotes scattering due to a larger extinction coefficient. Similar phenomena are confirmed by annealing the films for different durations.

PUBLICATIONS

Tsang W. S., Chan K. Y., Mak C. L. and Wong K. H., *Spectroscopic ellipsometry study of epitaxially grown $Pb(Mg_{1/3}Nb_{2/3})O_3$–$PbTiO_3$/MgO/TiN/Si heterostructures*, Appl. Phys. Lett., **83** (2003) 1599

Chan K. Y., Tsang W. S., Mak C. L., Wong K. H. and Hui P. M., *Effects of composition of $PbTiO_3$ on optical properties of $(1-x)PbMg_{1/3}Nb_{2/3}O_3$-$xPbTiO_3$ thin films,* Phys Rev. B., **69** (2004) 144111

Chan K. Y., Tsang W. S., Mak C. L. and Wong K. H., *Optical study of $0.65PbMg_{1/3}Nb_{2/3}O_3$-$0.35PbTiO_3$ thin films*, J. Euro. Ceram. Soc. (accepted)

ACKNOWLEDGEMENTS

I would like to acknowledge Dr. C. L. Mak, my chief supervisor and Dr K. H. Wong, for their close supervisions, fruitful discussions and enthusiasms in research during the past two years. I would like to express my thanks to Dr. Jeffrey Pang for his assistance with TEM measurements and valuable recommendations.

I am grateful to Mr. W. S. Tsang for his preparation of the (1-x)PMN–xPT films and helpful suggestions on the experiments.

I specially thank my research companions, Miss C. Y. Lam, Mr C. Zhao and Miss Y. Yeung, for their assistances in experiments and helping discussions.

I would also like to thank Mr. M. N. Yeung, Mr. C. S. Lo and Miss Yoyo Yeung for their technical supports throughout my project.

Finally I would like to thank my whole family for their encouragements and supports throughout my research period.

Table of Contents

CHAPTER 1 INTRODUCTION

1.1 BACKGROUND

Numerous ferroelectric materials such as lead zirconate titanate ($Pb(Zr_{1-x}Ti_x)O_3$), lithium niobate ($LiNbO_3$), lithium tantalite ($LiTaO_3$) and potassium dihydrogen phosphate (KDP) have good optical properties for optical device applications. These materials have wide band gaps, good transparencies over visible range, large electro-optical coefficients, high static dielectric constants and large nonlinear optical coefficients. A number of optical devices based on these ferroelectric materials have been developed for laser application as well as optical communication [Glass A. M., 1987; Xu Y., 1991]. Apart from these well-known ferroelectrics, lead magnesium niobate-lead titanate ((1-x)PMN–xPT) and strontium barium niobate (SBNx) have attracted a great deal of attention in optical realm recently.

(1-x)PMN–xPT is a solid solution of $Pb(Mg_{2/3}Nb_{1/3})O_3$ (PMN) and $PbTiO_3$ (PT). It has a very high dielectric constant [Noblanc O. *et al*, 1996], piezoelectric constant [Choi S. W. *et al*, 1989], and electro-optic coefficient [Lu Y. H., Zheung J. J. *et al*, 1999]. The value of effective electro-optic coefficient of 0.67PMN-0.33PT thin films is 1.38×10^{-16} $(m/V)^2$ [Lu Y. H., Zheung J. J. *et al*, 1999]. This value is ever larger than the best value reported for lead lanthanum zirconate titanate (PLZT) thin film (1.0×10^{-16} $(m/V)^2$) [Adachi H. *et al*, 1986]. The maximum dielectric constant of 0.65PMN-0.35PT thin

films reaches 2200 at room temperature at 10 kHz [Tantigate C. *et al*, 1995], which is two folds larger than that of PLZT films [Mah S. B. *et al*, 2000]. Therefore (1-x)PMN–xPT thin films are potential candidates for electro-optic devices [Haertling G. H. *et al*, 1971].

Since the 1980's, both the dielectric [Swartz S. L., 1984] and piezoelectric [Uchino K., 1986] properties of (1-x)PMN–xPT ceramics have been widely investigated. However, research studies focusing on optical properties have seldom been reported. In the 1990's, researchers started to study the optical properties of (1-x)PMN–xPT ceramics, McHenry studied the refractive index of 0.7PMN–0.3PT ceramics [McHenry D. A. *et al*, 1992]. Later Uchino measured the transmittance profile of (1-x)PMN–xPT ($x > 0.14$) ceramics [Uchino K., 1995]. Apart from these studies on (1-x)PMN–xPT ceramics, up to our knowledge, only few publications concerning the optical properties of (1-x)PMN–xPT films have been reported. For example, the propagation loss and its electro-optic coefficient of (1-x)PMN–xPT films grown on sapphire substrates were measured [Lu Y. H., Wang F. L. *et al*, 1999]. Thus, the refractive index and extinction coefficient of (1-x)PMN–xPT films have not been studied. It is of paramount important for us to measure these optical properties.

Similarly, $Sr_xBa_{1-x}Nb_2O_6$ (SBNx) is also ideal for optical applications owing to its extremely large linear electro-optic coefficient (r_{33} = 1340 pm/V) and nonlinear optic coefficient (d_{33} = 12.8 pm/V), strong photorefractive effect, and excellent pyroelectric property [Li S. T. *et al*, 2000; Xu Y. *et al*, 1991]. SBNx is currently being investigated

as a potential material for pyroelectric infrared detector [Beerman H. P., 1971], electro-optics [Prokhorov A. M. *et al*, 1991; Neurgaonkar R. R. *et al*, 1980], photorefractive devices [Neurgaonkar R. R. *et al*, 1986] and piezoelectrics [Jaffe B. *et al*, 1971].

SBNx exhibits tetragonal tungsten-bronze (TTB) type structure with its ferroelectric polar axis along the *c*-direction for $0.25 \leq x \leq 0.75$ [Xu Y., 1991]. On the contrary, strotium niobate (SN) and barium niobate (BN) have different crystal structures of type I and type II orthorhombic structures respectively [Repelin Y. *et al*, 1979]. Above its Curie temperature, SBNx crystal transforms from space group P4*bm* with tetragonal structure into non-polar group $P\bar{4}b2$ monoclinic structure [Xu Y., 1991]. This Curie temperature, T_c, changes approximately linearly with x ($57^{\circ}C \leq T_c \leq 247^{\circ}C$ when $0.75 \geq x \geq 0.25$). Beside Curie temperature, many other physical properties of SBNx also vary with its composition [Xu Y., 1991; VanDamme N. S. *et al*, 1991]. Hence, SBNx films having various compositions are important in different areas of various applications. The main purpose of the present study is to investigate the effects of processing parameters on the optical properties, in particular, refractive index and extinction coefficient of both (1-x)PMN-xPT and SBNx thin films.

1.2 CHARACTERISTICS OF LEAD MAGNESIUM NIOBATE-LEAD TITANATE

PMN (T_c = 256 K) is a well-known lead based relaxor ferroelectrics and a perovskite with complicated composition ($A(B_y'B_{1-y}'')O_3$) [Smolensky G. A., 1970]. On the other hand, PT (T_c = 765 K) is a typical normal ferroelectric material with perovskite structure (ABO_3) [Shirane G. *et al*, 1951].

The microscopic structures and the fundamental origins of the relaxor ferroelectric behavior remain in doubt. It is generally accepted that the relaxor behavior of mixed B-site cation perovskite is related to the B-site chemical ordering. According to Smolensky, different properties between relaxors and normal ferroelectrics are originated from their different order of B site and local composition fluctuations [Smolensky G. A., 1970]. Figure 1.2.1 shows a cubic perovskite structure. For $PbTiO_3$, the B site only has one species (Ti^{4+}). For PMN, two species (Mg^{2+} and Nb^{5+}) are in B (B_y' or B_{1-y}'') site with chemical disorder. The chemical disorder of B site and local composition fluctuations lead to a large fluctuation in Curie temperature. This fluctuation of Curie temperature at different crystal regions results in a diffuse phase transition observed in relaxors.

The properties of relaxors and normal ferroelectrics can be distinguished by several phenomena. Normal ferroelectrics have a long-range spontaneous polarization order

below phase transition temperature (T_c) and a sharp vanishing of this long-rang spontaneous polarization at phase transition. The dielectric constant follows the Curie Weiss law $\varepsilon = \frac{C}{T - T_c}$ above T_c and shows an abrupt anomaly at phase transition. Besides, normal ferroelectrics have optical birefringence below T_c. On the other hand, relaxor ferroelectrics have no long-range spontaneous polarization order and are characterized by diffuse phase transition due to the present of polar nanodomain. This polar nanodomain does not change around the diffuse transition temperature and disappears far above the diffuse transition temperature [Cross L. E., 1987]. This behavior of nonadomain on relaxors leads to a diffuse phase transition in which the phase transition occurs over a large range of temperature. The transition of dielectric constant is diffuse, exhibits a broad maximum and does not follow the Curie Weiss law. The response of dielectric constant shows a markedly frequency dispersion in which the temperature of the maximal dielectric constant (T_m) shifts to a higher temperature and the magnitude of dielectric constant decreases with increasing frequency. Relaxor ferroelectrics are optical isotropic in ferroelectric state.

PMN forms a solid solution with PT where Ti^{4+} on the octahedral site of the perovskite structure replaces Mg^{2+} and Nb^{5+} [Shrout T. R. *et al*, 1990]. Figure 1.2.2 shows the phase diagram of (1-x)PMN–xPT system. (1-x)PMN–xPT combines both the advantages of relaxor PMN and ferroelectrics PT. By changing the content of PT, the maximum dielectric constant occurs at varied temperatures ranging from 258 K to 765 K. Furthermore, the substitution of Ti^{4+} on the B-site of perovskite structure also

gradually changes the polar nanodomains of PMN into a long-range polar ordering or macrodomains [Li J. -F. *et al*, 1996; Newnham R. E. *et al*, 1997], thus the phase transition becomes less diffusive [Park J. H. *et al*, 1995]. From Fig. 1.2.2, when x is below 0.35, (1-x)PMN–xPT exhibits relaxor behavior, and when x is larger than 0.35, (1-x)PMN–xPT transforms from rhombohedral phase to tetragonal phase and this results in normal ferroelectric behavior. At x = 0.35, (1-x)PMN–xPT is at its morphotropic phase boundary (MPB) in which the structure of (1-x)PMN–xPT changes abruptly from rhombohedral to tetragonal with increasing content of PT. The piezoelectric coefficient of (1-x)PMN–xPT is maximal near the MPB region [Choi S. W. *et al*, 1989], as a result of enhanced polarizability arising from the coupling between the rhombohedral and tetragonal phase. The electro-optic coefficient [Lu Y. L., Wang F. L. *et al*, 1999] also has a maximum value at MPB. However, no detail studies on optical properties around MPB have been reported. Therefore, it would be of great interest to study the optical properties of these (1-x)PMN–xPT films near the MPB region.

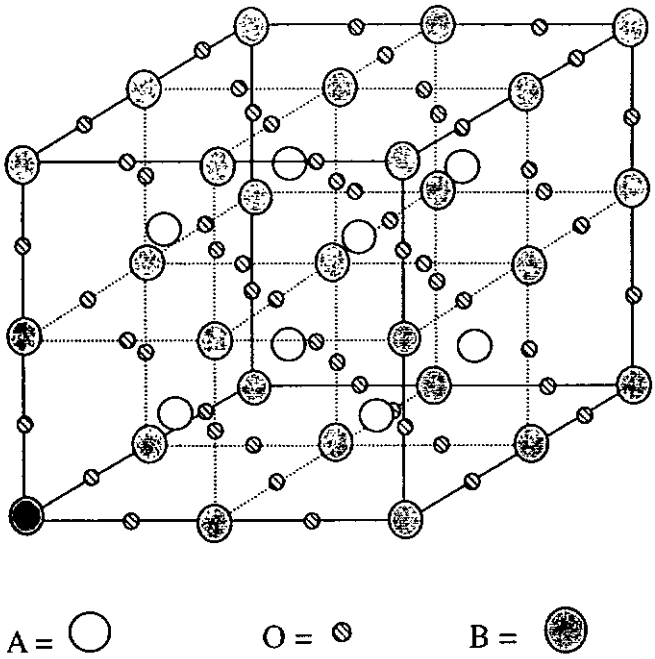

Fig. 1.2.1 Cubic perovskite structure.

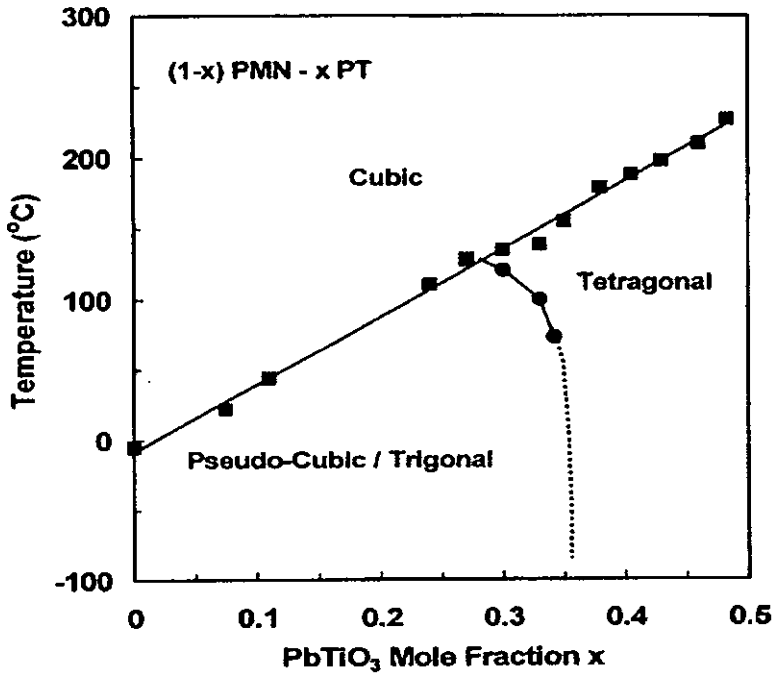

Fig. 1.2.2 The phase diagram of (1-x)PMN–xPT system adapted from Shrout [1990].

1.3 CHARACTERISTICS OF STRONTIUM BARIUM NIOBATE

$Sr_xBa_{1-x}Nb_2O_6$ (SBNx) belongs to the class of tetragonal tungsten-bronze (TTB) type ferroelectric oxides, which is the second largest class of ferroelectrics following perovskite type ferroelectrics. Similar with the perovskite structure, TTB type structure contains oxygen octahedral and maintains a crystallographic structure based on that of the TTB type $K_x WO_3$ and Na_xWO_3 ($x<1$) [Xu Y. *et al*, 1991]. In each TTB unit cell, there are four types of sites, namely, six A sites (with two A_1 sites and four A_2 sites), four C sites, ten B sites (with two B_1 sites and eight B_2 sites) and thirty oxygen ions (at the corners of the octahedral). The site occupancy formula may thus be written as $(A_1)_2(A_2)_4(C)_4(B_1)_2(B_2)_8O_{30}$. The sites A_1, A_2, C, B_1 and B_2 can be either partially or fully occupied by different cations. In the case of SBN60 ($Sr_{0.6}Ba_{0.4}Nb_2O_6$), Nb^{5+} occupies the B_1 and B_2 sites while either Sr ions or Ba ions, or both occupy the A_1, A_2 and C sites. The number of occupied sites depends on the valence and number of these ions in accordance with the requirements of electroneutrality, and on their size in accordance with crystallographic constraints. A schematic diagram showing a projection of the TTB structure on the (001) plane is shown in Fig. 1.3.1.

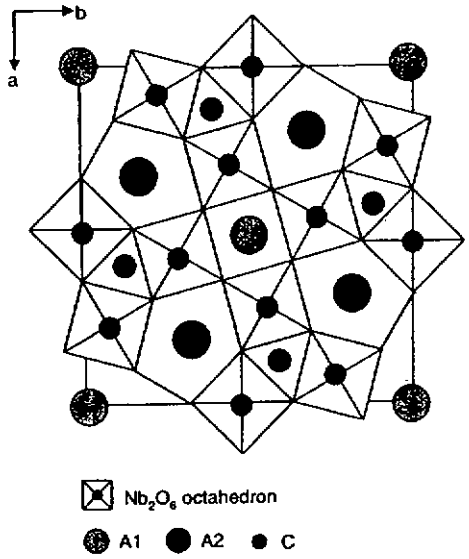

Fig. 1.3.1 Schematic diagram showing a projection of the TTB-type structure along *c*-axis [Jamieson P. B. *et al*].

SBNx solid-solution series ($0.2<x<0.8$) has a TTB-type structure and belongs to the point group 4mm at room temperature. This crystal possesses excellent pyroelectric and linear electro-optic properties with low half-wave voltages [Xu Y. *et al*, 1991]. Owing to its good mechanical and undeliquescent properties, SBNx is an ideal pyroelectric and linear electro-optic material. In addition, SBNx and doped-SBNx crystal can be used in holographic memory and other nonlinear optical devices. This is primarily because of its photorefractive effect (optically induced change of refractive index), in which only 5/6 of the A sites in the SBNx lattice are filled and the vacancies at the other 1/6 A sites act as carrier trapping centers.

By changing the Sr/Ba ratio, the Curie temperature T_c of SBNx can be made to vary in the range from 60°C to 250°C. The TTB type ferroelectric SBNx crystals possess a spontaneous polarization of 32 $\mu C/cm^2$ (Sr/Ba = 75/25) at room temperature and a polar axis along the c-axis of the tetragonal lattice [Glass A. M., 1969 and 1970]. Polycrystalline ferroelectric SBNx thin films (grain size about 2-3 μm) having approximately the same nonlinear properties as SBNx single crystals have been reported [Zhdanov V. G. *et al*, 1967]. For a light beam traversing along a direction perpendicular to the c-axis under a driving electric voltage of 30 V, this modulator was found to operate effectively at several hundred kHz [Jobin Yvon]. The photocurrent effect in SBNx has also been investigated [Zeinally A. H. *et al*, 1978]. This effect is due to excitation of the photocarriers generated during illumination, such that the electrical conductivity and the permittivity of the crystal are changed. According to this

information, SBNx is a potential material for electro-optic device applications. Therefore, it is of great interest for us to also study the optical properties of SBNx.

1.4 FABRICATION METHODS OF LEAD MAGNESIUM NIOBATE-LEAD TITANATE AND STRONTIUM BARIUM NIOBATE FILMS

Since 1990, epitaxial (1-x)PMN–xPT films have been grown by various methods, such as sol-gel spin-on method [Udayakumar K. R. *et al*, 1995], sol-gel dip-coating method [Lu Y. H. Wang F. L. *et al*, 1999] and pulsed laser deposition (PLD) [Tantigate C. *et al*, 1995]. Among these techniques, PLD is a very promising technique for fabricating high optical quality ferroelectric oxide thin films of high density and crystallinity. Advantages of PLD technique are low processing temperature and the ability for fabrication of multilayer structures. Because evaporated particles have high energy, substrate temperature for crystallization can be reduced. In addition, PLD is capable of producing films with good stoichiometry. This is important in the deposition of complex oxide (1-x)PMN–xPT thin films where conventional thermal evaporation and sputtering always lead to non-stoichiometric films. In this project, PLD method was used to fabricate (1-x)PMN–xPT films. In this project, the (1-x)PMN–xPT samples were fabricated by Mr. W. S. Tsang.

Similarly, SBN60 films have been fabricated by various techniques such as sputtering [Wu A. Y. *et al*, 1990], pulsed laser deposition [Thöny S. S. *et al*, 1994], metal organic chemical vapor deposition [Nystrom M. J. *et al*, 1995] and sol-gel process [Chen C. J. *et al*, 1991; Xu R. *et al*, 1990 Xu Y. Wang F. L. *et al*, 1991]. Among these fabrication techniques, the sol-gel process is the most versatile, inexpensive and convenient method. Advantages of sol-gel technique include excellent homogeneity, ease of chemical composition control, high purity, low processing temperature, film uniformity over large area and versatile shaping. In this project, our SBN60 films were fabricated by sol-gel spin-on method.

CHAPTER 2 SPECTROSCOPIC PHASE MODULATION ELLIPSOMETER

2.1 OPTICAL CHARACTERIZATION

There are different experimental techniques using light to measure the thickness and optical properties of thin films. Basically, they are classified into three types of measurements:

a) Photometric Measurement

The amplitudes of incident and reflected or transmitted rays are measured. The main area of application is the determination of optical constant and absorption peaks of films.

b) Interference Measurement

The phase of rays reflected by different surfaces are measured. Using this technique, the film thickness is determined.

c) Ellipsometric Measurement

The ellipticity of the reflected light, the relative change in the amplitude and the phase of the reflected light are measured. Using this technique, both the optical constants and thickness of the films are obtained.

Among these three types of technique, ellipsometric measurement is superior to the other two. The change of ellipticity on reflection is very sensitive to the thickness as well as the presence of inhomogeneity, such as surface and interface roughness, of the

thin films. The sensitivity of thickness measurement using this technique can achieve atomic resolution. It also measures the refractive index and the extinction coefficient simultaneously, so that, unlike the photometric measurement, the Kramers-Kronig relation is not required. Furthermore, in the case of multiple-layer structures, ellipsometer can provide the thickness and dielectric function of each layer.

Ellipsometer is classified into two types, namely, single wavelength ellipsometer (SWE) and spectroscopic ellipsoemeter (SE). SWE uses a laser source and is particularly suited to measure the thickness and refractive index of single transparent layer on a substrate. The simplicity, speed and accuracy make SWE a very important technology for semiconductor metrology. On the other hand, arc lamp of SE provides a light source over a broad range of wavelengths. The strength of SE is to analyze multiple-layer structures and to determine their corresponding optical dispersion functions. In this study, SE was used to study the dispersion function of (1-x)PMN–xPT and SBN60 ($Sr_{0.6}Ba_{0.4}Nb_2O_6$) thin films.

2.2 THEORY

According to Azzam and Bashara, ellipsometer is defined as a measurement of the polarization state of polarized light wave [Azzam R. M. A. *et al*, 1977]. During an ellipsometric experiment, polarized light is allowed to interact with the sample under investigation. The interaction between the sample and the light beam changes the polarization state of the reflected light wave. Measurements of the initial and final

polarization states lead to the determination of the optical properties of the sample. The change of polarization state of the light after reflection depends on the structural and optical properties of the sample. By constructing an appropriate dispersion model for the sample, the change of polarization state of the light upon reflection from the sample can be simulated. Finally, model parameters of interest are determined by fitting process using an optimization algorithm.

In Fig. 2.2.1, two light beams with same frequency and amplitude travel along the same path. One is polarized vertically and the other is polarized horizontally. In this case, the maximum, zero and minimum of the electric field strength of the horizontal wave are displaced from those of vertical wave (in this particular example, the two waves are out of phase by 90°). When the two waves are combined, the tips of the arrows of the resultant wave do not move back and forth in plane. Instead, they move in a manner which, if viewed end-on, would describe a circle. This is called circularly polarized light. Had the phase shift been anything other than 90°, or had the amplitudes not been equal, the tips of the arrow would have appeared to be moving on an ellipse, if viewed end-on, this is referred to as elliptically polarized light. Specifically, when two linearly polarized waves with the same frequency are combined out of phase, the resultant wave is elliptically polarized [Harland G. Tompkins *et al*, 1999].

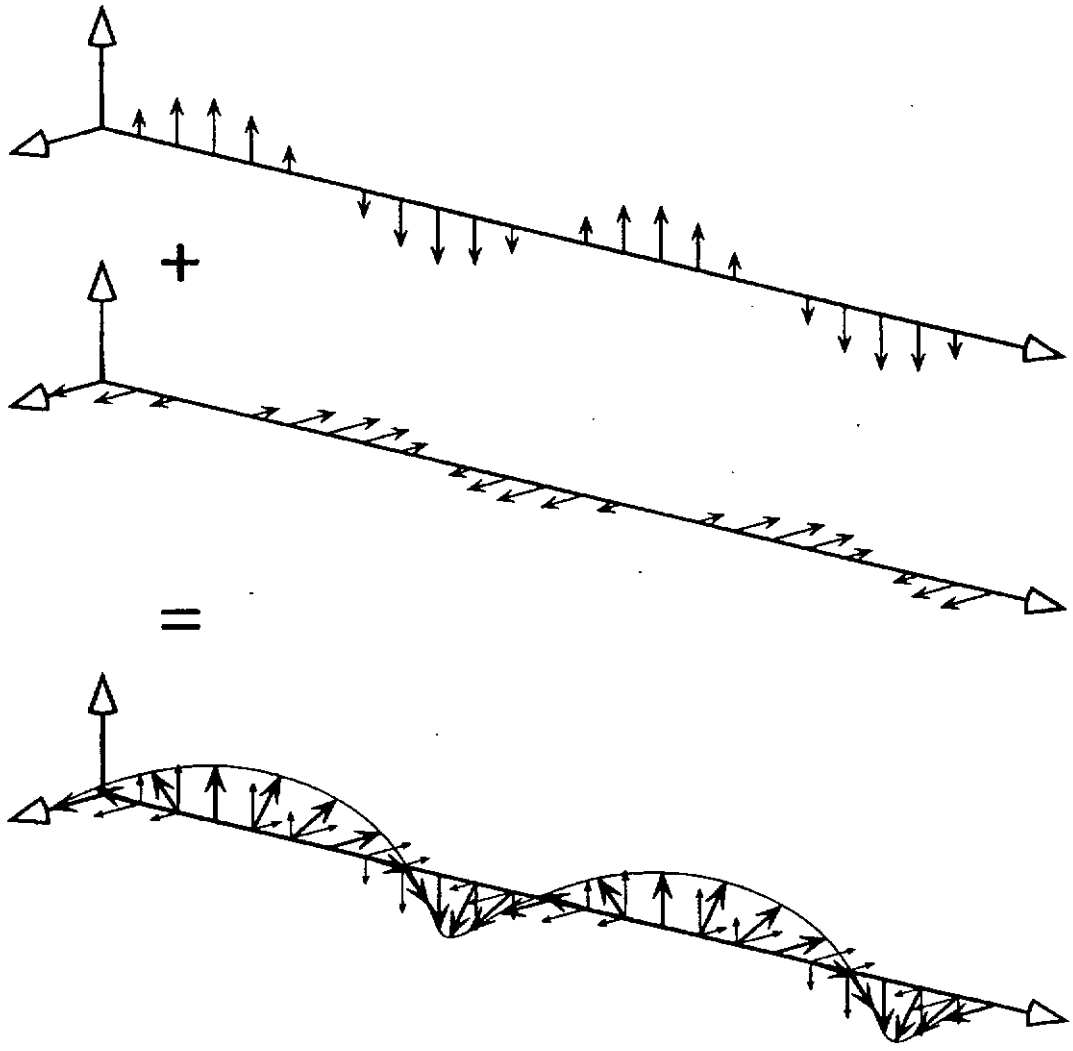

Fig. 2.2.1 Combining two linearly polarized light beams which are a quarter wave out of phase and which have the same frequency and amplitude will produce circularly polarized light [Harland G. Tompkins *et al*, 1999].

To describe the change of polarization, we can resolve the incident light into two orthogonal polarization states as shown in Fig. 2.2.2. It is commonly resolved the incident light into linear polarizations parallel and perpendicular to the plane of incidence. In Fig. 2.2.2, we show the electric waves which are waving in the plane of incidence as E_p and perpendicular to the plane of incidence as E_s. These waves are referred as the p-wave and s-wave, respectively. After reflection, the amplitude and phase of these two components may be changed.

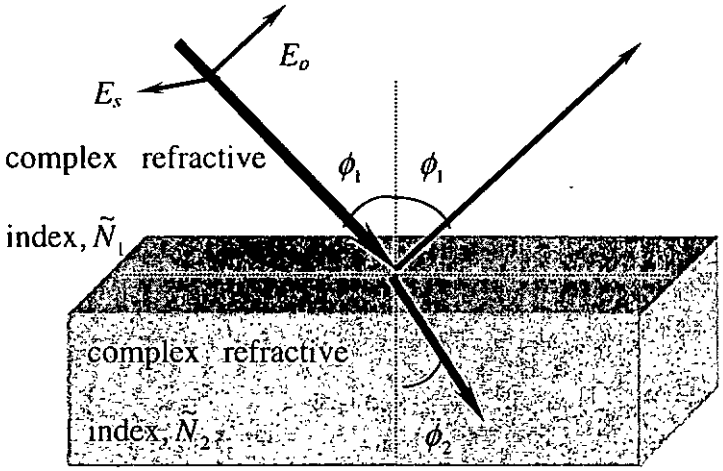

Fig. 2.2.2 The plane of incidence is defined as the plane which contains both the incoming beam and the normal to the surface [Harland G. Tompkins *et al*, 1999].

Frensel reflectance coefficient is defined as the ratio of the intensity of the outgoing light to that of the incoming light. For a single interface, the Frensel coefficients of s- and p-waves are different. They are defined as:

$$r_{12}^{p} = \frac{\tilde{N}_2 \cos\phi_1 - \tilde{N}_1 \cos\phi_2}{\tilde{N}_2 \cos\phi_1 + \tilde{N}_1 \cos\phi_2} \qquad \text{Eq. (2.2.1)}$$

$$r_{12}^{s} = \frac{\tilde{N}_1 \cos\phi_1 - \tilde{N}_2 \cos\phi_2}{\tilde{N}_1 \cos\phi_1 + \tilde{N}_2 \cos\phi_2} \qquad \text{Eq. (2.2.2)}$$

where $\tilde{N}_1$ and $\tilde{N}_2$ are the complex refractive indices of medium 1 and 2 respectively. ϕ_1 represents the incident angle in medium 1 and ϕ_2 represents the refractive angle in medium 2.

When a light beam incident on a thin film (medium 2) which is grown on a bulk substrate (medium 3), more than one interface have to be considered. In Fig. 2.2.3, the resultant reflected wave returning to medium 1 will consist of light (i) which is initially reflected from the first interface (between medium 1 and medium 2), light (ii) which is transmitted by the first interface and reflected from the second interface (between medium 2 and medium 3), and then transmitted by the first interface going in the reserve direction, light (iii) and so on. The light intensity of successive transmission

back into medium 1 has a smaller amplitude than the previous one. This infinite series of partial waves makes up the resultant reflected wave.

From a macroscopic point of view, we are only interested in both the phase and amplitude relationships between the p-wave and the s-wave. The ratio of the amplitude of the outgoing resultant wave to the amplitude of the incoming wave is defined as the total reflection coefficient. For a single film (two interfaces) this is

$$R^p = \frac{r_{12}^p + r_{23}^p \exp(-j2\beta)}{1 + r_{12}^p r_{23}^p \exp(-j2\beta)} \qquad \text{Eq. (2.2.3)}$$

$$R^s = \frac{r_{12}^s + r_{23}^s \exp(-j2\beta)}{1 + r_{12}^s r_{23}^s \exp(-j2\beta)} \qquad \text{Eq. (2.2.4)}$$

where $\beta = 2\pi\left(\frac{d}{\lambda}\right)\tilde{N}_2 \cos\phi_2$. Here r_{12}^p and r_{23}^p, r_{12}^s and r_{23}^s are defined using Eq. 2.2.1 and Eq. 2.2.2 respectively. Since the reflective index $\tilde{N} = n - ik$. When extinction coefficient $k \neq 0$, the Fresnel coefficient, $\tilde{N}_2$ and $\cos\phi_2$ (and hence β) are complex numbers. When $k = 0$, these numbers become real.

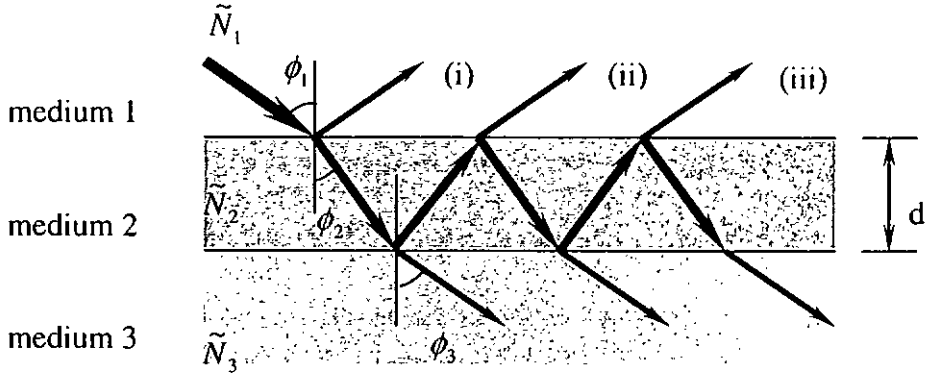

Fig. 2.2.3 Reflections and transmissions for two interfaces. The resultant reflected beam is made up of the initially reflected beam and the infinite series of beams which are transmitted from medium 2 back into medium 1 [Harland G. Tompkins *et al*, 1999].

Figure 2.2.2 shows the p- and s-waves. In general, they are not necessarily in phase. For each reflection, a phase shift may exist between the incoming and the outgoing waves and such shift is not necessarily the same for both the p- and s-waves. The phase difference between the p- and s-waves before reflection is denoted as δ_1 and the phase difference after reflection is denoted as δ_2. Then we define the parameter Δ, called delta, as

$$\Delta = \delta_1 - \delta_2 \qquad \text{Eq. (2.2.5)}$$

In addition to the phase shift, the reflection also induces an amplitude reduction for both the p- and s-waves, and again, it is not necessarily the same for the two waves. We define the quantity Ψ in such a manner that

$$\tan \Psi = \frac{|R^p|}{|R^s|} \qquad \text{Eq. (2.2.6)}$$

Hence, Ψ is the angle whose tangent is the ratio of the magnitudes of the total reflection coefficients.

2.3 INSTRUMENTATION

Figure 2.3.1 shows the schematic diagram of a spectroscopic phase modulated ellipsometer. The ellipsometer can be divided into three parts: polarizing section, optical system and analyzing section.

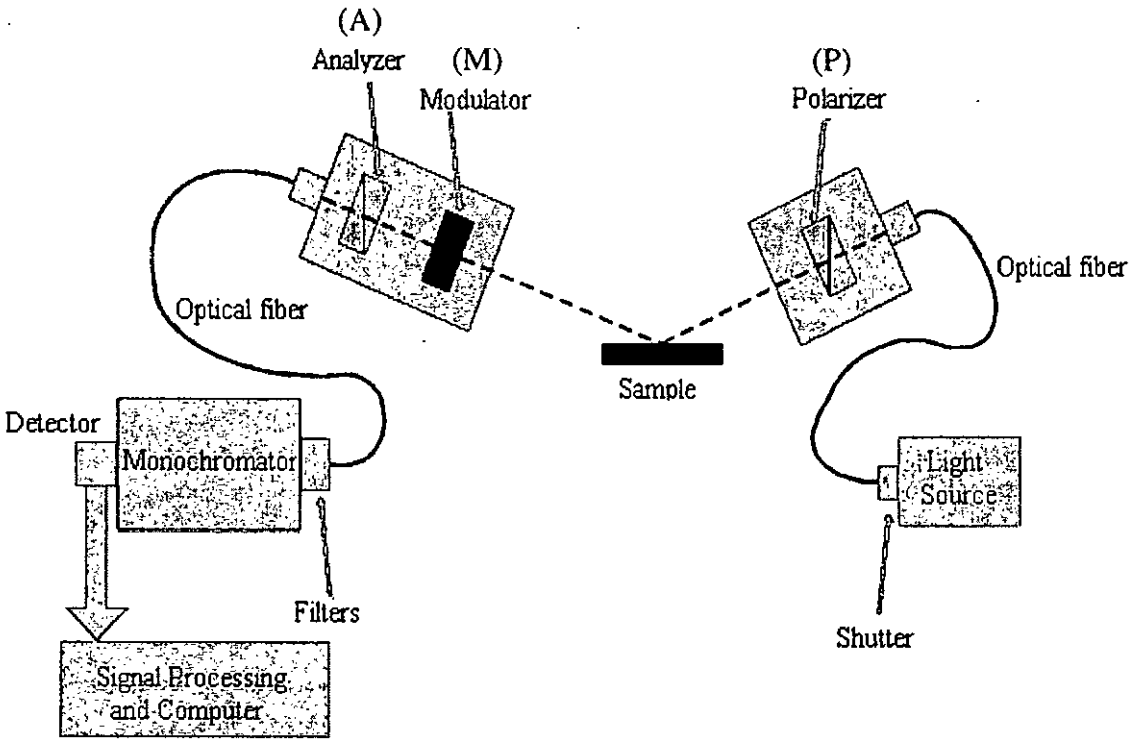

Fig. 2.3.1 Schematic diagram of a spectroscopic phase modulated ellipsometer [Jobin Yvon].

The polarizing section consists of a light source and a linear polarizer, P. The light source is a high pressure 75 W Xenon (Xe) arc lamp. The linear polarizer used is a Calcite Glan polarizer with extinction coefficient less than 10^{-5}. It is mounted in an automatic positioner with accuracy better than 0.05°. The optical system consists of a sample holder. The height and tilted angle of the holder can be adjusted for positioning the sample. The analyzing section consists of a phase modulator, M and a linear analyzer, A followed by a monochromator and a photodetector. The modulator M, which is made of fused silica bar, is used to modify the ellipticity of the polarized light. It is mounted in an automatic positioner with accuracy better than 0.05°. The analyzer used is a Calcite Glan polarizer which has extinction coefficient less than 10^{-5}. The monochromator, which has a grating of 1200 grooves/mm and 0.1 nm resolution at 500 nm is used to disperse the incident light. A photomultiplier tube (PMT) is used as the detector. The voltage of PMT can be adjusted automatically to maintain the intensity of the detected light within a certain level for measurement.

Here, the polarizing section of the instrument controls the polarization state of the incident light. The outgoing light beam from the optical system is analyzed by the analyzing section of the instrument. In the analyzing section, a modulator is used to induce a small modulation of the polarization state of the incident light toward the sample. After passing through the modulator, the ellipticity of the polarization of light beam varies as a function of time (at the modulator frequency of about 50 kHz). The

analyzer followed by the photodetector analyzes the modulated light beam. This detected signal is also varied with function of time.

Generally, ellipsometer measures the traditional ellipsometric angles, Ψ and Δ, directly as a function of energy in experiments. As we have mentioned a spectroscopic phase modulated ellipsometer was used in our measurements. The photoelastic modulator generated a periodic phase shift $\delta(t)$ between orthogonal amplitude components of the transmitted beam. The detected intensity has the general form [Jasperson S. N. *et al*, 1969]:

$$I(t) = I[I_0 + I_S \sin\delta(t) + I_C \cos\delta(t)] \qquad \text{Eq. (2.3.1)}$$

where I is a constant, and

$$\begin{aligned} I_0 &= 1 - \cos 2\Psi \cos 2A + \cos 2(P-M)\cos 2M(\cos 2A - \cos 2\Psi) + \\ &\quad \sin 2A \cos\Delta \cos 2(P-M)\sin 2\Psi \sin 2M \\ I_S &= \sin 2(P-M)\sin 2A \sin 2\Psi \sin\Delta \qquad \text{Eq. (2.3.2)} \\ I_C &= \sin 2(P-M)[\sin 2M(\cos 2\Psi - \cos 2A)\sin\Delta \\ &\quad + \sin 2A \cos 2M \sin 2\Psi \cos\Delta] \end{aligned}$$

For a suitable choice of the angles A, M and P, a simple determination of the ellipsometric angles from I_0, I_S and I_C could be obtained. Throughout the experiment, we set

$$P - M = +45°;\ M = 0° \text{ and } A = +45° \qquad \text{Eq. (2.3.3)}$$

so that Eq. 2.3.2 can be rewritten as

$$\begin{aligned} I_o &= 1 \\ I_S &= \sin 2\Psi \sin\Delta \qquad \text{Eq. (2.3.4)} \\ I_C &= \sin 2\Psi \cos\Delta \end{aligned}$$

Therefore, the angles Ψ and Δ can be determined accurately by measuring I_S and I_C. During the measurements of (1-x)PMN–xPT thin films, the spectral range of experiments is from 0.75 to 3.5 eV. Meanwhile for SBN60 thin films, the range of measurements is between 1.5 and 3.5 eV. The reason for this shorter range for SBN60 is because at low energy range, the signal to noise ratio is poor. The photon energy interval between the data point can be chosen depending on the profile of spectrum. For example, if the profile of spectrum varies rapidly, a smaller interval is needed. In both measurements, the interval of 0.01 eV is adapted.

CHAPTER 3 ANALYTICAL METHODS

Before obtaining the refractive index, thickness and surface roughness of the films, a dispersion model was needed. Based on this model, simulated values of I_S and I_C, namely I_S^{sim} and I_C^{sim} were simulated and compared with the measured quantities. An optimization algorithm was used to refine the values of the thickness and optical constants of the model until the difference between experimental data (I_S and I_C) and the simulated data (I_S^{sim} and I_C^{sim}) was minimized.

3.1 APPROXIMATION OF SURFACE ROUGHNESS

For a microscopically inhomogeneous thin film, it is usually modeled as a mixture of two materials. In our fitting, the surface roughness of the films was modeled as an inhomogeneous film composed of film material and air as shown in Fig. 3.1.1. To calculate the effective complex dielectric function of the inhomogeneity, the Bruggeman effective medium approximation (BEMA) [Bruggeman D. A. G., 1935]:

$$f_a \frac{\varepsilon - \varepsilon_a}{\varepsilon + 2\varepsilon_a} + f_b \frac{\varepsilon - \varepsilon_b}{\varepsilon + 2\varepsilon_b} = 0 \qquad \text{Eq. (3.1.1)}$$

was employed. BEMA assumes a mixture with state of aggregation of each phase on a scale smaller than the wavelength of light, but sufficiently large so that each constituent

retains their bulk dielectric responses. Aspnes and Theeten have shown that BEMA can often yield excellent results for a variety of inhomogeneous films [Aspnes D. E. *et al*, 1979]. In this study, the dielectric constant of the surface layer of the film is modeled by BEMA as an inhomogeneous film composed of film material and air.

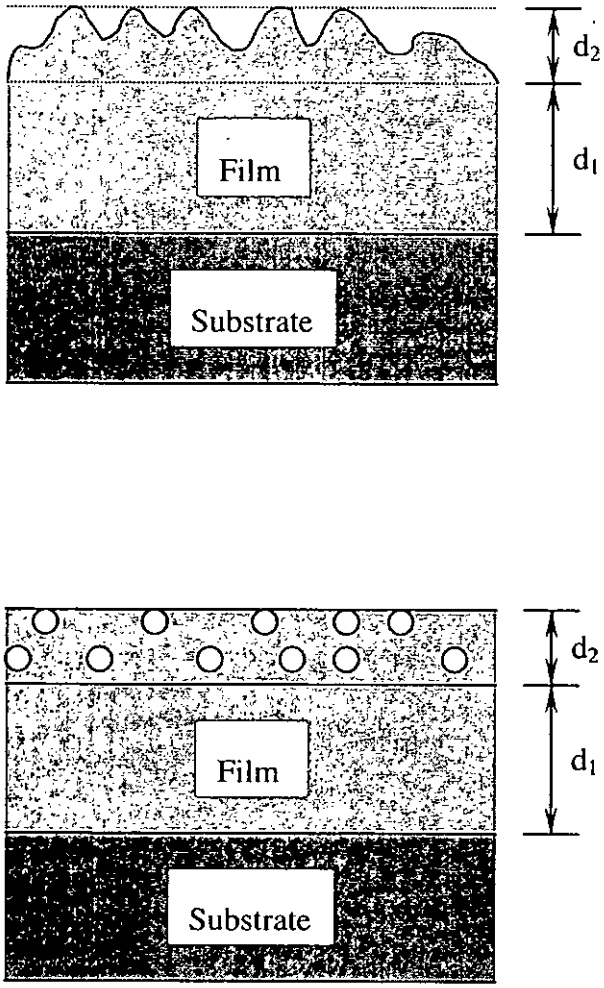

Fig. 3.1.1 Surface roughness of the film is modeled as an inhomogeneous film composed of film material and air (void).

3.2 DISPERSION MODEL: LORENTZ MODEL

In Lorentz model, an atom with electron bounded to the nucleus is represented by a small mass bounded to a large mass by a spring [Frederick Wooten, 1972; Harland G. Tompkins *et al*, 1999]. The motion of an electron bound to the nucleus is then described by

$$m\frac{d^2\vec{r}}{dt^2}+m\Gamma\frac{d\vec{r}}{dt}+m\omega_o^2\vec{r}=-e\vec{E} \qquad \text{Eq. (3.2.1)}$$

where m is the electronic mass, e is the magnitude of electronic charge, $\vec{r}$ is the displacement from equilibrium, and Γ is the damping rate. The electric field $\vec{E}$ acts as a driving force acting on the electron. The term $m\Gamma(d\vec{r}/dt)$ represents viscous damping and provides for an energy loss mechanism. The actual loss mechanism is radiation damping for a free atom, but it arises from various scattering mechanisms in a solid. The damping term in Eq. 3.2.1 is written in the form in which it often appears in describing the electrical conductivity metals. The term $m\omega_o^2\vec{r}$ is a Hooke's law restoring force, where ω_o is the resonant frequency.

Based on this model, the complex dielectric function $\tilde{\varepsilon}$ is obtained [Harland G. Tompkins *et al*, 1999]:

$$\tilde{\varepsilon} = 1 + \frac{4\pi Ne^2}{m} \cdot \frac{1}{\left(\omega_o^2 - \omega^2\right) - i\Gamma\omega} \qquad \text{Eq. (3.2.2)}$$

By defining the complex dielectric function $\tilde{\varepsilon}$ as

$$\tilde{\varepsilon} = \varepsilon_1 + i\varepsilon_2 \qquad \text{Eq. (3.2.3)}$$

then the real and imaginary parts of the dielectric function become:

$$\varepsilon_1 = 1 + \frac{4\pi Ne^2}{m} \cdot \frac{\left(\omega_o^2 - \omega^2\right)}{\left(\omega_o^2 - \omega^2\right)^2 + \Gamma^2\omega^2} \qquad \text{Eq. (3.2.4)}$$

and

$$\varepsilon_2 = \frac{4\pi Ne^2}{m} \cdot \frac{\Gamma\omega}{\left(\omega_o^2 - \omega^2\right)^2 + \Gamma^2\omega^2} \qquad \text{Eq. (3.2.5)}$$

If we consider classical atoms with more than one electron per atom, we can extend the previous results. Let N_j be the density of electrons bounded with resonance frequency ω_j. Then,

$$\tilde{\varepsilon} = 1 + \frac{4\pi e^2}{m} \cdot \sum_j \frac{N_j}{\left(\omega_o^2 - \omega^2\right) - i\Gamma_j \omega} \qquad \text{Eq. (3.2.6)}$$

The frequency dependence of a single oscillator is illustrated in Fig. 3.2.1. Except for a narrow region near ω_o, ε_1 increases with increasing frequency. This is called the normal dispersion. The region near ω_o where ε_1 decreases with increasing frequency is called the anomalous dispersion.

On the other hand, we notice that ε_2 is always positive and approaches zero for values of frequency far from ω_o, where ε_1 may either positive or negative, and approaches the value of one at frequency far from ω_o.

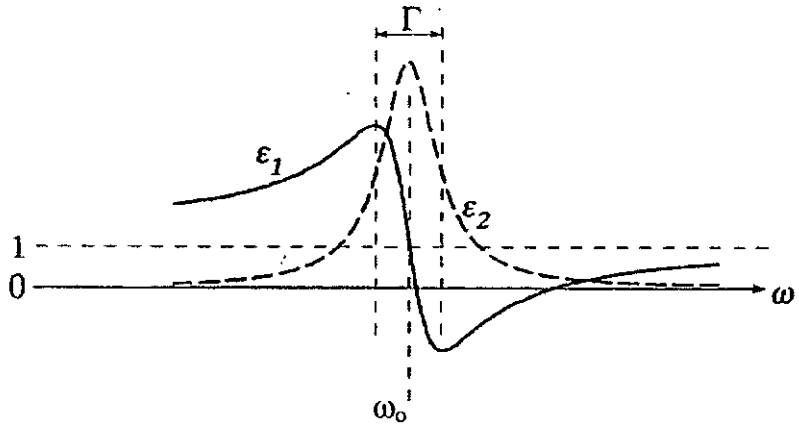

Fig. 3.2.1 The frequency dependence of ε_1 and ε_2 for the Lorentz oscillator [Harland G. Tompkins *et al*, 1999].

Since $\tilde{\varepsilon} = \tilde{N}^2$ Eq. (3.2.7)

where $\tilde{N}$ is the complex refractive index, then we can obtain values for n and k in terms of the values of ε_1 and ε_2, where n and k are the real part and imaginary part of refractive index. Indeed, k is also known as the extinction coefficient. The relationships are

$$n = \sqrt{\frac{1}{2}\left(\varepsilon_1^2 - \varepsilon_2^2\right)^{1/2} + \varepsilon_1} \qquad \text{Eq. (3.2.8)}$$

$$k = \sqrt{\frac{1}{2}\left(\varepsilon_1^2 - \varepsilon_2^2\right)^{1/2} - \varepsilon_1} \qquad \text{Eq. (3.2.9)}$$

It must be recognized that the Lorentz oscillator is an idealization. It is useful to illustrate the qualitative aspects of insulators, semiconductors and conductors where the resonant frequency lies in the spectral range.

3.3 OPTIMIZATION ALGORITHUM

After selecting a suitable dispersion model for the sample, we simulated the ellipsometric data. In order to judge the matching between the experimental and simulated data, a merit function was used as a maximum likelihood estimator. The most common one is the mean-squared error (MSE) which is defined as:

$$MSE = \chi^2 = \frac{1}{N-M-1}\sum_{j}^{N}\left(\left(I_s^{\exp}{}_j - I_s^{sim}{}_j\right)^2 + \left(I_c^{\exp}{}_j - I_c^{sim}{}_j\right)^2\right) \qquad \text{Eq. (3.3.1)}$$

where I_S^{exp} and I_C^{exp} represent experimental data whereas I_S^{sim} and I_C^{sim} are the simulated data. N is the number of data point corresponding to different photon energies at which the measurement is made. M is the number of the unknown parameters. The function exhibits a minimum when the simulated data matches the experimental data as close as possible.

A regression analysis was employed to refine the value of unknown parameters until the merit function was minimized. The Levenberg-Marquadt (LM) algorithm was used for fitting. From this algorithm, the best-fit value and the 90 % confidence limit of each parameter were obtained. Throughout this thesis, all of the modeling parameters are reported in the format as: best-fit value ± 90 % confidence limit. The 90 % confidence limit of a parameter means that if a large number of ellipsometric spectra from the same sample with same conditions were fitted, the confidence interval would contain the true value of the parameter 90 % [Devore J., 1982]. The value of 90 % confidence limit is very helpful for evaluating the quality of the best-fit result. If the 90 % confidence interval for a given parameter is excessively large, then it means that the parameter is strongly varied in a large extent, despite the fact that the value of χ^2 is not changed. This indicates that parameters correlate with each other or this particular parameter does not affect the calculated data. In this case, this parameter was removed from the regression.

Although the LM algorithm has strong advantage of being reasonably insensitive to the starting value of the parameters, it does have difficulties when the starting values are outside reasonable range. Moreover, with poorly selected starting values, the search may terminate in local minima with unacceptably high value of χ^2 and unacceptably final values for the parameters. Therefore, before using LM algorithm to refine the value of unknown parameters in model, the ellipsometric spectra were simulated by some starting values of parameters. The simulated spectra were then compared with experimental one. When the simulated spectrum was close enough to the experimental spectrum, the starting values of the parameters would be used. Besides, in order to check the repeatability of the best-fit parameter values, different sets of starting values were used. If the results of the analyses shown poor repeatability, it was very probable that there is a strong parameter correlation in the model and those best-fit parameter values were not unique.

3.4 GOODNESS OF FIT

In order to evaluate the fitting, four conditions must be fulfilled:

a) A Physically Reasonable Model: A negative or zero thickness and non-physical optical constant dispersion are signs of failure.

b) A Small Value for χ^2: The most obvious check on the quality of the fitting is the value of the final MSE from the fits. Large MSE value is usually an indication of a poor fit to the experimental data. And a small value χ^2 is usually indicative of a good agreement obtained between calculated and experimental values.

c) Reasonable Small Values for the 90 % Confidence Limits: When a parameter is either correlated to another model parameter or it does not affect the calculated data (dummy parameter), the 90 % confidence interval will be large.

d) Low Values for the Cross-correlation Coefficients: Parameters with high cross-correlation coefficients always give a good quality of the fit to the experiment data. However, it is possible that the solution generated by the modeling algorithm may not be unique. There may be more than one set of values for the variable model parameters which yield the same fit to the experimental data. This condition is referred to correlation. This will usually occur when there are too many variable parameters in the models, or when the effects of one parameter exactly offset the effects of another parameter. The strong parameter correlation always accompanies a large 90 % confidence limit of parameter.

CHAPTER 4 EXPERIMENTAL

All (1-x)PMN–xPT thin films were fabricated by pulsed laser deposition (PLD) method while SBN60 ($Sr_{0.6}Ba_{0.4}Nb_2O_6$) thin films were prepared by sol-gel spin-on coating method. Structural properties of these films were examined by X-ray diffractometer (XRD) and transmission electron microscope (TEM). The surface morphology and cross-section of the films were studied by scanning electron microscope (SEM). The surface roughness was measured by atomic force microscope (AFM). Spectroscopic ellipsometer (SE) measurements were carried out by a spectroscopic phase modulated ellipsoemeter to obtain the refractive indices and extinction coefficients of these films. The absorption profiles of these films were measured by a spectrophotometer.

4.1 PULSED LASER DEPOSITION

A typical PLD system is shown in Fig. 4.1.1. A Krypton fluoride (KrF) excimer laser with wavelength of 248 nm (Lambda Physik COMPex 205) was used for thin film ablation. The laser beam was directed and focused into the deposition chamber using a plano-convex lens. The incoming beam was focused onto the rotating target inside the chamber. The windows of the chamber were made of UV-grade fused silica, which allowed up to 90 % transmittance of the beam laser intensity. For film deposition, the chamber was evacuated down to around 10 mTorr using a mechanical rotary pump (ULVAC D-330K) and to a higher vacuum of $5x10^{-7}$ Torr via a cryro-pump (CTI-

CRYOGENICS CRYO-TORR 8). The pressure of the chamber was monitored by a manometer (MKS Baratron Type 122A) in the range from 10 to $1x10^{-3}$ Torr, while for pressure lower than $1x10^{-3}$ Torr, an ionization gauge (ULVAC type WIT) was employed.

The substrate holder was equipped with a heating filament that could be heated up to 750 °C. The heating filament being used was Kanthal wire (25 % chromium, 5 % aluminium, 3 % cobalt and 67 % iron) of 0.559 mm in diameter and the resistance per unit length was 5.1 Ωm^{-1}. Total resistance of the Kanthal wire was 15 Ω. The heating process was controlled by a PID controller (Shimaden SR-19) and a power regulator (PAC25-0321). A K-type (Nickel-Chromium, Nickel-Aluminium) stainless steel shielded thermocouple was employed for monitoring the temperature. The substrates were secured on the holder by silver paint in order to ensure a good thermal contact between the substrate and the holder.

Oxygen was passed through the gas inlet into the deposition chamber. The target was mounted with a rotating shaft through the center. The distance between the target and the substrate holder was fixed at about 5 cm. During deposition, the target holder was rotated continuously to ensure that the surface of the target was evenly ablated and to prevent pitting on the target surface.

Thin (1-x)PMN–xPT films with x = 0, 0.3, 0.35, 0.4 were grown on MgO single crystals. Before deposition, the MgO substrates were immersed in acetone and

degreased by ultrasonic cleaner. The substrates were then adhered on face-plate of the heater with high-temperature silver paste which also acted as a heat conducing medium. All the (1-x)PMN–xPT, films were deposited under 200 mTorr ambient oxygen pressure. The thickness of the films was controlled by deposition time and laser repetition rate.

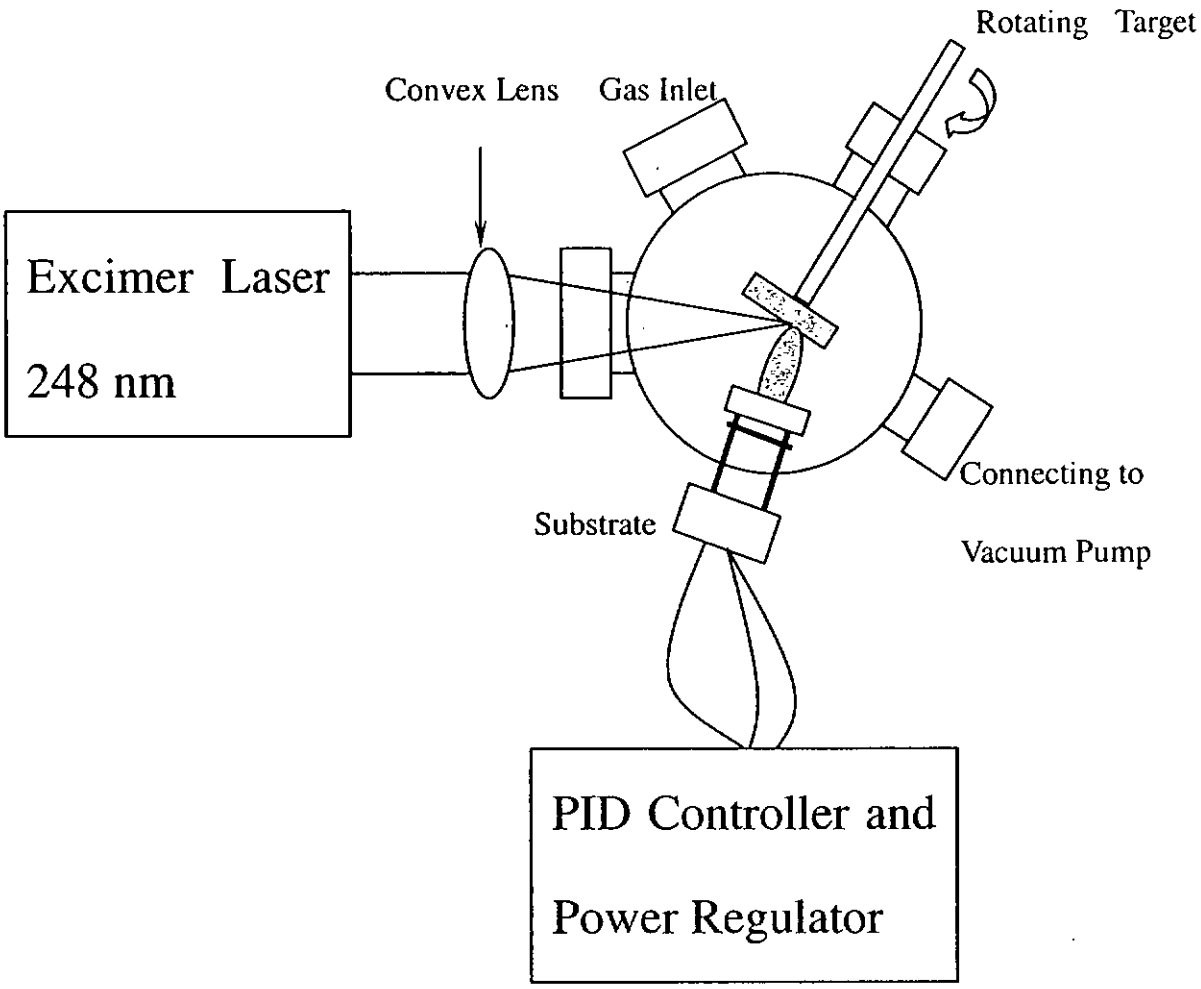

Fig. 4.1.1 Schematic Diagram of a typical PLD Setup.

4.2 SOL-GEL SPIN-ON COATING

Before preparing SBN60 sol, individual metal alkoxide solutions were first produced separately. Firstly, strontium and barium metals were dissolved in 2-methoxyethanol to form strontium alkoxide and barium alkoxide respectively. The 2-methoxyethanol acted as both the solvent and the stabilizer. Niobium(V) chloride ($NbCl_5$) was used to prepare niobium alkoxide by mixing with potassium hydroxide and added into 2-methoxyethanol. KOH was employed to getting rid of the chloride ions. The KCl was precipitated out and was easily separated from the solution by filtration. The three metal alkoxides were then mixed according to the stochiometric ratio. The procedure of the sol-gel processing of SBN60 is shown schematically in Fig. 4.2.1.

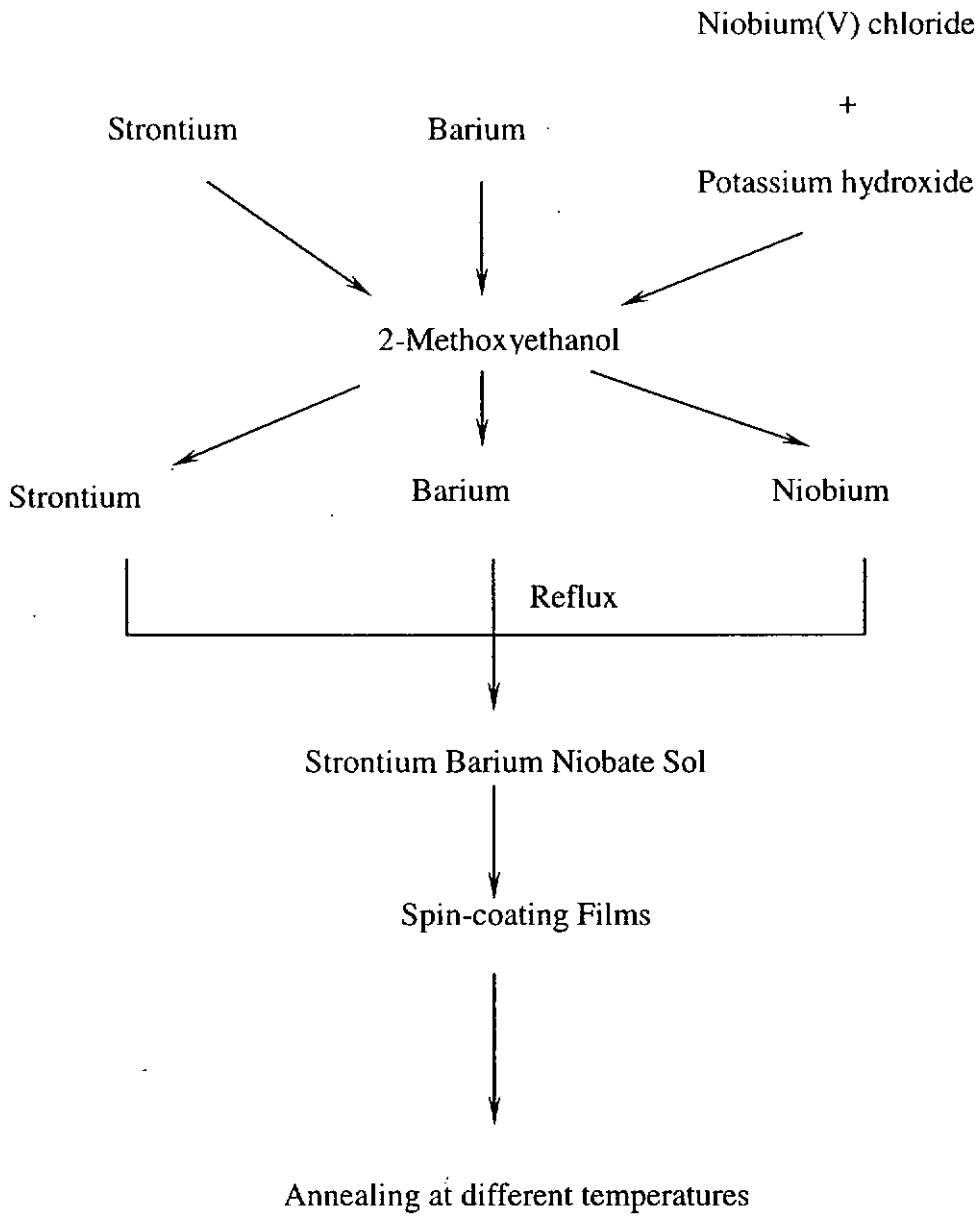

Fig. 4.2.1 A flow chart of preparation route of SBN60 sol and thin films.

To fabricate SBN60 films on 1×1 cm^2 (001)Si substrates, spin-coating technique was used. Initially, Si substrates were cleaned and etched. SBN60 sol of molar concentration of 0.16 M was spin-coated on Si substrates using a spin coater operated at 3000 rpm for 30 s. After drying on a hot plate for several seconds, the films were annealed at a temperature range from 200°C to 700°C with interval of 100°C for 2 hours.

4.3 SAMPLE CHARACTERIZATION AND MEASUREMENTS

4.3.1 X-ray Diffractometry (XRD)

X-ray diffractometry is a common and non-destructive method for characterization of crystal structure. It can be used to determine the atom location of bulk solids, powders or thin films. The XRD system (Philip, X'pert system) was operating both in four-circle and Bragg-Brentano (θ–2θ) geometries. The X-ray used was the K_α radiation of Cu with wavelength of 1.54 Å. The K_β line was filtered off by an appropriate Ni filter. In this project, XRD was performed in several modes of scanning. The θ-2θ scan was used to determine the crystal phase formed with orientation normal to the substrate surface. The out-of-plane orientation of the (1-x)PMN–xPT(200) peaks were examined by ω–scan. A smaller full-width-half-maximum (FWHM) of ω–scan profile indicates a better quality in orientation. The XRD ϕ–scan was performed to confirm the epitaxial growth of the films.

4.3.2 Scanning Electron Microscopy (SEM)

The surface morphology and cross section of the films were investigated by field emission scanning electron microscopy (JEOL 6335F). The film thickness of the films was determined from the cross section image. The principle maximum amplification of the SEM was about 300,000. Under this amplification, grains size of about 20-30 nm were barely resolved.

4.3.3 Atomic Force Microscopy (AFM)

AFM (Burleigh, Metris-2000) was used to characterize the surface morphology of our thin films especially in the determination of lateral grain size and the surface roughness of the films. Throughout the studies, scan area of 0.5x0.5 μm^2 in contact mode was used.

4.3.4 Spectrophotometer

The transmittance of (1-x)PMN–xPT transparent films was measured by a spectrophotometer (Shimadzu UV – 2101 PC). The ratio of transmitted light intensity through the films to the incident light was measured as a function of wavelength.

Shimadzu UV – 2101 PC is a double-beam spectrophotometer. During the experiment, a beam splitter was used to split the incident beam into two beams of equal intensity

with equivalent optical path as shown in Fig. 4.3.4.1. One of these beams passed through a bare MgO substrate as reference.

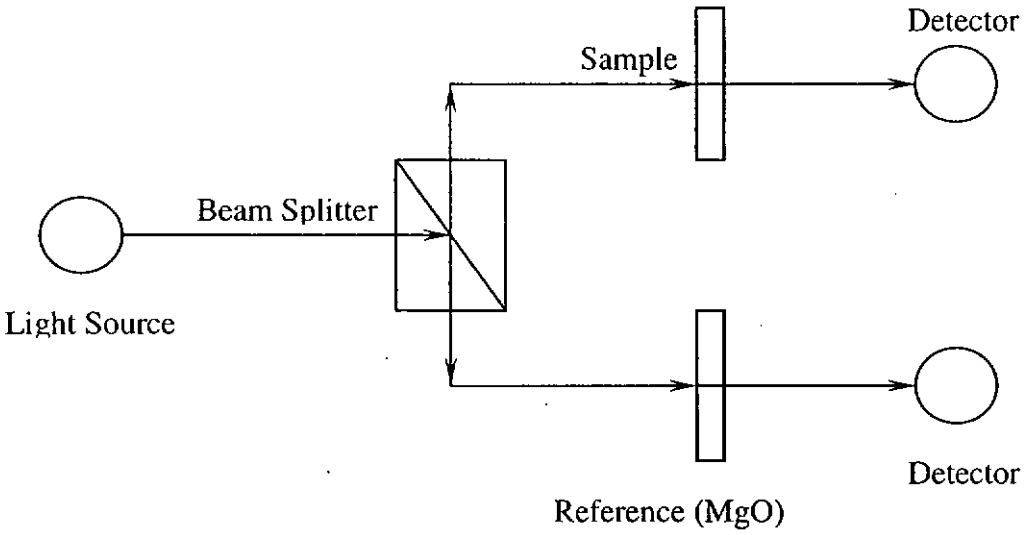

Fig. 4.3.4.1 The schematic diagram of a double-beam spectrophotometer.

4.3.5 Transmission Electron Microscopy (TEM)

TEM specimens were prepared by the method of grinding and ion milling method. The thin films samples were first cut into small rectangular pieces of dimension of 3x3 mm^2. Two pieces of rectangle were glued together using G1 epoxy (Gatan, Inc.) with the thin films facing each other. The slap was grinded mechanically to 30 μm thick using a series of abrasive papers from 100 μm to 20 μm. The slap was then glued on a 3 mm diameter copper supporting grid. The polishing was carried out using diamond polishing films of 6 μm, 3 μm and 1 μm until the silicon substrate turns to red when observed under an optical microscope using transmitted light, indicating a total thickness of about

8 μm. The samples were milled by Ar ions using a Gatan PIPS machine operated at 5 kV. When a hole was formed at the junction of the films, the energy was reduced to 2 kV to minimize the amorphous effect induced by high energy Ar ion. TEM studies were carried out on a JEOL JEM-2011 microscope operated at 200 keV.

CHAPTER 5 OPTICAL PROPERTIES OF LEAD MAGNESIUM NIOBATE-LEAD TITANATE THIN FILMS

Refractive index is one of the fundamental optical properties of films. Before measuring other optical properties of films or designing optical devices, it is important to determine the refractive index of optical films. The refractive index of thin films is directly correlated to material composition, density, microstructure and crystallinity. Among these factors, density, microstructure and crystallinity of the films are affected by deposition temperature. In this chapter, the effects of composition ratio and deposition temperature on the refractive index of (1-x)PMN–xPT films are investigated by spectroscopic ellipsometer.

5.1 COMPOSITION DEPENDENCE

As we have mentioned before, the maximum electro-optic coefficient of (1-x)PMN-xPT is at its MPB region (x about 0.35). For application point of view, it is of great interest to investigate the change of refractive index around this MPB region. Till now, only the refractive indices of PMN single crystal [McHenry, D. A. *et al*, 1990], 0.7PMN-0.3PT ceramics [McHenry D. A., 1992] and $PbTiO_3$ ceramics [Landolt-Börnstein, 1981] have been reported. In these studies, the refractive index of PMN, 0.7 PMN-0.3PT and $PbTiO_3$ were found to be 2.522, 2.598 and 2.668 at 633 nm respectively. Bing further suggested that for (1-x)PMN–xPT family, their refractive indices increase slightly with

$PbTiO_3$ content due to a larger $PbTiO_3$ refractive index [Bing Y. H. *et al*, 2000]. These studies only concentrated on bulk ceramics. Up to our knowledge, the refractive index of thin film (1-x)PMN–xPT has not been reported yet. In this section, results of refractive indices of (1-x)PMN–xPT films with different $PbTiO_3$ content are discussed.

In our studies, (1-x)PMN–xPT films were fabricated on MgO substrates. The two main reasons for choosing MgO as substrates are:

a) A small lattice misfit

MgO single crystal has a lattice constant of 4.2 Å [Nagarajan V. *et al*, 2000] which close to that of (1-x)PMN–xPT (4.02 Å) [Tyunina M. *et al*, 1999]. There is only about 4.7% lattice mismatch between the two materials. Thus eptiaxial films can be fabricated at relatively low deposition temperature. The lattice stress induced in the films can be decreased.

b) A large difference in refractive index

The refractive index of 0.7PMN-0.3PT ceramics is 2.598 at 633 nm [McHenry D. A., 1992], which is much larger than that of bulk MgO (1.734) at 650 nm [Stephens R. E. *et al*, 1952]. A larger refractive index difference between the film and substrate increases the amplitude of oscillations of ellipsometric spectra and enhances the accuracy for determination of thickness and refractive index of the film [Harland G. Tompkins *et al*, 1999].

5.1.1 Fabrication and Structural Characterization

(1-x)PMN–xPT films were grown on MgO single crystal substrate with $PbTiO_3$ content x = 0, 0.1, 0.3, 0.35 and 0.4. Unless stated otherwise, the following conditions for deposition of (1-x)PMN–xPT films were employed in all cases. The substrate temperature was 670°C, the ambient oxygen pressure was 200 mTorr, 3 J/cm^2 laser influence and 6 Hz laser repetition rate were used. The deposition time was 20 min. Then as-grown (1-x)PMN–xPT films were post-annealed at the deposition temperature and oxygen pressure for 10 min. Afterwards, the films were cooled naturally to room temperature.

Figure 5.1.1.1 shows the XRD θ-2θ profiles of the (1-x)PMN–xPT||MgO films with different PT contents. Highly oriented (1-x)PMN–xPT films of perovskite phase are observed in all PT contents. The out-of-plane lattice constants calculated from the (002) diffraction peak of (1-x)PMN–xPT films with x = 0, 0.1, 0.3, 0.35 and 0.4 are 4.03 Å, 4.02 Å, 4.02 Å, 4.02 Å and 4.00 Å, respectively. The XRD ω-scan of 0.7PMN-0.3PT film grown on a single-crystal MgO substrate is shown in Fig. 5.1.1.2. The full-width-half-maximum (FWHM) of the rocking curves for all (1-x)PMN–xPT films are about 0.8°. To give an idea of the instrumentation limit of our XRD machine, the FWHM value for single crystal MgO substrate is ≤ 0.2°. XRD ϕ-scans of the (202)(1-x)PMN–xPT and (202)MgO were performed to confirm the epitaxy of our films. Figure 5.1.1.3 shows a typical ϕ-scan for 0.7PMN–0.3PT film. The peaks of 0.7PMN–0.3PT and MgO are at the same position and separated by 90°. This clearly shows the four-fold

symmetry of both the film and the substrate. Our XRD results indicate that all (1-x)PMN–xPT films are cube-on-cube grown on (001)MgO substrates with an in-plane epitaxial relationship of (001)(1-x)PMN–xPT||(001)MgO.

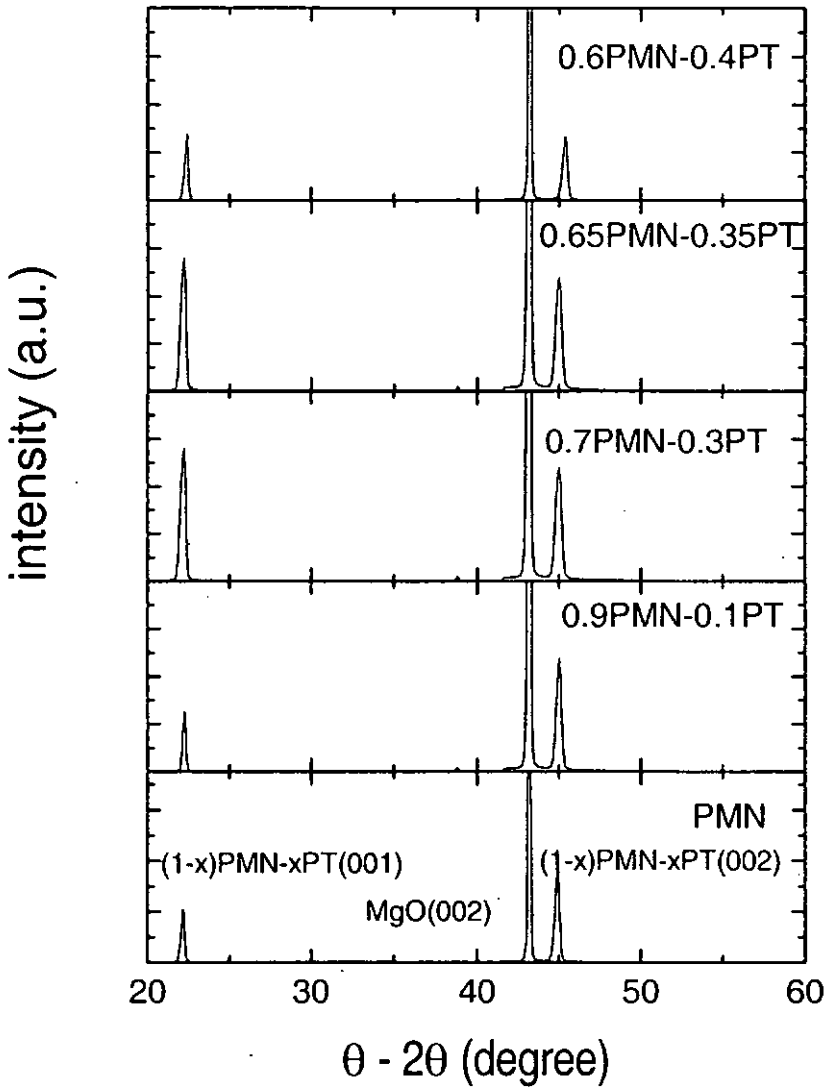

Fig. 5.1.1.1 XRD θ–2θ scans of (1-x)PMN–xPT films with different content of $PbTiO_3$.

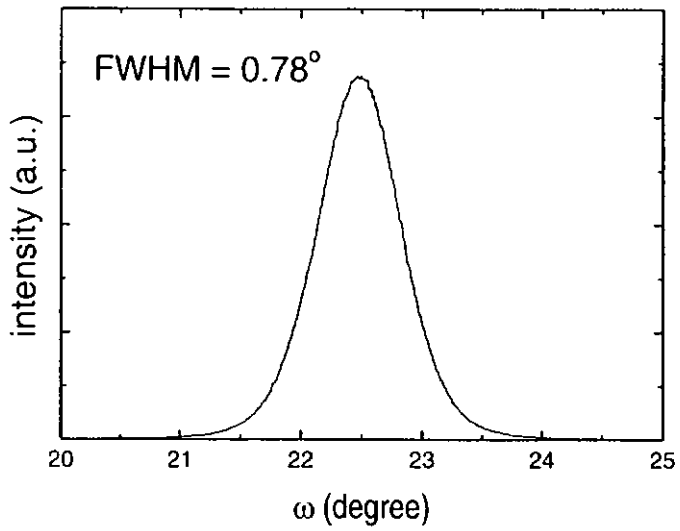

Fig. 5.1.1.2 XRD ω-scan of 0.7PMN-0.3PT film grown on a single-crystal MgO substrate.

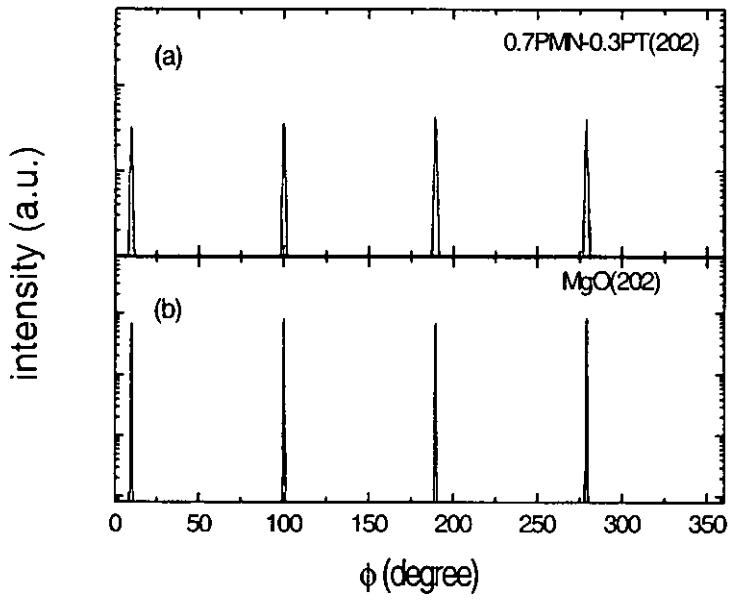

Fig. 5.1.1.3 XRD ϕ–scan of the (a) 0.7PMN-0.3PT(202) and (b) MgO(202).

5.1.2 Ellipsometric Measurement

The SE spectra were measured by a phase modulated spectroscopic ellipsometer (Jobin Yvon) at photon energy from 0.75 to 3.5 eV with an interval of 0.01 eV. The ellipsometric spectra of 0.7PMN–0.3PT thin film are shown in Fig. 5.1.2.1. The spectra exhibit oscillations due to interference. Such oscillations are very useful for determining the thickness and the transparent range of the film.

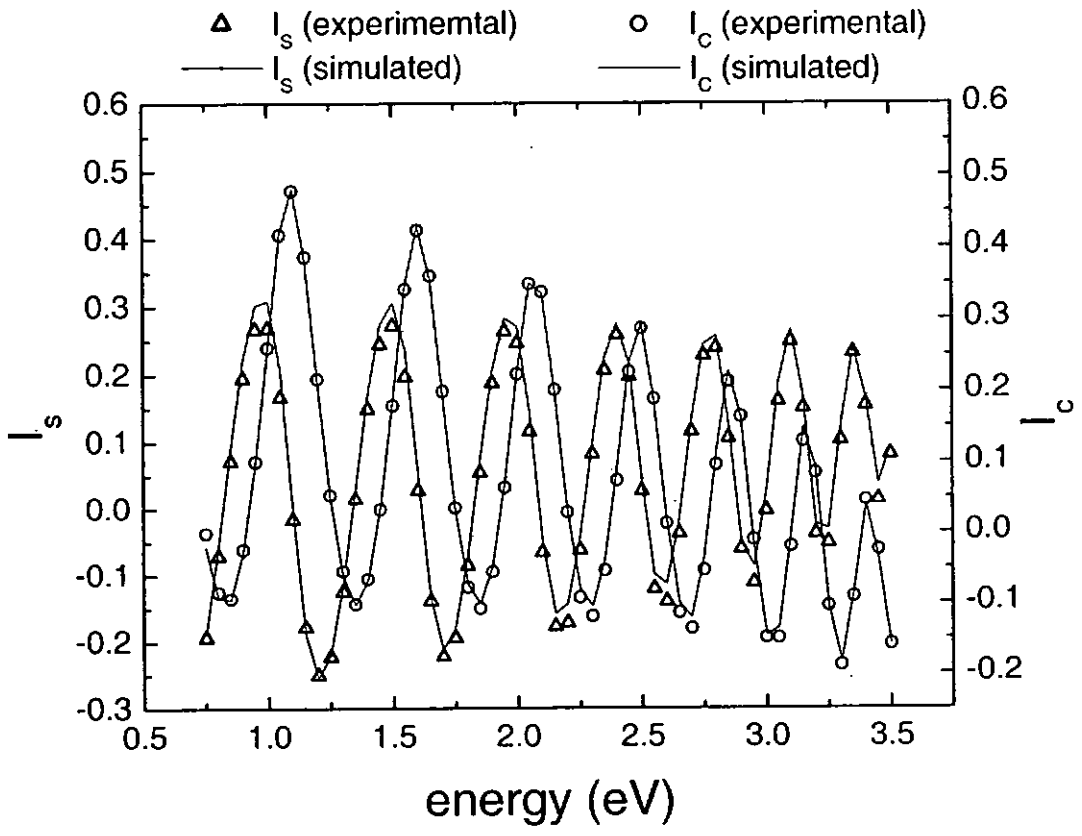

Fig. 5.1.2.1 Spectra of ellipsometric parameters I_S and I_C as functions of energy for a 0.7PMN-0.3PT film.

5.1.3 Modeling and Fitting

The optical properties of oxygen-octahedral ferroelectrics are dominated by their BO_6 octahedra, which governs the low lying conduction bands and the highest valence bands. This lowest energy oscillator is the largest contributor to the dispersion of the refractive index. Other ions in the structure contribute to the higher conduction bands and have a smaller effect on the optical properties of these ferroelectrics. In the fitting, we simulated the experimental data with three different models: Sellmeier, Canchy and Lorentz. For the first two models, acceptable agreements were only obtained in a short dispersion range. Lorentz model, on the other hand, was fitted well for the whole range of 0.75 to 3.5 eV. Therefore, Lorentz oscillator model with four oscillators:

$$\varepsilon(\omega) = \varepsilon_{\infty} + \sum_{j=1}^{4} \frac{f_j \omega_{oj}^2}{\omega_{oj}^2 - \omega^2 + i\gamma_j \omega} \qquad \text{(Eq. 5.1.3.1)}$$

was used in this chapter to describe the dominating interband oscillators of (1-x)PMN–xPT. The model parameters $f_j\omega_{oj}^2$, ω_{oj} and γ_j are the oscillator strengths, resonance energies and damping rate which gives the width of the resonance, respectively. The parameter ε_{∞} represents the contribution at higher frequencies.

Our initial analysis was based on a single-layer Lorentz model with four oscillators. Poor agreement, however, was found with the experimental data. In subsequent

analysis, we modified the single-layer Lorentz model into a double-layer Lorentz model (Fig. 5.1.3.1). In this modified model, we assume that the films are composed of two layers – a bottom bulk (1-x)PMN–xPT layer and a surface layer consisting of bulk (1-x)PMN–xPT and voids. The voids in the surface layer were mainly caused by surface roughness. The net optical constants of the mixed layer ((1-x)PMN–xPT + void) were calculated by the Bruggeman effective medium approximation (BEMA). The reference data of refractive index of single crystal MgO [Nagarajan V. *et al*, 2000] was used as the reference data for the substrate. Using this double-layer Lorentz model to analyze the data over the spectra range 0.75 – 3.5 eV, good fits were obtained between the simulated values of I_S as well as I_C and the experimental data. The solid lines in Fig. 5.1.2.1 denote these fittings. Table 5.1.3.1 shows the values of the fitting parameters for different (1-x)PMN–xPT films.

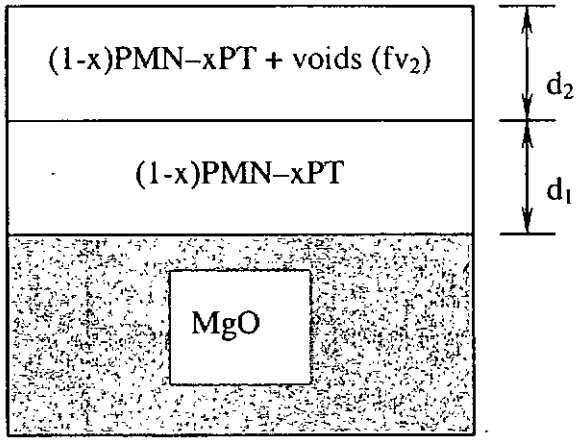

Fig. 5.1.3.1 Double-layer Lorentz model for interpreting (1-x)PMN–xPT||MgO films. f_{v2} is the volume percentage of void (air) in the surface layer. d_1 and d_2 are the layer thicknesses of bottom and top layers respectively.

Table 5.1.3.1 Fitting parameters for (1-x)PMN–xPT films with different composition ratio.

	x = 0	x = 0.1	x = 0.3	x = 0.35	x = 0.4
d_1 (Å)	6215±19.8	5171±19.7	5807±19.1	5382±19.8	9073±15.0
d_2 (Å)	40±1.1	38±1.3	75±2.6	32±2.7	117±1.9
fv_3 (%)	59±5	59±7.9	35±15	50±12	29±11
ε_∞	2.450±0.333	1.375±0.252	2.699±0.257	1.900±0.083	1.714±0.525
f_1	0.760±0.304	1.008±0.157	1.368±0.014	0.854±0.077	0.605±0.085
ω_{o1}	4.051±0.145	4.453±0.063	5.644±0.060	4.468±0.032	3.800±0.035
γ_1	0.250±0.015	-1.075±0.032	1.257±0.093	-0.628±0.006	0.306±0.013
f_2	0.265±0.011	2.798±0.214	-0.516±0.247	2.753±0.002	0.631±0.051
ω_{o2}	5.000±0.039	5.987±1.917	3.968±0.024	6.327±0.005	4.283±0.258
γ_2	-2.830±0.047	1.692±0.807	0.874±0.162	0.730±0.019	-0.924±0.975
f_3	-0.120±0.902	0.302±0.173	1.237±0.033	0.447±2.736	-1.085±0.540
ω_{o3}	1.950±0.044	3.809±0.081	4.907±0.704	3.848±0.005	1.925±0.689
γ_3	-3.389±0.381	0.263±0.013	-0.759±0.521	0.292±0.093	0.626±0.149
f_4	1.950±0.403	-	1.070±0.211	-	3.146±0.496
ω_{o4}	5.454±0.415	-	3.985±0.270	-	6.910±0.015
γ_4	0.289±0.051	-	0.478±0.019	-	0.908±0.032

Figures 5.1.3.2 (a) and (b) show the refractive index n and extinction coefficient k of (1-x)PMN–xPT films with different PT compositions as a function of energy obtained based on Eq. 5.1.3.1. In general, the extinction coefficients are fairly flat below 2.5 eV and increase more sensitively at higher energies. However, the refractive indices appear to be continuously increased non-linearly over the entire range of energies with a more receptive increase at energies above 2.5 eV. This behavior is typical of an insulator or semiconductor in the range of energy near the band gap. Below the band gap, transmission dominates with a tiny extinction coefficient. As the band gap energy is approached from below, both n and k increase with k approaches a resonance characterized by one of the oscillators in the Lorentz model. As the PT content increases, the refractive index of (1-x)PMN–xPT film increases. This is due to the smaller band gap and hence higher refractive index of PT as compared to that of PMN (shown in Fig. 5.1.3.2 (a)). The refractive index of PT ceramics [Landolt-Börnstein, 1981] is also plotted in Fig. 5.1.3.2 (a) for comparison. The dispersion profile of PT ceramics (only of a limited region) is very similar to those of our (1-x)PMN–xPT films of different PT contents. We also notice that the refractive index of PMN single crystal is larger than that of our PMN film. For example, the refractive indices of PMN single crystal [McHenry D. A., 1992] and PMN film are 2.522 and 2.469 at 633 nm respectively. The slightly larger lattice constant of MgO implies that the epitaxial films take on a lower density than in the bulk. The presence of grain boundary, lower film density and poor crystallinity in the films also contribute to a reduced refractive index. Furthermore, grain size may also affect the refractive index. Further investigation is

needed to unravel the dependence of the refractive index on grain size. Figure 5.1.3.2 (b) shows that the extinction coefficient k of (1-x)PMN–xPT films increases sharply with energy for energies higher than 3.2 eV. The sharp increase in k signifies a change in the optical properties from dominantly transmission to absorption as the band gap energy is approached. For (1-x)PMN–xPT films, the main contribution of optical loss comes from the band gap as well as grain boundary scattering. These mechanisms become increasingly important for photon energies near the band gap and for photon wavelengths comparable to the grain size of the films [DiDomenico M. J. *et al*, 1969; Tian H. Y. *et al*, 2001].

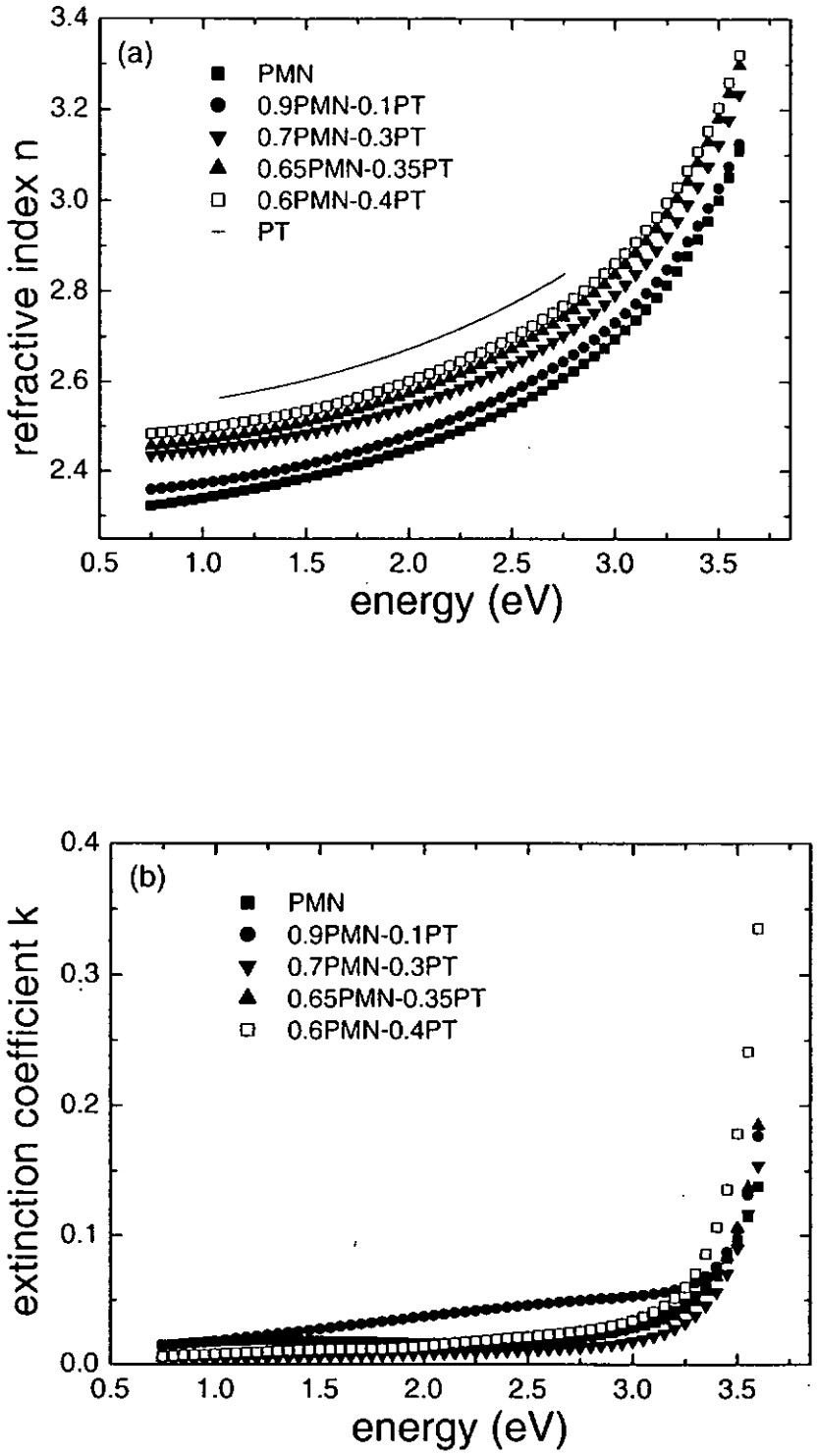

Fig. 5.1.3.2 Dispersion spectra of (a) the refractive indices and (b) the extinction coefficients of (1-x)PMN–xPT films with different $PbTiO_3$ content.

The dominating features in the optical properties of (1-x)PMN–xPT for energies below 3.5 eV come from the inter-band electronic transitions between the low lying conduction bands and the upper valence bands. It is, therefore, useful to investigate the change in the band gap as the PT content changes. In order to determine the band gap energy, the absorption coefficients α of the films were derived from the extinction coefficients k using:

$$\alpha = \frac{4\pi k}{\lambda} \qquad \text{(Eq. 5.1.3.2)}$$

where λ is the wavelength. The band gaps of (1-x)PMN–xPT films were then deduced from α and the energy of the incident light $h\nu$ using the Tauc equation [Tauc J. C., 1972]:

$$(\alpha h\nu)^2 = B(h\nu - E_g) \qquad \text{(Eq. 5.1.3.3)}$$

where B is a constant and E_g is the band gap energy. In this equation, the relation $\alpha \propto \sqrt{h\nu - E_g}$ results from the joint density of states. By extrapolating the linear portion of the Tauc curve to zero, as shown in Fig. 5.1.3.3, band gap energies were obtained for our (1-x)PMN–xPT films. The values are shown in Table 5.1.4.1.

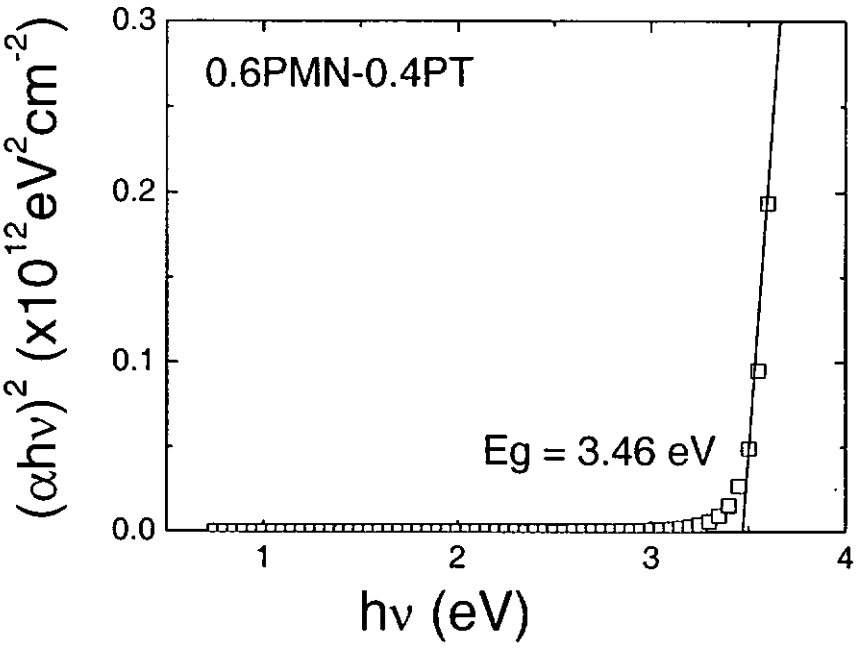

Fig. 5.1.3.3 The Tauc plot $(\alpha h\nu)^2$ obtained from the fitted extinction coefficient against energy for 0.6PMN-0.4PT. The straight line is the extrapolation of the linear portion of the Tauc plot.

5.1.4 Transmittance Measurement

In order to confirm the values of the band gap of (1-x)PMN–xPT films, optical transmittance measurements (Shimadzu UV – 2101 PC) were also performed. Figure 5.1.4.1 shows the transmittance spectra of (1-x)PMN–xPT films grown on single crystal MgO. As the surface roughness is much smaller than visible wavelengths, the oscillations in the optical transmittance spectra were resulted from multiple reflections. All the films, in general, showed a good optical transmittance of about 80 % in the visible region. The percentage of transmittance of the films decreases to zero near 350 nm due to the interband transitions. Figure 5.1.4.2 shows the Tauc plot of $(\alpha h\nu)^2$ vs $h\nu$. By extrapolating the linear portion of the curve to zero, the band gap energies were identified. Results are also listed in Table 5.1.4.1. We notice that the two sets of values of the band gap obtained by two different techniques are very similar values. They both indicate that optical band gap energy of (1-x)PMN–xPT is a composition-dependent parameter and decreases with PT content.

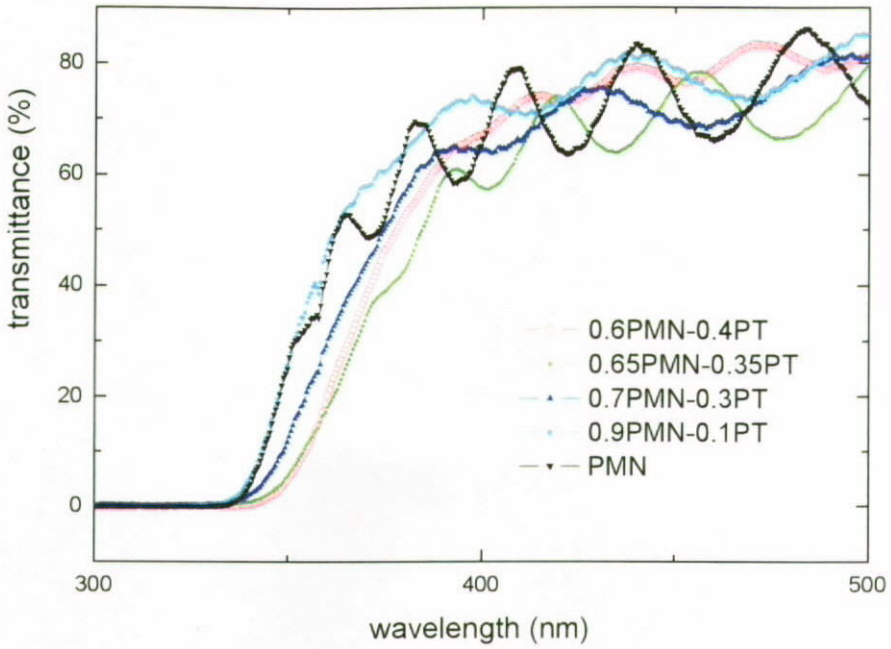

Fig. 5.1.4.1 Transmittance spectra of (1-x)PMN–xPT films with different PT compositions.

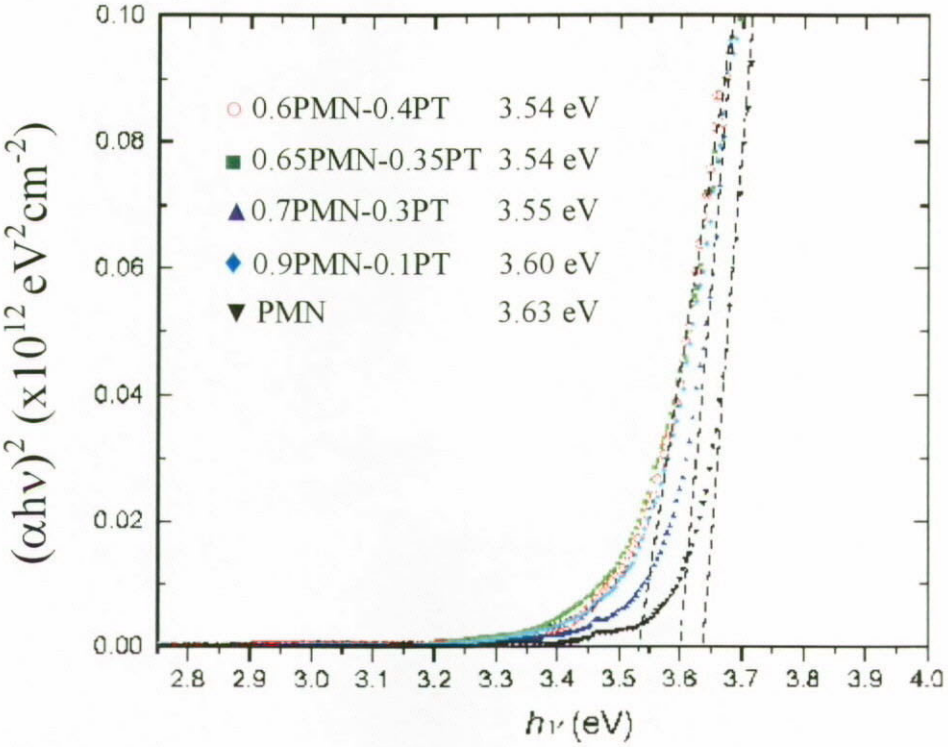

Fig. 5.1.4.2 Dependencies of the absorption coefficients $(\alpha h\nu)^2$ on the photon energy obtained from the transmittance spectra for (1-x)PMN–xPT films with different PT compositions.

Table 5.1.4.1 Energy band gaps (E_g) of different (1-x)PMN–xPT films obtained by transmittance measurement and SE.

(1-x)PMN-xPT	E_g (Trans) (eV)	E_g (SE) (eV)	% Error $\left(1-\frac{E_g(SE)}{E_g(Trans)}\right)\times 100\%$
x = 0	3.63	3.54	4.8
0.1	3.60	3.52	8.5
0.3	3.55	3.51	9.9
0.35	3.54	3.51	3.5
0.4	3.54	3.45	8.1

5.1.5 Surface Morphology

In order to verify the thickness profile obtained by SE, the surface morphology and thickness of films were examined by top view image and side view image of scanning electron microscopy (SEM). The surface roughness, on the other hand, was characterized by atomic force microscopy (AFM). Surface roughness of all the samples was obtained by scanning an area of 0.5x0.5 μm^2 in contact mode. This measured surface roughnesses obtained by AFM were compared with the d_2 values obtained from ellipsometer. Studies showed that these two sets of values are linearly proportional to each other. [Koh J., *et al*, 1996]

Figures 5.1.5.1 (a) and (b) show the surface and cross-section SEM images of a 0.65PMN–0.35PT film. The surface, in general, is smooth and crack-free as observed in SEM micrographs, while the film and the substrate are easily distinguished in the cross-section SEM image. All the films show similar features. The thickness of this 0.65PMN-0.35PT film is about 561 nm and is close to the value obtained by SE. The root mean square (rms) roughness of the film obtained by AFM is about 3.9 nm. This value is similar to that obtained by SE (d_2 = 3.2 nm). Figure 5.1.5.2 shows a typical AFM image of our 0.65PMN-0.35PT films. Tables 5.1.5.1 and 5.1.5.2 show the values obtained by SEM and AFM respectively of all the samples compared to those obtained by SE.

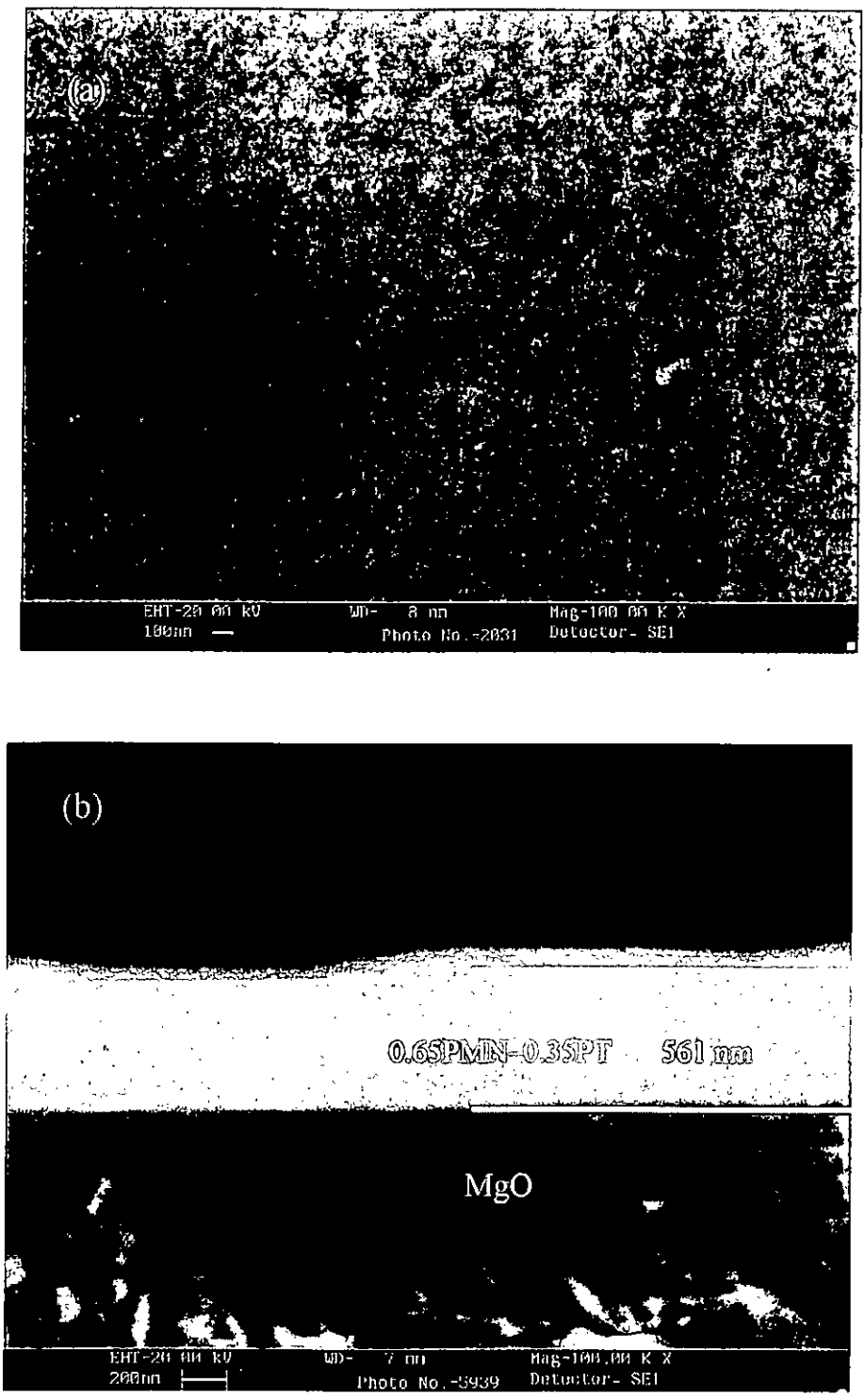

Fig. 5.1.5.1 SEM micrographs showing the (a) surface morphology and (b) cross-section of 0.65PMN-0.35PT film grown on MgO substrate.

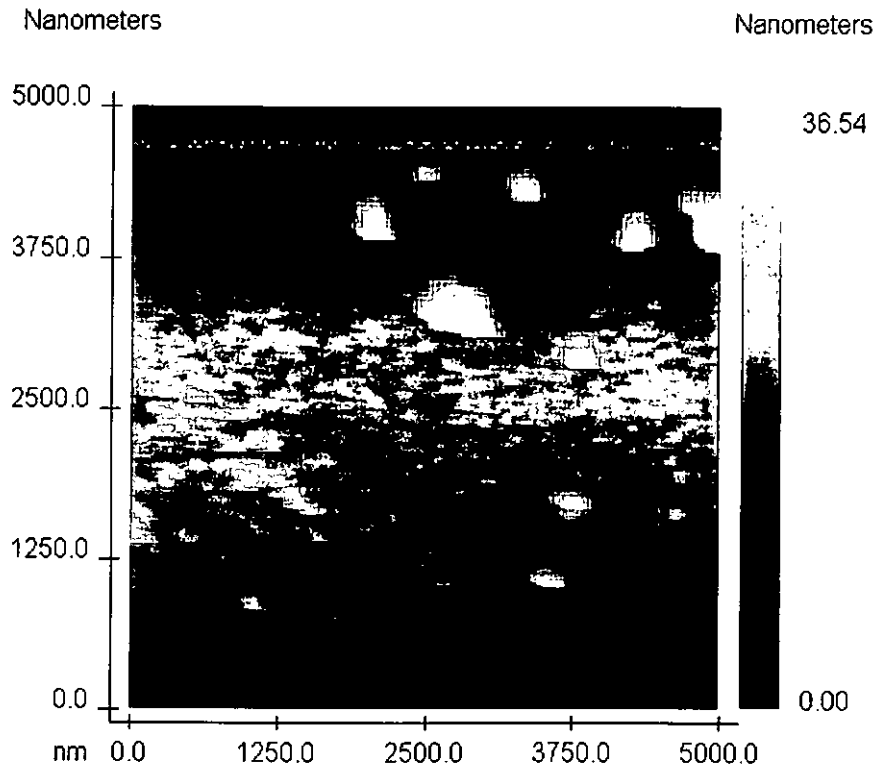

Fig. 5.1.5.2 AFM image of 0.65PMN-0.35PT||MgO film.

Table 5.1.5.1 Film thicknesses of different (1-x)PMN–xPT films obtained by SE and SEM.

(1-x)PMN-xPT	SE $d_1 + d_2$ (nm)	SEM d (nm)	% Error $\left(1-\frac{SE\ \ d_1+d_2}{SEM\ \ d}\right)\times 100\%$
x = 0	626	657	4.7
0.1	521	480	8.5
0.3	589	535	10
0.35	541	561	3.6
0.4	919	850	8.1

Table 5.1.5.2 Surface roughness of different (1-x)PMN-xPT films obtained by SE and SEM.

(1-x)PMN-xPT	SE d_2 (nm)	AFM d (nm)	% Error $\left(1-\frac{SE\ \ d_2}{AFM\ \ d}\right)\times 100\%$
x = 0	4.0	4.3	7.0
0.1	3.8	3.8	0.0
0.3	7.5	7.6	1.3
0.35	3.2	3.9	17.9
0.4	11.7	9.8	19.4

5.2 DEPOSITION TEMPERATURE DEPENDENCE

It is well known that deposition temperature has a prominent effect on crystal structure as well as crystallinity and thus the refractive indices of the films. In this section, 0.65PMN-0.35PT films were grown on single crystal MgO substrate with different deposition temperatures ranging from 630°C to 710°C by PLD method. The deposition conditions were similar to those reported in section 5.1. The refractive indices of the films were again measured by ellipsometer.

5.2.1 Structural Characterization

Figure 5.2.1.1 shows the XRD θ–2θ scans of 0.65PMN-0.35PT films deposited at different temperatures. Highly oriented 0.65PMN–0.35PT films of perovskite phase are observed. The out-of-plane lattice constants calculated from the diffraction angles of (002) peak of 0.65PMN–0.35PT films with deposition temperatures at 630°C, 670°C and 710°C are 3.99 Å, 4.01 Å and 4.03 Å respectively. The FWHM of the rocking curves are 1.65°, 0.79° and 2.3° respectively (Fig. 5.2.1.2). XRD ϕ-scans of the (202)0.65PMN–0.35PT and (202)MgO were performed to confirm the epitaxy of our films. Figure 5.2.1.3 shows a typical ϕ-scan for 0.65PMN–0.35PT film with deposition temperature of 670°C. The peaks of 0.65PMN–0.35PT and MgO are at the same position and separated by 90°. This clearly shows the four-fold symmetry of both the film and the substrate. Our XRD results indicate that all 0.65PMN–0.35PT films are

cube-on-cube grown on (001)MgO substrates with an in-plane epitaxial relationship of (001)0.65PMN–0.35PT||(001)MgO.

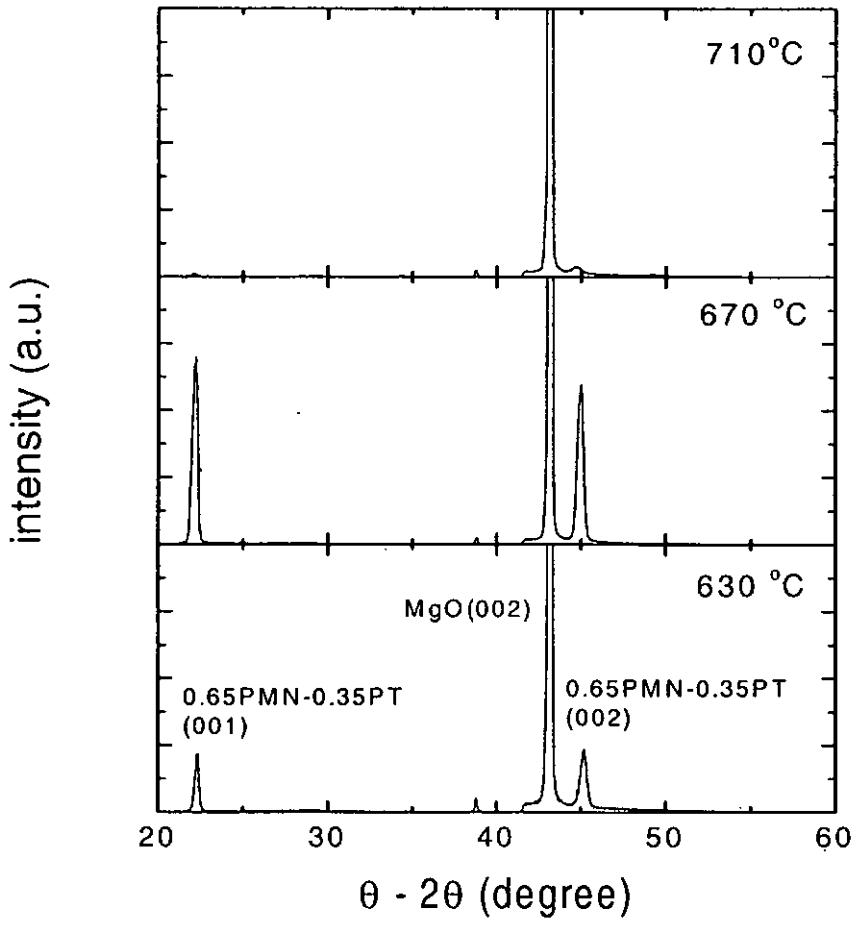

Fig.5.2.1.1 XRD θ–2θ scans of 0.65PMN-0.35PT films with different deposition temperatures.

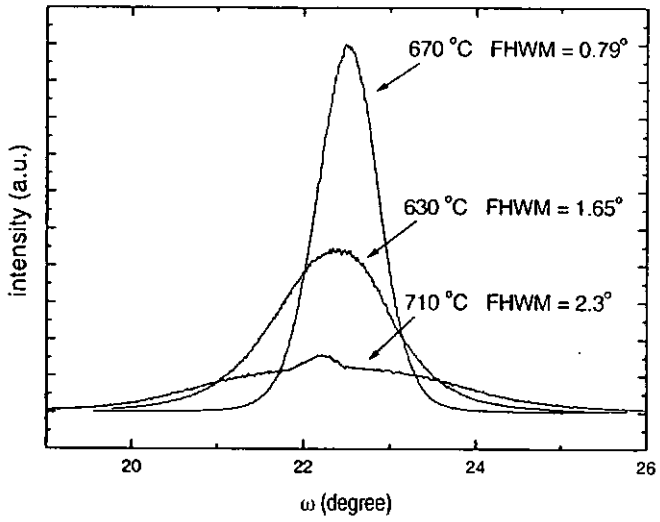

Fig. 5.2.1.2 XRD ω-scans of 0.65PMN-0.35PT films grown on single crystal MgO substrate with different deposition temperatures.

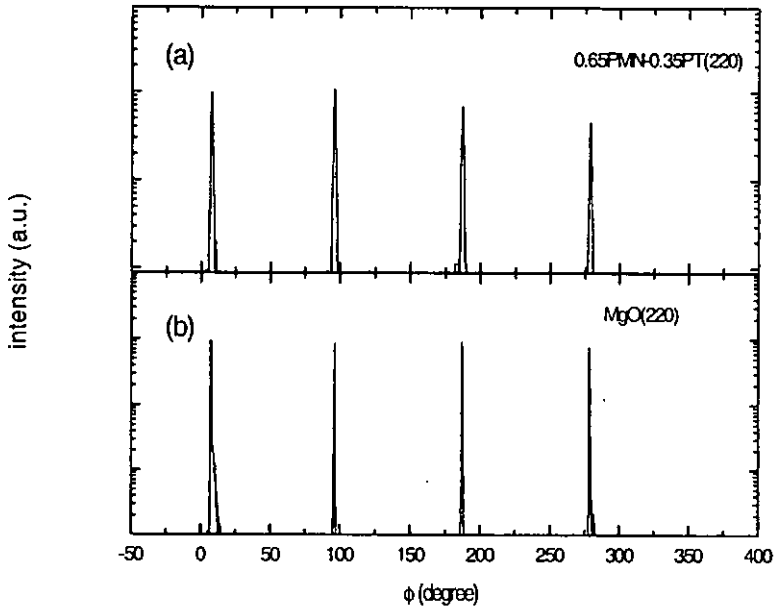

Fig. 5.2.1.3 XRD ϕ–scan of the (a) 0.65PMN-0.35PT(202) and (b) MgO(202) deposited at 670°C.

5.2.2 Modeling and Fitting

In this section, similar fitting steps of previous section were employed. Here, the double-layer Lorentz oscillator model with three oscillators was used. Figure 5.2.2.1 shows the ellipsometric spectra of experimental and simulated ellipsometric angles, I_S and I_C, for 0.65PMN–0.35PT film deposited at 710°C. Good fits between the simulated values of I_S as well as I_C and the experimental data were obtained. The solid lines in Fig. 5.2.2.1 denote these fittings. Table 5.2.2.1 shows the values of the fitting parameters for the films with different deposition temperatures.

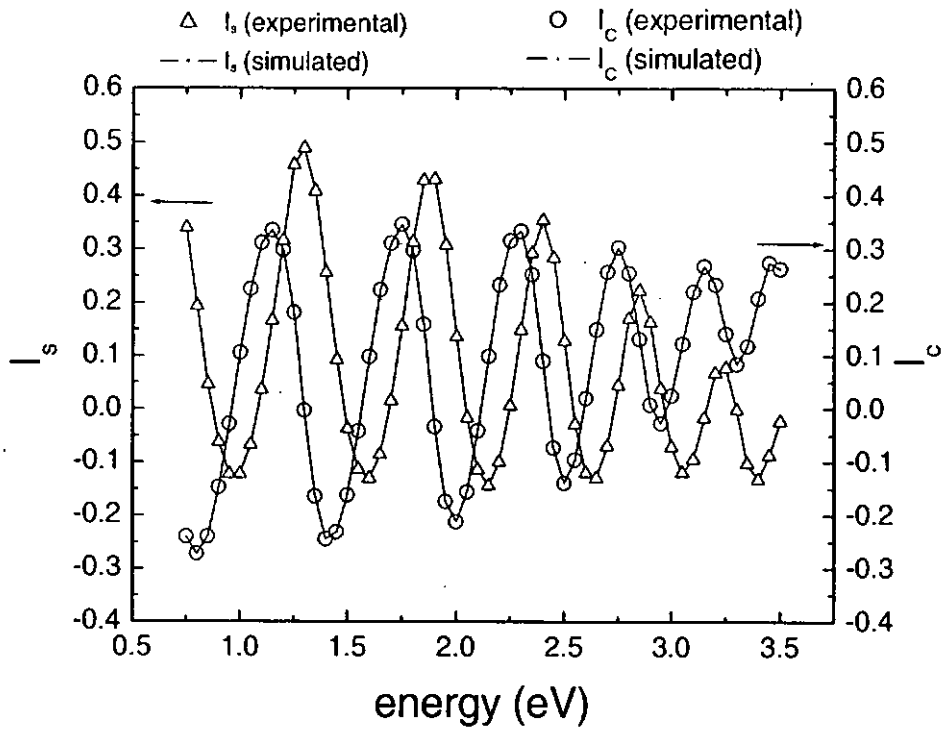

Fig. 5.2.2.1 Spectra of ellipsometric parameters I_S and I_C as functions of energy for 0.65PMN–0.35PT film deposited at 670°C.

Table 5.2.2.1 Fitting parameters for 0.65PMN–0.35PT films with different deposition temperatures.

Temp/ °C	630	670	710
d_1 (Å)	5385±18.0	5382±19.8	4436±4.6
d_2 (Å)	25±2.4	32±2.7	66±0.7
fv_3 (%)	65±5.9	50±12	57±5.4
ε_∞	1.889±0.349	1.900±0.083	2.678±0.355
f_1	3.126±0.322	0.854±0.077	3.345±0.234
ω_{o1}	5.762±0.229	4.468±0.032	4.981±0.198
γ_1	0.127±0.295	-0.628±0.006	0.520±0.056
f_2	0.518±0.381	2.753±0.002	-0.443±0.330
ω_{o2}	3.927±0.860	6.327±0.005	-8.361±0.028
γ_2	0.172±0.664	0.730±0.019	5.447±0.065
f_3	9.200±0.200	0.447±2.736	-0.347±0.237
ω_{o3}	0.388±0.061	3.848±0.005	-1.945±0.312
γ_3	18.078±0.042	0.292±0.093	-11.022±0.216

Figures 5.2.2.2 (a) and (b) shows the refractive index and extinction coefficient dispersion curves of 0.65PMN–0.35PT films deposited at different temperatures based on Eq. 5.1.3.1. In general, the refractive index n appears to be continuously increased nonlinearly over the whole energy range from 0.75 to 3.5 eV. Indeed, it increases more rapidly at higher energies. However, the extinction coefficient k is fairly flat below 2.5 eV. Below the band gap, transmission dominates with a small extinction coefficient. As the band gap energy is approached from below, both n and k increase with k approaches a resonance characterized by one of the oscillators in the Lorentz model. Meanwhile, as observed in Fig. 5.2.2.2 (a), the refractive indices of 0.65PMN–0.35PT films increase from deposition temperature of 630°C to 670°C, but decrease at 710°C. This lowering of refractive index at higher temperature might be caused by the loss of PbO. It is well known that PbO evaporated and escaped from film surface at an elevated post-deposition annealing temperature [B. Jaffe, 1971]. In this circumstance, PbO evaporation and grain densification increase the film's porosity and hence locally reduce the density of film. This phenomenon was reported in lead-based ferroelectric films [Fox G. R., 1992]. We believe that films' reduction of film's density decreases the refractive index of the film. Hence, the refractive index of film decreases with a larger deposition temperature. According to Fig. 5.2.2.2 (b), the extinction coefficient of 0.65PMN–0.35PT film deposited at 710°C, particularly at higher energy region, is larger than those of other two films. This larger extinction coefficient is due to a larger grain size as well as higher porosity, resulting in a stronger scattering of light.

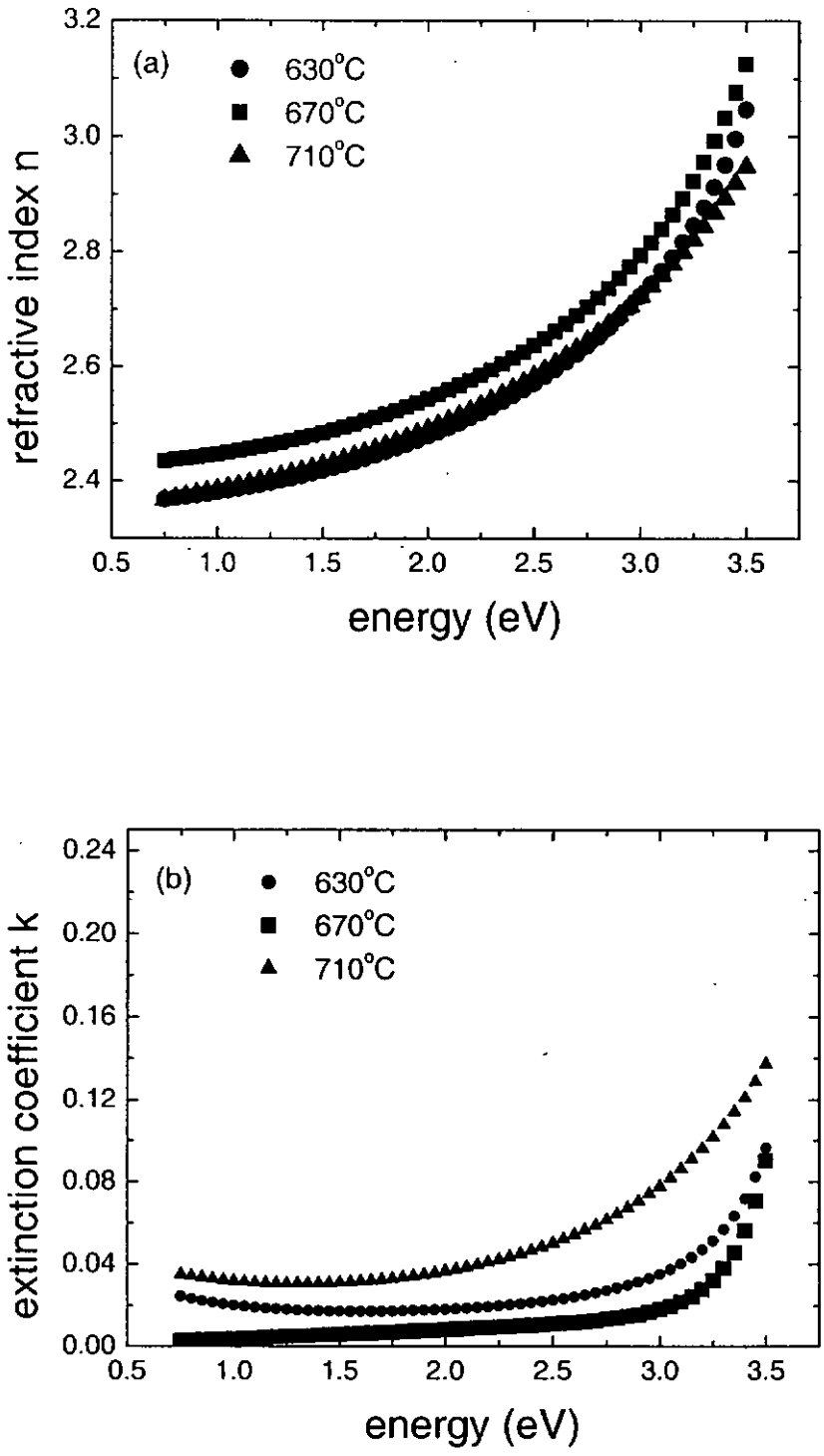

Fig. 5.2.2.2 Dispersion spectra of (a) the refractive indices and (b) the extinction coefficients of 0.65PMN–0.35PT films deposited at different temperatures.

Since the optical properties of (1-x)PMN–xPT are dominated by inter-band electronic transitions between the lower lying conduction bands and the upper valence bands of BO_6 octahedra, it is of great interest to investigate the change of the optical band gap of (1-x)PMN–xPT films deposited at different temperatures. The absorption coefficients of the films were obtained from extinction coefficients using Eq. 5.1.3.2. The optical band gap energies were derived from Eq. 5.1.3.3. Figure 5.2.2.3 shows the dependence of the absorption coefficients $(\alpha h\nu)^2$ on the photon energy for 0.65PMN–0.35PT films deposited at 710°C. By extrapolating the linear portion of the curve to zero, the band gap energy was close to 3.30 eV. Indeed, all the band gap energies obtained for films deposited at different temperatures were close to 3.30 eV. Therefore, we believe that the band gap energy is independent of the deposition temperature within our experimental range.

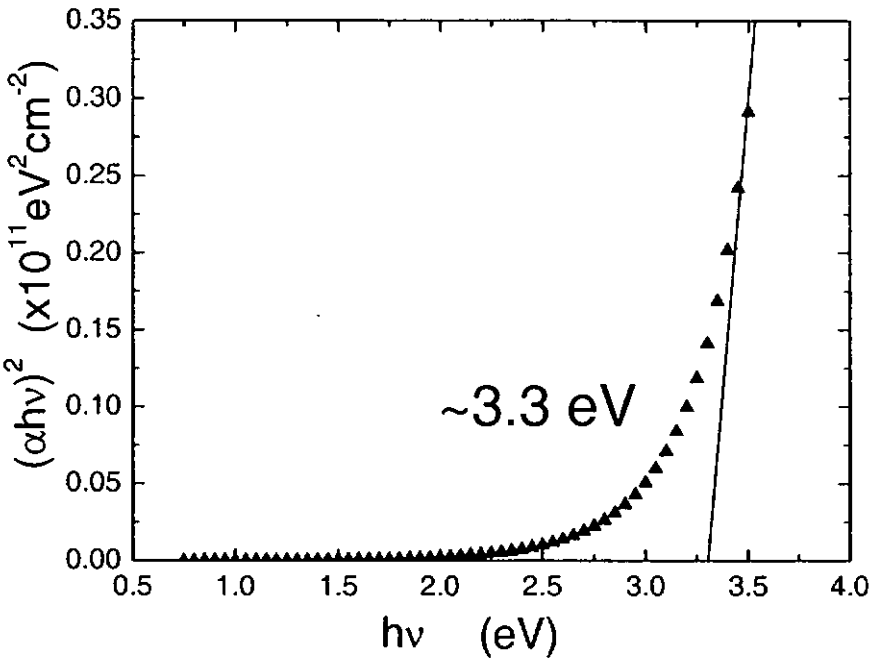

Fig. 5.2.2.3 The Tauc plot $(\alpha h\nu)^2$ obtained from the fitted extinction coefficient against energy for 0.65PMN–0.35PT film deposited at 710°C. The straight line is the extrapolation of the linear portion of the Tauc plot.

5.2.3 Transmittance Measurement

In order to verify the values of the band gap energies of 0.65PMN–0.35PT films obtained by SE, optical transmittance measurements were carried out. Figure 5.2.3.1 shows the transmittance spectra of 0.65PMN–0.35PT films. The transmittance curve of the 0.65PMN–0.35PT film deposited at 710°C shows a larger absorption at wavelengths below band gap, which is agreed with the extinction coefficient profile obtained by SE measurements.

Figure 5.2.3.2 shows the dependence of the absorption coefficients $(\alpha h\nu)^2$ on the photon energy obtained from the transmittance spectra. The extrapolations of the linear portion of the Tauc curves are about 3.5 eV and there is no observable change in the band gap energies as we changed the deposition temperature from 630°C to 710°C. We notice that the two sets of values of the band gaps obtained by two different techniques take on similar trend and values. They both indicate that band gap energy of 0.65PMN–0.35PT film is independent of deposition temperature. Compared to the dependency in composition of (1-x)PMN–xPT where the band gap energy changes by about 3 % as we change x from 0 to 0.4, the band gap energy seems to be not sensitive to deposition temperature.

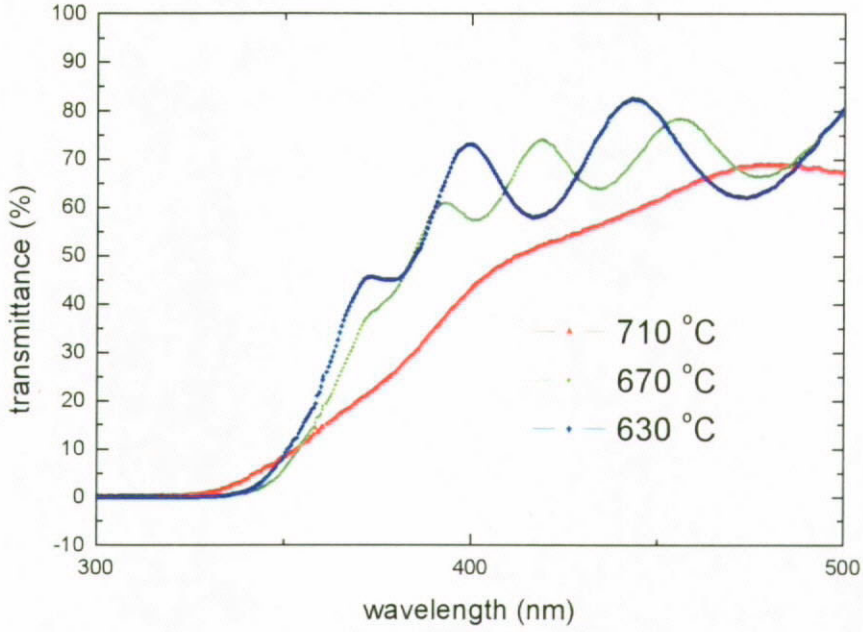

Fig. 5.2.3.1 Transmittance spectra of 0.65PMN–0.35PT films with different deposition temperatures.

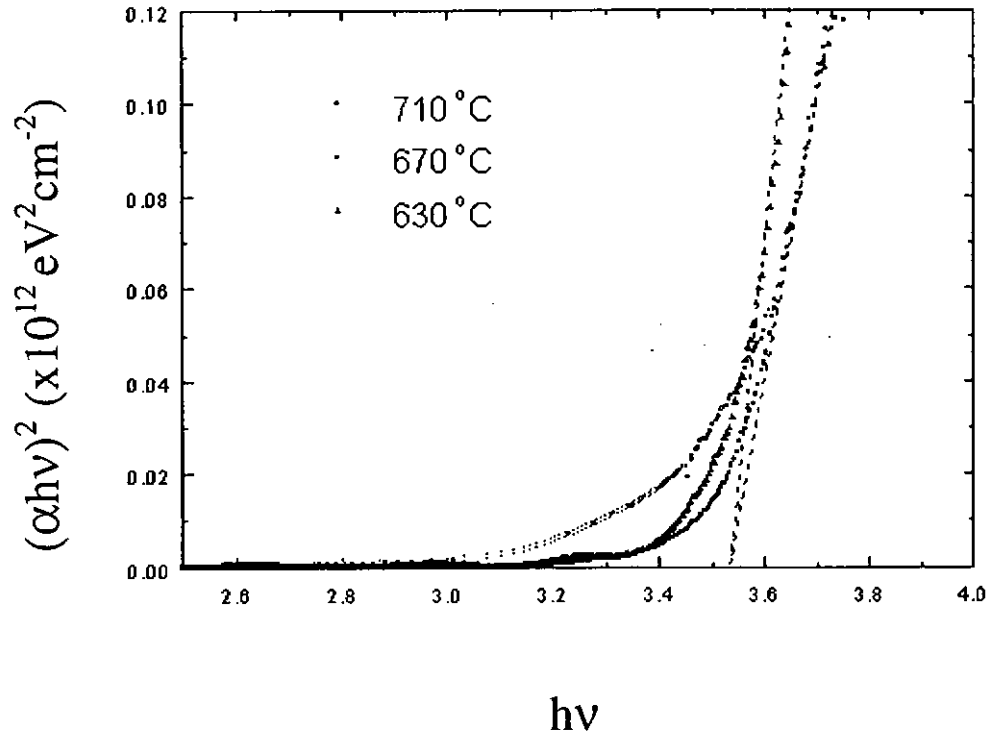

Fig. 5.2.3.2 Dependencies of the absorption coefficients $(\alpha h\nu)^2$ on photon energy obtained from the transmittance spectra for 0.65PMN–0.35PT films with different deposition temperatures.

5.2.4 Surface Morphology

Surface morphology and cross section of 0.65PMN-0.35PT films deposited at different temperatures were examined by SEM. These SEM micrographs are shown in Figs. 5.2.4.1 and 5.2.4.2 respectively. The film roughness was measured by AFM. These AFM images are shown in Fig. 5.2.4.3. Our SEM images reveal that all (1-x)PMN–xPT film surface are, in general, dense, smooth and crack-free. The films grown at 630°C and 670°C exhibit no observable feature indicating that the films are densely packed with very fine grains (< 10 nm). As the substrate temperature increases to 710°C, the film surface is covered with irregular-shape grains with a fairly uniform size distribution of approximately 300 nm. As observed by AFM, these grains result in a rougher surface (5.5 nm) as compared to other two films (about 4 nm). Furthermore, grain enlargement and pores at grain boundaries are also observed at film annealed at 710°C. This means that the porosity of the film is increased resulting in a larger grain scattering. Thus, a larger extinction coefficient of the film at short wavelength was obtained.

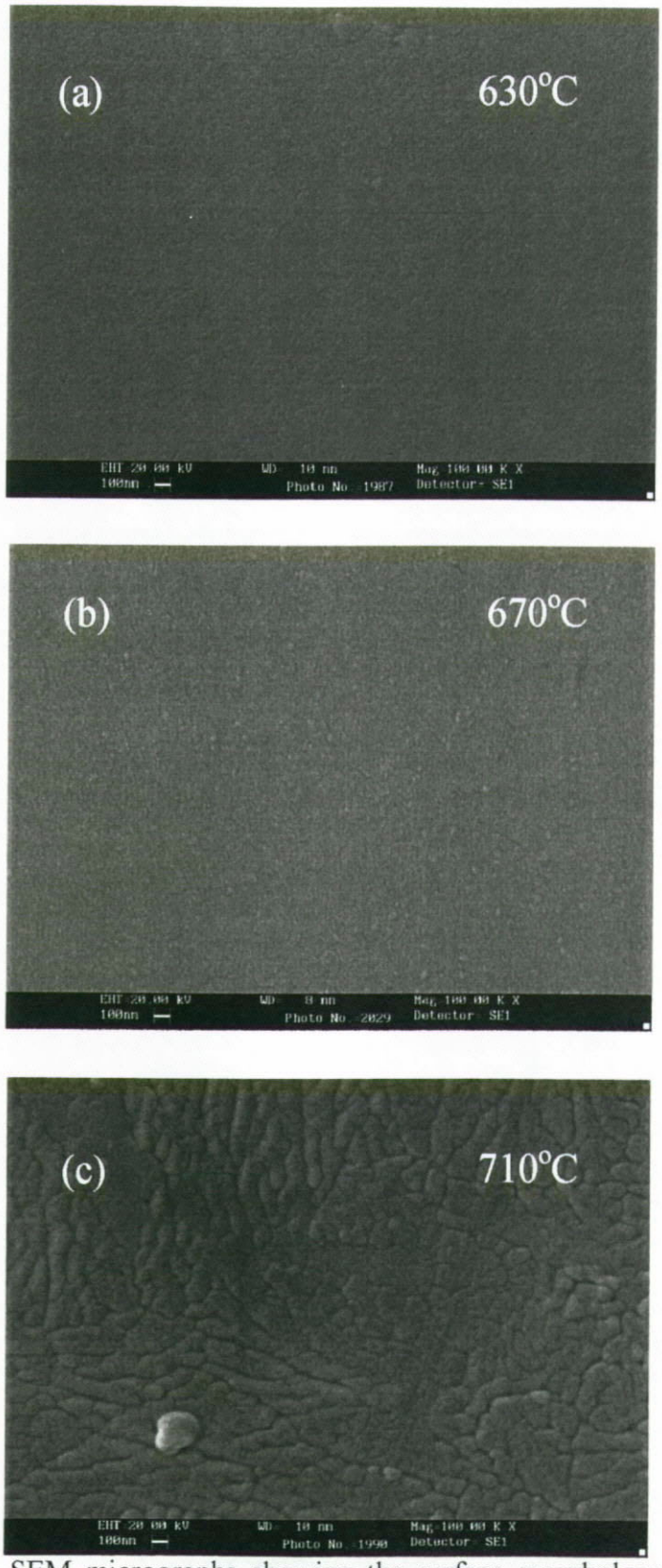

Fig. 5.2.4.1 SEM micrographs showing the surface morphology of 0.65PMN–0.35PT films grown on MgO substrate deposited at (a) 630°C, (b) 670°C and (c) 710°C.

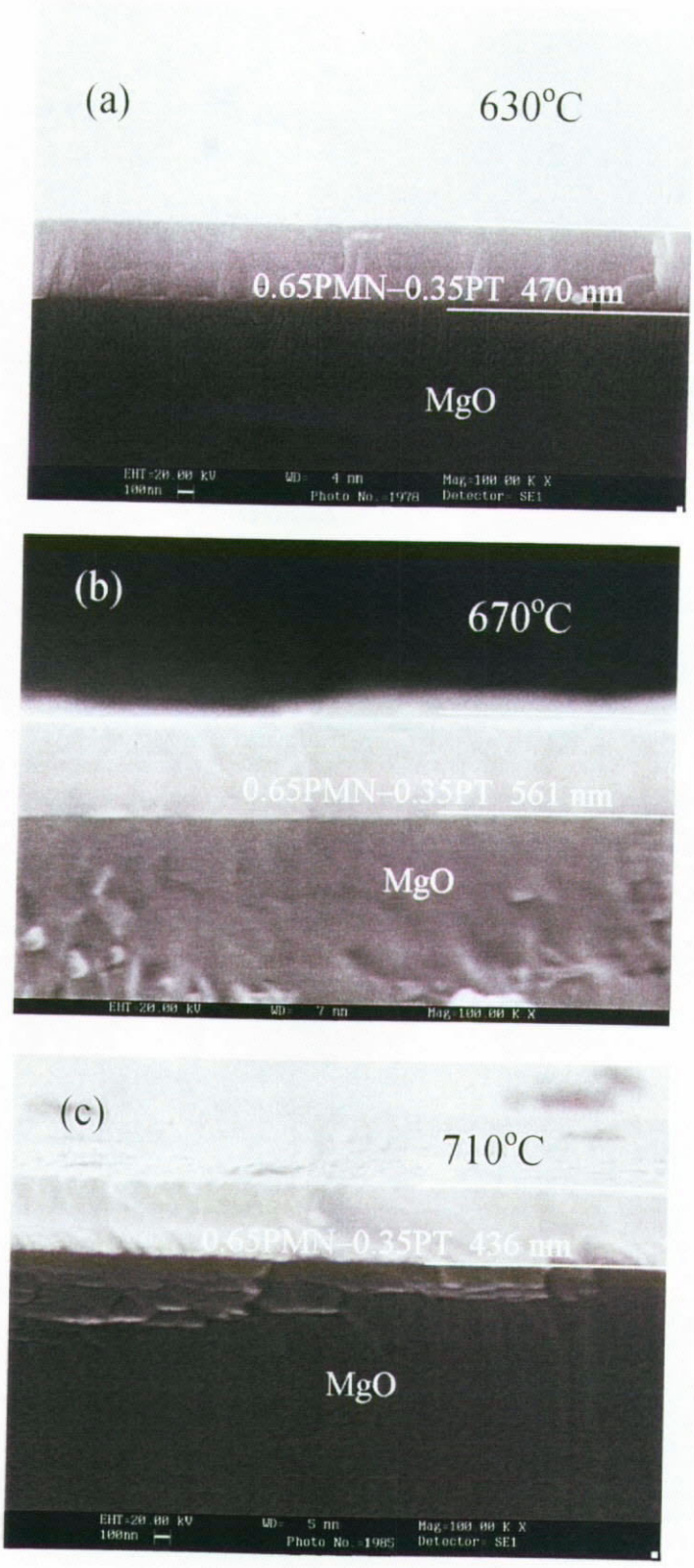

Fig. 5.2.4.2 SEM micrographs showing the cross section of 0.65PMN–0.35PT films grown on MgO substrate deposited at (a) 630°C, (b) 670°C and (c) 710°C.

(a) 630°C

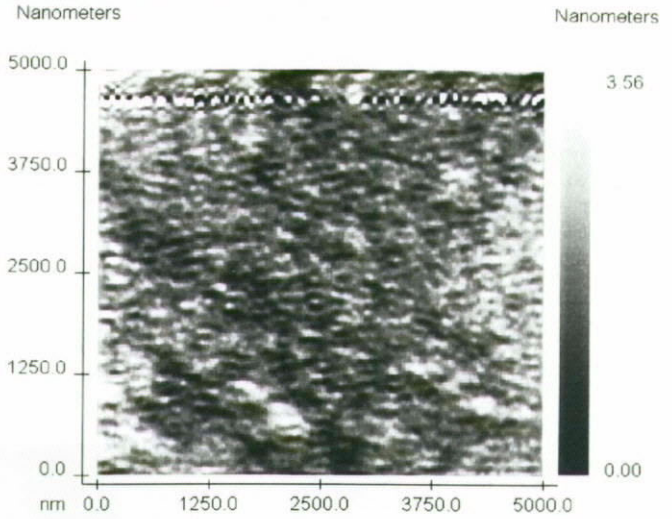

(b) 670°C

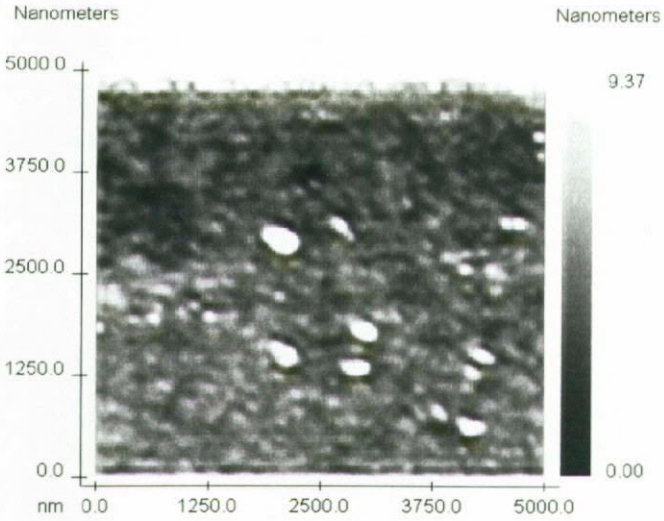

(c) 710°C

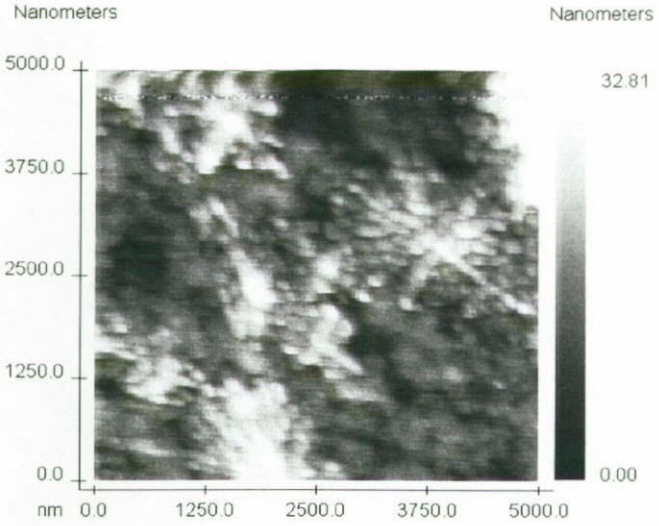

Fig. 5.2.4.3 AFM images of 0.65PMN–0.35PT||MgO films deposited at different temperatures.

Table 5.2.4.1 Film thicknesses of different 0.65PMN–0.35PT films obtained by SE and SEM.

Temperature /°C	SE d_1+d_2 (nm)	SEM d (nm)	% Error $\left(1-\frac{SE\ \ d_1+d_2}{SEM\ \ d}\right)\times 100\%$
630	539	470	14
670	541	561	4.1
710	444	436	0.23

Table 5.2.4.2 Surface roughness of different 0.65PMN-0.35PT films obtained by SE and SEM.

Temperature /°C	SE d_2 (nm)	AFM d (nm)	% Error $\left(1-\frac{SE\ \ d_2}{AFM\ \ d}\right)\times 100\%$
630	2.5	4.3	42
670	3.2	3.9	18
710	6.6	5.5	17

CHAPTER 6 OPTICAL PROPERTIES OF STRONTIUM BARIUM NIOBATE THIN FILMS

In this chapter, similar to previous investigation on the effects of processing parameters on the optical properties of (1-x)PMN–xPT films, the effects of annealing temperature and duration on the refractive indices of sol-gel derived SBN60 ($Sr_{0.6}Ba_{0.4}Nb_2O_6$) films were studied.

6.1 ANNEALING TEMPERATURE DEPENDENCE

6.1.1 Fabrication and Structural Characterization

Spin-coating technique was used to fabricate SBN60 films on 1×1 cm^2 (001)Si substrates. Unless stated otherwise, the following conditions for producing SBN60 films were employed in all cases. The sol solution had a concentration of 0.16 M and was spin-coated on silicon substrates using a spin coater operated at 3000 rpm for 30 s. After drying for several seconds on a hot plate at a temperature of 150°C, the films were then annealed at a temperature range between 200°C and 700°C for 2 hours with an interval of 100°C.

XRD θ-2θ profiles of the SBN60 films annealed at different temperatures are shown in Fig. 6.1.1.1. Due to the small thickness of the films (≤ 100 nm), XRD signals are generally very weak. From the figure, peaks corresponding to the tetragonal tungsten bronze (TTB) phase SBN60 are identified only in films with annealing temperatures above 600°C. As expected, the crystalline films are polycrystalline due to the large lattice mismatch between SBN60 film and Si substrate. Hence, our XRD results indicate that crystallization process is occurred at an annealing temperature between 500°C and 600°C.

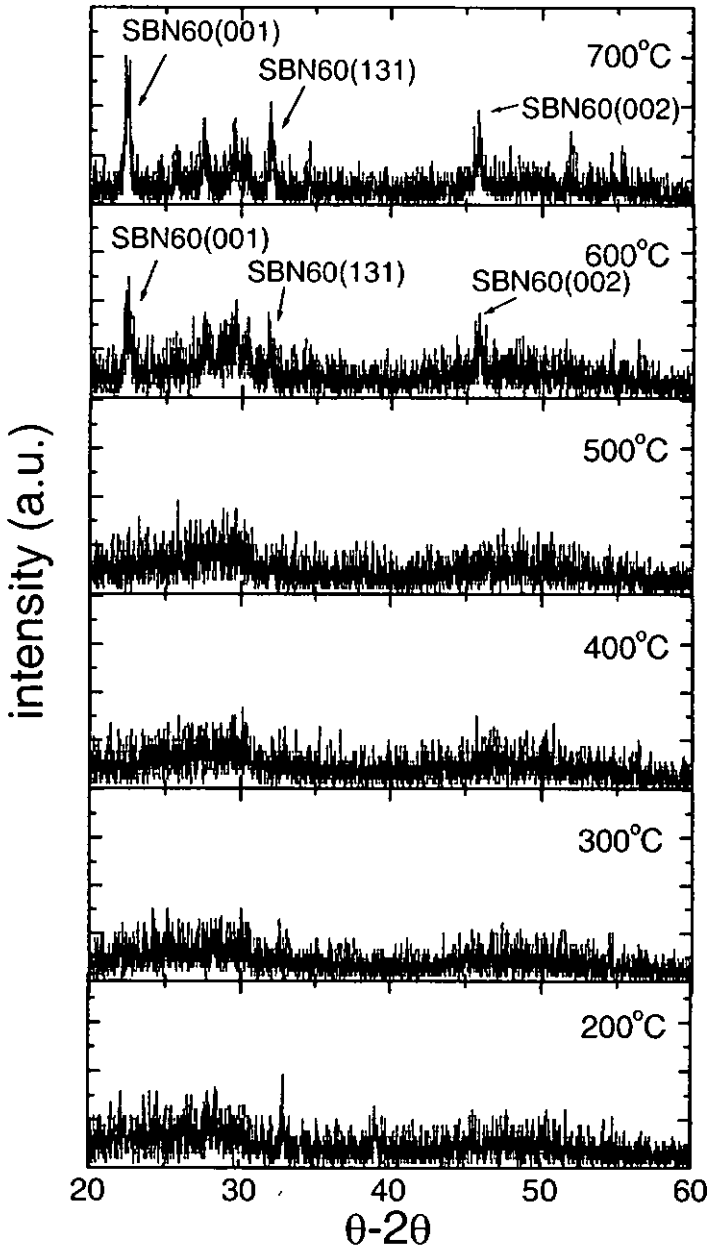

Fig.6.1.1.1 XRD θ-2θ scans of the SBN60 films with different annealing temperatures.

Figure 6.1.1.2 shows the SEM surface micrograph of the SBN60 film annealed at 600°C. Indeed, for films annealed at or below 500°C (figure not shown), no observable features are detected in SEM micrographs. In the figure, grains with a grain size of about 100 nm are observed. These grains are elongated, cylindrical in shape and evenly distributed over the substrate. Thus, the micrograph shows that the sol-gel SBN60 film was well crystallized at 600°C.

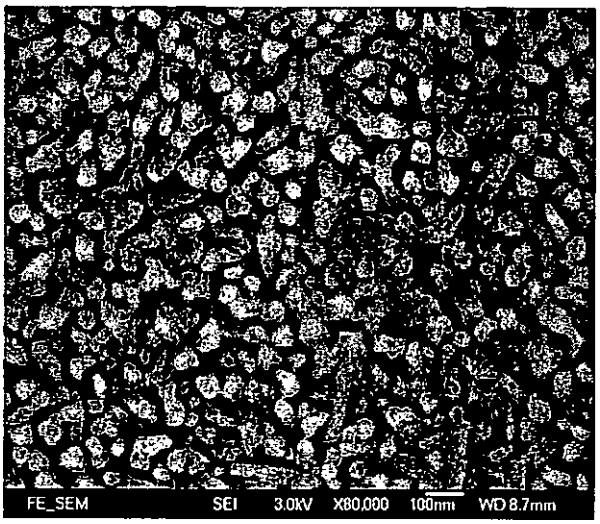

Fig. 6.1.1.2 SEM micrograph of SBN60 film grown on Si substrate annealed at 600°C.

However, because of the poor signal to noise ratio observed in the XRD measurements, small grains formed at 500°C were unable to be detected by XRD. Therefore, high-resolution TEM studies were carried out to confirm the crystallization of SBN60 films. Figures 6.1.1.3 and 6.1.1.4 show the TEM micrographs of SBN60 films annealed at 500°C and 600°C respectively. As observed in Fig. 6.1.1.3, no crystallized pattern is identified in SBN60 film, implying that the film is still amorphous. The inset in Fig. 6.1.1.3 shows a diffraction ring of the film. The ring is isotropic without any diffraction pattern, indicating again that the film is amorphous. Meanwhile, Fig. 6.1.1.4 shows the TEM micrograph of a selected area of a film annealed at 600°C. The micrograph shows a clear crystalline SBN60 region, although some parts of the film are still in amorphous phase. The inset shows a diffraction ring which has a clear diffraction pattern. Therefore, our TEM results demonstrate that the crystallization occured between 500°C and 600°C. These results are consistent with our XRD results.

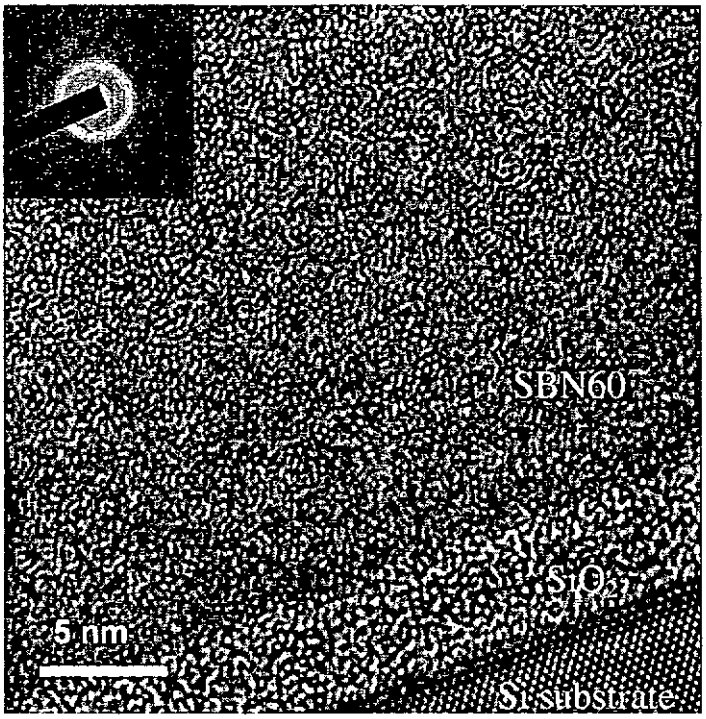

Fig. 6.1.1.3 HREM shows the microstructure of SBN60 film annealed at 500°C.

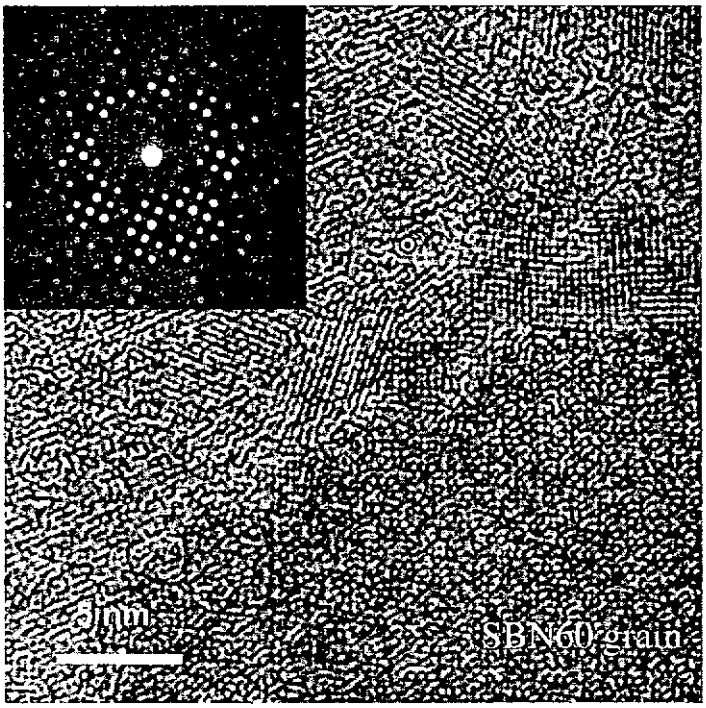

Fig. 6.1.1.4 HREM shows the microstructure of SBN60 film annealed at 600°C.

6.1.2 Modeling and Fitting

In this chapter, Lorentz model with one oscillator of the dielectric function [Harland G. Tompkins *et al*, 1999]:

$$\varepsilon(\omega) = \varepsilon_{\infty} + \frac{f\omega_0^2}{\omega_0^2 - \omega^2 + i\gamma\omega} \qquad \text{(Eq. 6.1.2.1)}$$

was used to describe the energy band gap of SBN60. The model parameters $f\omega_o^2$, ω_o and γ are the oscillator strength, resonance energy and damping rate of the oscillator, respectively. The parameter ε_{∞} represents the contributions at higher frequencies.

Similar to the fitting procedures of (1-x)PMN–xPT, single- and double-layer Lorentz models were used. Poor agreements between the experimental data and fitting results were obtained in both models. In order to have a better fit, a graded double-layer model (Fig. 6.1.2.1) was introduced. In this model, the film consists of two layers: a surface layer that composed of bulk SBN60 as well as voids, a bottom layer that linearly mixed with SBN60 and SBN60+SiO_2. Voids in the top layer are mainly caused by surface roughness and porosity resulting from evaporation of the solvent in the annealing process. In the bottom layer, we assumed that the underneath of this layer consists of pure SiO_2, meanwhile the top portion is made of pure SBN60. In between, the layer is mixed linearly with SBN60 and SiO_2. The SiO_2 in the bottom layer may be come from

the incomplete etching process or diffusion during annealing. The existence of this SiO_2 layer is confirmed in our TEM micrograph (Fig. 6.1.1.3).

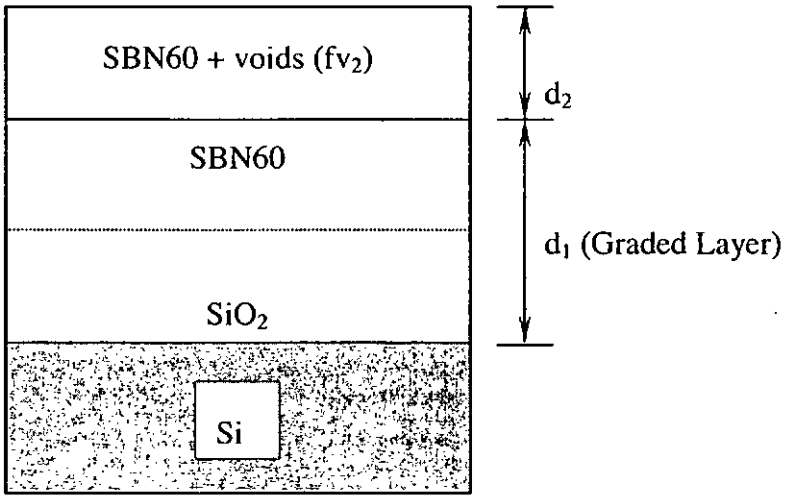

Fig. 6.1.2.1 Graded double-layer model for interpreting SBN60 film on Si. fv_2 is the void volume percentage in top layer. d_1 and d_2 are the layer thicknesses of bottom and top layers respectively.

Using this graded double-layer model to analyze the data over the spectral range of 0.75 – 3.5 eV, better fits of I_S and I_C between the simulated values and the experimental data were obtained. The solid lines in Fig. 6.1.2.2 denote these results.

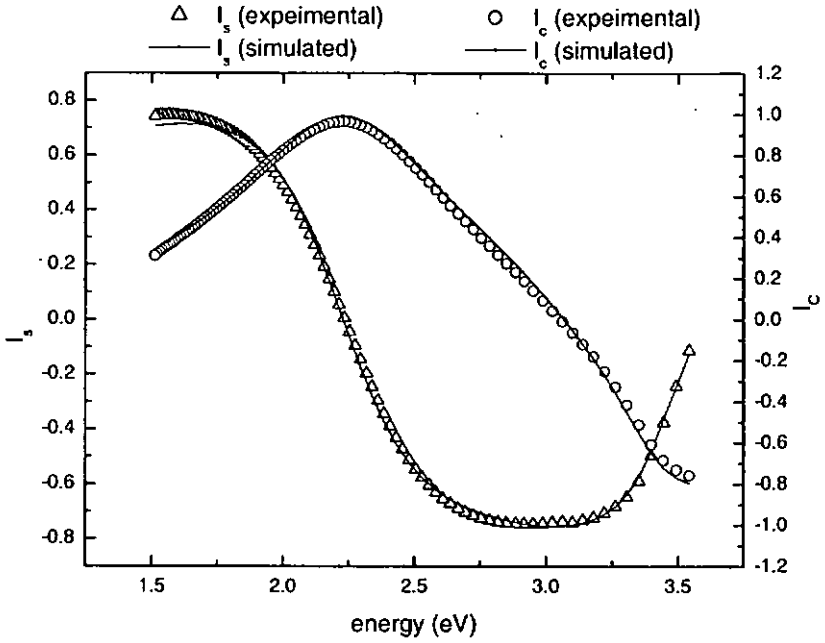

Fig. 6.1.2.2 Spectra of ellipsometric parameters I_S and I_C as functions of energy for SBN60 film annealed at 600°C using the graded double-layer Lorentz model.

Figures 6.1.2.3 and 6.1.2.4 depict the dispersion spectra of the refractive indices n and extinction coefficients k of the SBN60 films annealed at different temperatures based on the graded double-layer model. As seen in Fig.6.1.2.3, the refractive indices of the SBN60 films are general greater than that of SBN50 single crystal (n = 2.312) at 1.96 eV [Landolt-Börnstein, 1981]. These unexpected high refractive indices of SBN60 films indicate that the results are physically unreasonable and thus the model needs further modification before a better agreement is obtained.

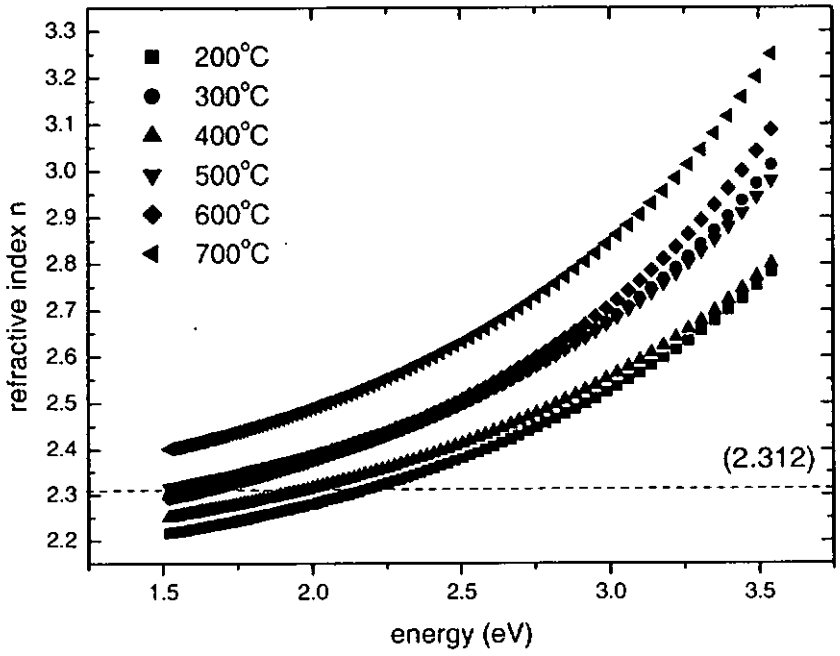

Fig. 6.1.2.3 Dispersion spectra of refractive indices of SBN60 films annealed at different temperatures. The fittings are based on the graded double-layer Lorentz model.

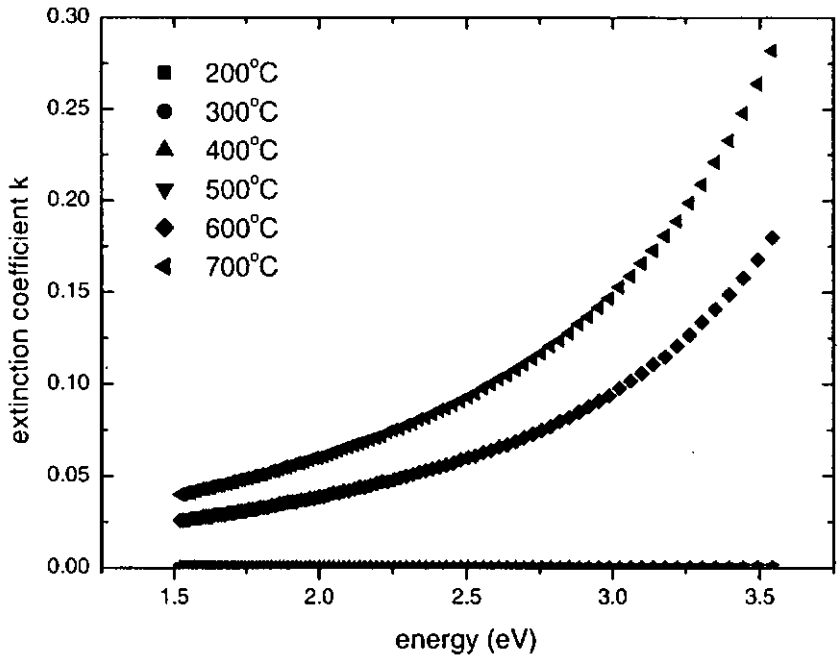

Fig. 6.1.2.4 Dispersion spectra of extinction coefficients of SBN60 films annealed at different temperatures. The fittings are based on the graded double-layer Lorentz model.

Based on this graded double-layer model (Fig. 6.1.2.1), a modified graded double-layer model was developed. The schematic diagram of this model is shown in Fig. 6.1.2.5. In this model, the film consists of two layers: a surface layer that composed of bulk SBN60 as well as voids, and a bottom layer that linearly mixed with bulk SBN60 and SBN60 plus SiO_2. The main modification, as compared to the graded double-layer model, is in the bottom portion of the graded layer. In the bottom portion, we assumed that the underneath consists of SBN60 and SiO_2, meanwhile the top portion is pure SBN60.

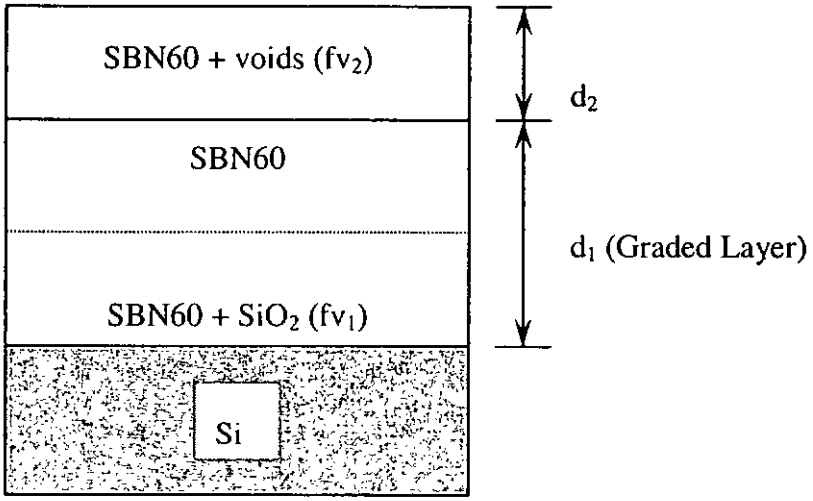

Fig. 6.1.2.5 Modified graded double-layer model for interpreting SBN60 films. fv_1 and fv_2 are the SiO_2 and the voids volume percentages in bottom and top layers respectively. d_1 and d_2 are the layer thicknesses of bottom and top layers respectively.

Although this modified graded double-layer model improved some of the fittings, it could not fit all the samples. The obtained refractive index values of the films annealed at 600°C and 700°C were still larger than that of single crystal (at 1.96 eV). Therefore, this modified graded double-layer model was altered again. A graded triple-layer model, with the schematic diagram shown in Fig. 6.1.2.6, was used. In this model, the film consists of three layers: a surface layer that composed of bulk SBN60 as well as voids, a bulk SBN60 middle layer and a bottom layer that linearly mixed with bulk SBN60 and bulk SBN60 plus SiO_2. In this graded triple-layer model, as compared to the modified graded double-layer model, a pure SBN60 layer is inserted.

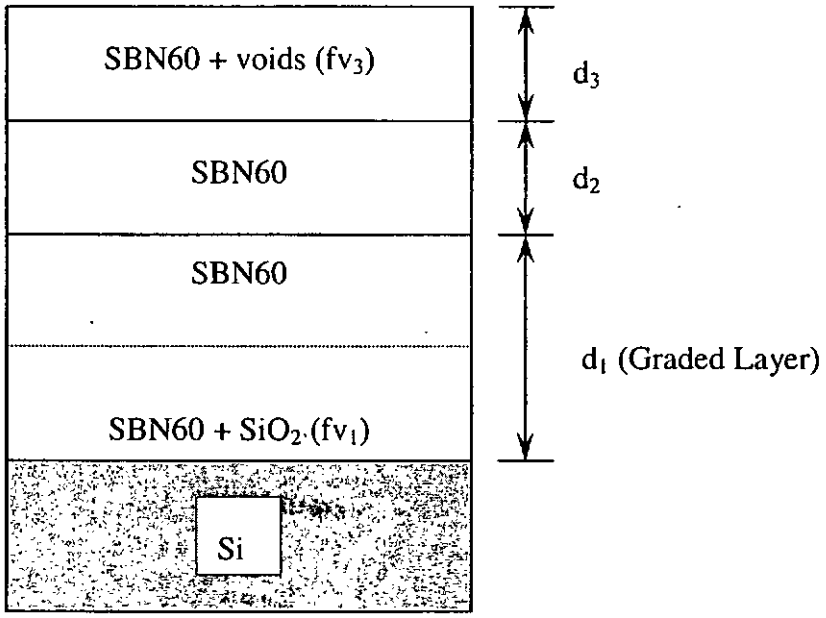

Fig. 6.1.2.6 Graded triple-layer model for interpreting the SBN60 films. fv_1 and fv_3 are the SiO_2 and the voids volume percentages in bottom and top layers respectively. d_1, d_2 and d_3 are the layer thicknesses of bottom, middle and top layers respectively.

Using this triple-layer model to analyze the data over the spectra range 0.75 – 3.5 eV, better fit results, with smaller deviation as compared with the modified double-layer model, of I_S and I_C were obtained for all the samples. The solid lines in Fig. 6.1.2.7 denote these results. Table 6.1.2.1 shows the values of the fitting parameters for SBN60 films with different annealing temperatures.

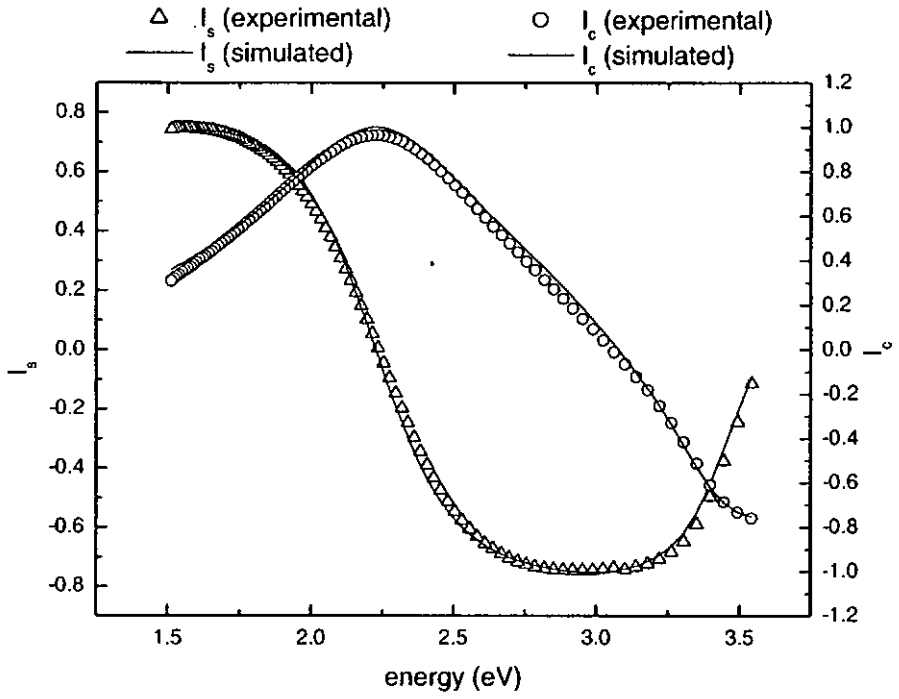

Fig. 6.1.2.7 Spectra of ellipsometric parameters I_S and I_C as functions of energy for SBN60 film annealed at 600°C using the graded triple-layer Lorentz model.

Table 6.1.2.1 Fitting parameters for SBN60 films with different annealing temperatures.

Temp/ °C	200	300	400	500	600	700
d_1 (Å)	673±82.2	661±52.4	584±37.3	646±28.0	588±20.3	605±35.2
d_2 (Å)	231±92.3	168±55.8	126±38.2	84±28.5	96±22.5	129±41.3
d_3 (Å)	89±20.1	81±1.6	123±1.1	75±2.5	70±5.8	120±13.5
fv_1 (%)	74±5.1	79±7.9	71±5.5	79±9.8	100*	100*
fv_3(%)	50±3.9	50±2.5	50±8.4	50±10.2	50±6.2	50±10.8
ε_∞	1.000±0.326	1.000±0.374	1.000±0.326	1.000±0.381	1.000±0.266	1.000±0.335
f	2.928±0.347	3.038±0.336	3.164±0.281	3.108±0.358	3.350±0.235	3.400±0.298
ω_o	5.419±0.297	5.552±0.200	5.744±0.156	5.333±0.144	4.839±0.090	4.800±0.133
γ	0.000±0.068	0.048±0.049	0.000±0.051	0.233±0.050	0.354±0.030	0.473±0.034

* The initial fitted value was 99.99 with a large 90 % confidence value. In the sequential fitting, the fv_1 (%) was fixed at 100.

Figures 6.1.2.8 and 6.1.2.9 show the dispersion spectra of the refractive indices n and extinction coefficients k of the SBN60 films derived from the graded triple-layer model. Based on this triple-layer model, the n dispersion spectra have a similar value and an energy dependency as compared with these obtained by the modified graded double-layer model for films annealed between 200°C and 500°C. For films annealed at 600°C and 700°C, however, the n dispersion spectra decrease. For example, the n values of films annealed at 600°C and 700°C at 1.96 eV are 2.238 and 2.254 respectively, which are smaller than that of single crystal SBN50. In general, n continuously increases non-linearly with photon energy over the entire range of energies with a more perceptive increase at energies above 2.5 eV. As the annealing temperature increases, the spectra of n shift upward. This indicates that the refractive index increases with annealing temperature. The upward shift is more significant around crystallization of the film, i.e. between 500°C and 600°C. This indicates that the crystallization of the SBN60 films has an important influence on the refractive index.

Furthermore, amorphous films possess a nearly zero extinction coefficient. It means that the films are transparent and no scattering as well as absorption occurs. Meanwhile, for the 600°C and 700°C films, their k spectra are fairly flat below 2.5 eV and increases more sensitively at higher energies. This behavior is typical of an insulator or semiconductor in the range of energy near the band gap. Below the band gap, transmission dominates with a tiny extinction coefficient. As the band gap energy is

approached from below, both n and k increase with k approaches a resonance characterized by the oscillator in the Lorentz model.

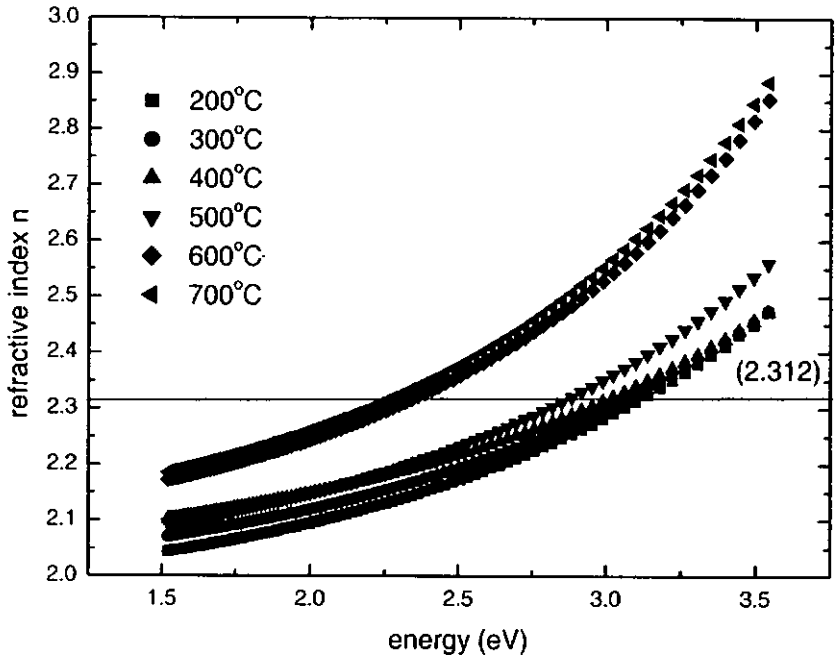

Fig. 6.1.2.8 Dispersion spectra of refractive indices of SBN60 films annealed at different temperatures. The fitting are based on the graded triple-layer Lorentz model.

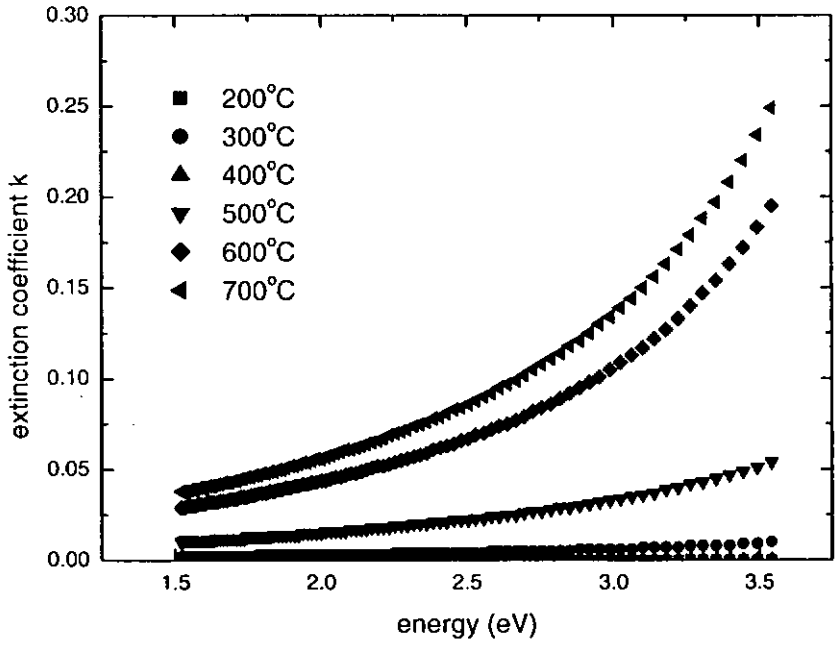

Fig. 6.1.2.9 Dispersion spectra of extinction coefficients of SBN60 films annealed at different temperatures. The fittings are based on the graded triple-layer Lorentz model.

6.1.3 Surface Morphology

In order to verify the film thicknesses obtained by SE, the surface morphology and thickness of the films were measured by scanning electron microscopy (SEM). On the other hand, surface roughness obtained by atomic force microscopy (AFM) was used to compare with the fitted parameter (d_3).

Figures 6.1.3.1 and 6.1.3.2 show the cross-section and the surface images of film annealed at 600°C obtained by SEM and AFM respectively. The thickness and root mean square (rms) roughness obtained are about 80 nm and 7.1 nm respectively. These values are close to those obtained by SE ($d_1 + d_2 + d_3$ = 75.4 nm and d_3 = 7 nm). For comparison, the films thickness ($d_1 + d_2 + d_3$) and the surface roughness (d_3) obtained by different techniques are listed in Table 6.1.3.1 and 6.1.3.2. The film thickness and roughness obtained by SE are in good agreements with those obtained by SEM and AFM. Only small deviations are obtained and this indicates that the graded triple-layer model is a reasonable description for our SBN60 films.

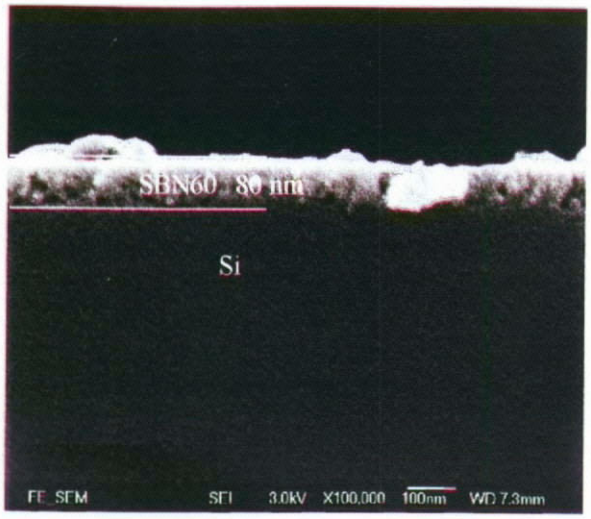

Fig. 6.1.3.1 SEM micrograph showing the cross-section of SBN60 film grown on Si substrate annealed at 600°C.

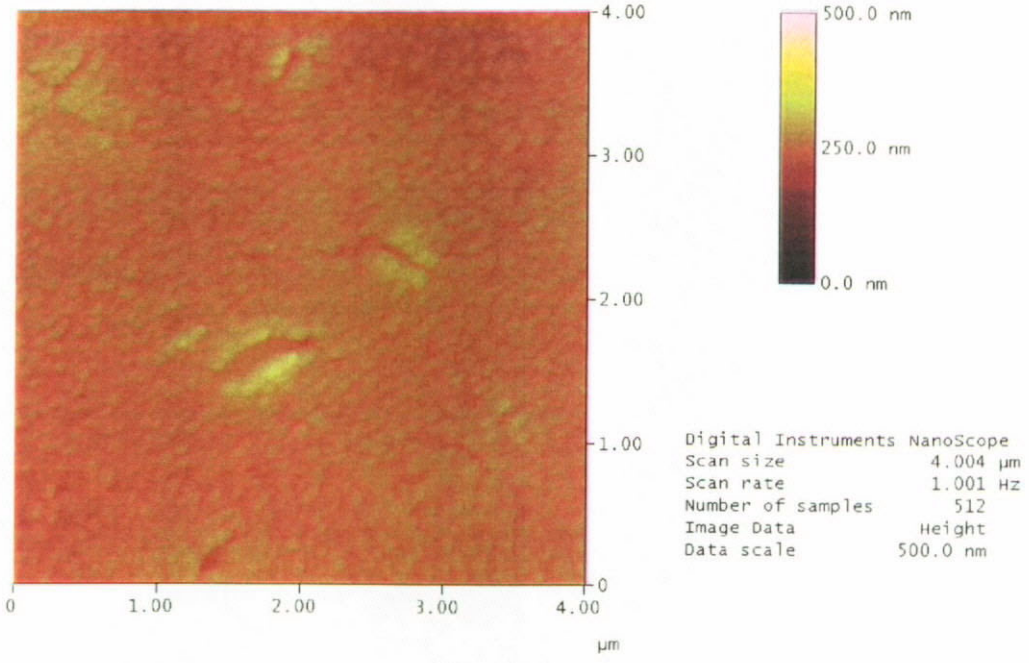

Fig. 6.1.3.2 AFM images of SBN60 film grown on Si substrate annealed at 600°C.

Table 6.1.3.1 Film thicknesses of SBN60 films obtained by SE and SEM.

Annealing Temperature/ °C	SE $d_1 + d_2 + d_3$ (nm)	SEM d (nm)	% Error $\left(1 - \frac{SE\ \ d_1 + d_2 + d_3}{SEM\ \ d}\right) \times 100\%$
200	99.3	100	0.7
300	91.0	98	7.1
400	83.3	82	1.6
500	80.5	79	1.9
600	75.4	80	5.8
700	85.4	90	5.1

Table 6.1.3.2 Surface roughness of SBN60 films obtained by SE and AFM.

Annealing Temperature/ °C	SE d_3 (nm)	AFM d (nm)	% Error $\left(1 - \frac{SE\ \ d_3}{AFM\ \ d}\right) \times 100\%$
200	8.9	8.3	7.2
300	8.1	7.9	2.5
400	12.3	12.0	2.5
500	7.5	7.9	5.1
600	7.0	7.1	1.4
700	12.0	11.9	0.8

6.2 ANNEALING DURATION DEPENDENCE

Apart from annealing temperature, the effects of annealing duration on the optical properties of the sol-gel SBN60 films were also studied. Based on our previous results, the highest refractive index was obtained at an annealing temperature of 700°C. Therefore, in this study, we fixed the annealing temperature at 700°C and varied the annealing duration from 30 min up to 600 min.

6.2.1 Fabrication and Structural Characterization

Unless stated otherwise, the following fabrication conditions were employed in all cases. The sol solution had a concentration of 0.16 M and was spin-coated on 1×1 cm^2 (001)Si substrates using a spin coater operated at 3000 rpm for 30 s. After drying for several seconds on a hot plate at about 150°C, the films were annealed at 700°C for different annealing durations of 30 min, 90 min, 120 min, 150 min, 300 min and 600 min.

XRD θ-2θ profiles of these SBN60 films on Si substrates annealed at different durations are shown in Fig. 6.2.1.1. From the figure, it was noticed that peaks corresponding to the SBN60 tetragonal tungsten-bronze (TTB) phase were identified in all films. As expected, the films are polycrystalline.

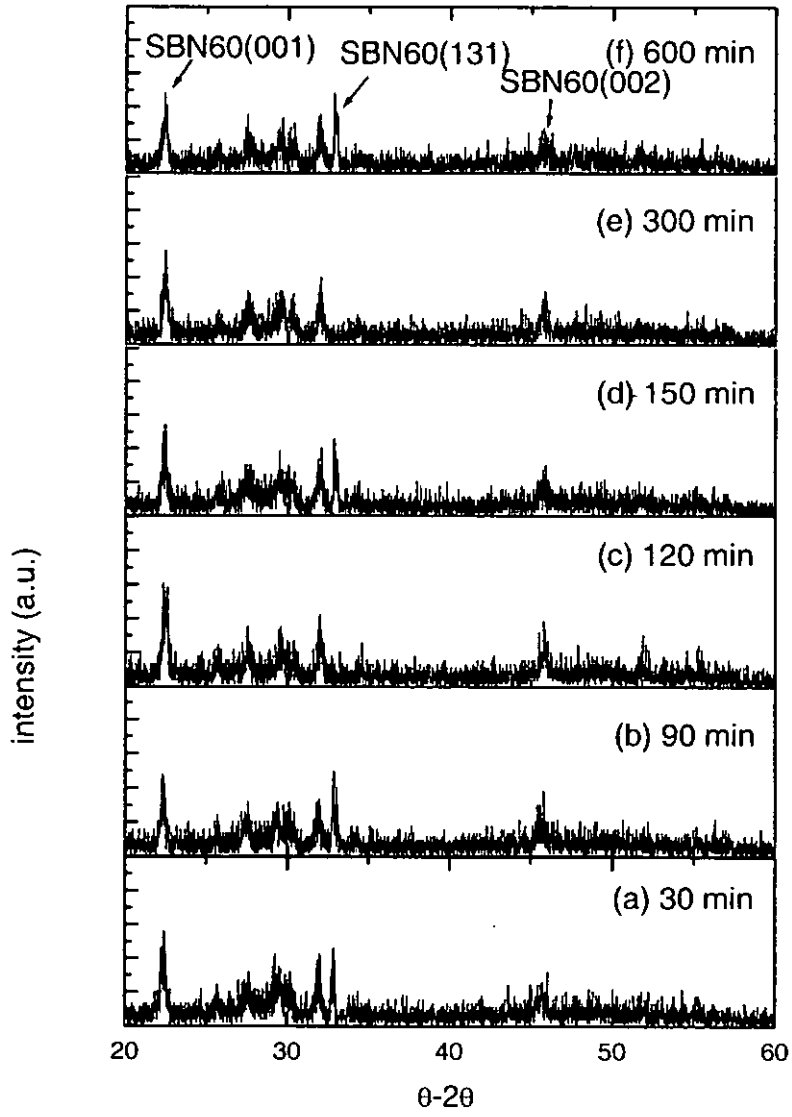

Fig.6.2.1.1 XRD θ-2θ scans of the SBN60 films annealed at 700°C with different annealing durations.

Figures 6.2.1.2 and 6.2.1.3 show the top view SEM images of samples annealed for 30 min and 600 min respectively. SEM micrographs reveal that all SBN60 film surfaces are, in general, dense, smooth and crack-free. The surface of the 30 min film has grainy (about 100 nm) microstructures. Pores (about 10 nm) at grain boundaries, probably caused by solvent evaporation, are clearly observed. The top layer of the 600 min film has similar features as these observed in the 30 min film and only shows an increase in grain size. This grain enlargement is probably due to coalescence of smaller grains resulting in a larger pore size at grain boundaries.

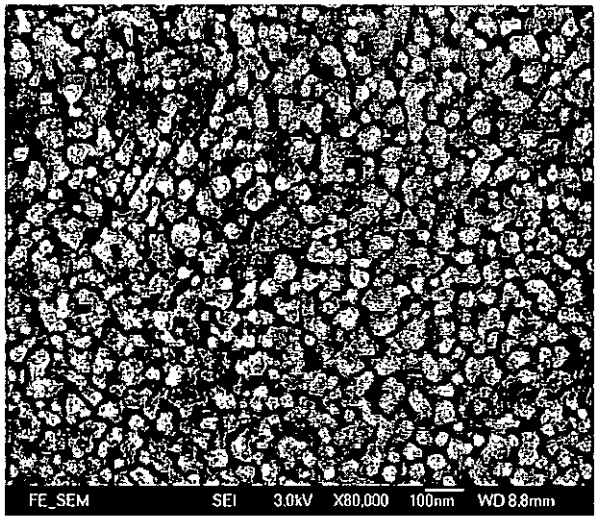

Fig. 6.2.1.2 SEM micrograph of SBN60 film grown on Si substrate annealed 700°C for 30 min.

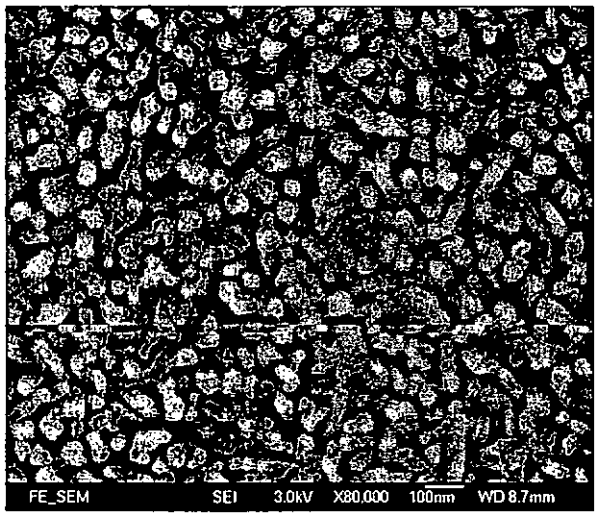

Fig. 6.2.1.3 SEM micrograph of SBN60 film grown on Si substrate annealed 700°C for 600 min.

6.2.2 Modeling and Fitting

Similar to previous section, the graded triple-layer model was used. To analyze the data over the spectra range of 0.75 – 3.5 eV. Good fits of I_S and I_C between the simulated values and the experimental data were obtained. The solid lines in Fig. 6.2.2.1 denote these results. Table 6.2.2.1 shows the values of fitting parameters for different SBN60 films.

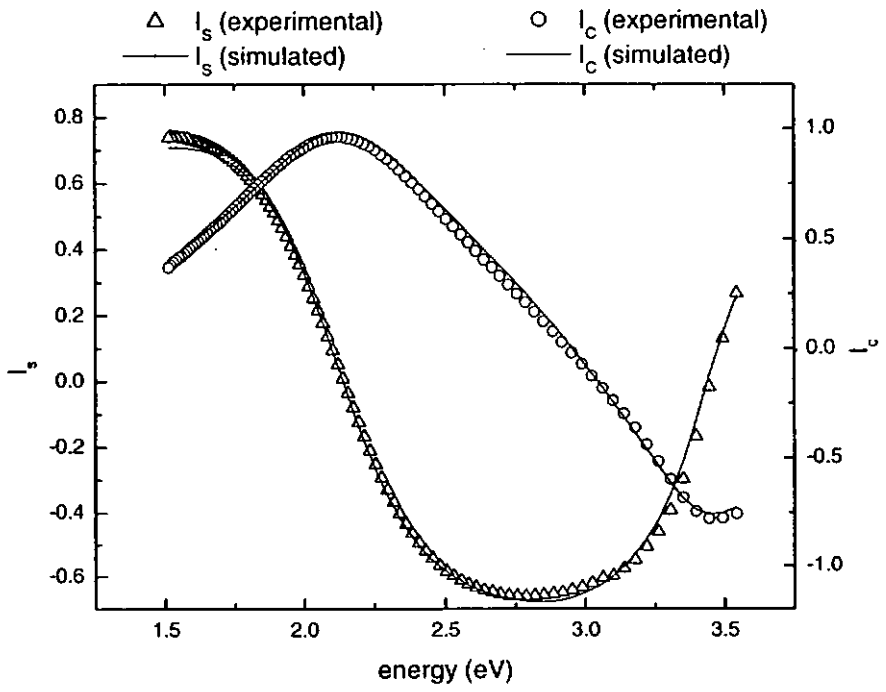

Fig. 6.2.2.1 Spectra of ellipsometric parameters I_S and I_C as functions of energy for SBN60 film annealed at 700°C for 150 min.

Table 6.2.2.1 Fitting parameters for SBN60 films with different annealing durations.

Duration	30 min	90 min	120 min	150 min	300 min	600 min
d_1 (Å)	553±37.0	389±47.8	605±35.2	602±21.8	538±31.0	634±32.8
d_2 (Å)	153±58.7	358±54.9	129±41.3	101±23.8	97±39.8	156±43.0
d_3 (Å)	170±42.7	95±16.4	120±13.5	95±10.5	170±44.6	100±25.8
fv_3 (%)	15±4.3	53±3.7	50±10.8	50±4.5	13±3.2	13±3.5
ε_∞	1.160±0.389	1.000±0.482	1.000±0.335	1.000±0.247	1.000±0.406	1.000±0.409
S_1	82.63±0.724	85.52±0.947	78.34±0.564	78.92±0.421	79.67±0.742	78.23±0.682
ω_{o1}	5.108±0.197	5.086±0.269	4.800±0.133	4.773±0.101	4.784±0.187	4.768±0.170
γ_1	0.450±0.056	0.463±0.055	0.473±0.034	0.503±0.028	0.701±0.048	0.749±0.046

Figures 6.2.2.2 and 6.2.2.3 plot the dispersion spectra of the refractive indices n and extinction coefficients k of the SBN60 films derived from the graded triple-layer model.

As shown in Fig. 6.2.2.2, n increases non-linearly with photon energy over the entire range of energies with a more receptive increase at energies above 2.5 eV. The dispersion curves are divided into two groups. For 30 min and 90 min films the values of n are lower than those of the other films, while the n values seem to be the same for 120 min, 150 min, 300 min and 600 min films. On the basis of these results, it is concluded that the annealing time has a mild influence on the optical properties of sol-gel SBN60 films. As far as the annealing time is equal to or longer than 120 min, no observable change in the refractive index is detected in sol-gel derived SBN60 film. However, a slightly different result was obtained in extinction coefficients. The k dispersion curves are divided into three groups as compared to two groups in n dispersion curves. The 30 min and 90 min films have the lowest extinction coefficients. Then the 120 min and 150 min films have a slightly larger extinction coefficient. Finally, the 300 min and 600 min films have the largest extinction coefficient. This increase in extinction coefficient is probably due to the grain scattering. In general, for waveguide applications, films with a high refractive index and a low extinction coefficient are required. Hence, our results show that the optimum annealing time is about 150 min.

As observed in Fig.6.2.2.3, the spectra of k are fairly flat below 2.5 eV and increases more sensitively at higher energies. This behavior is typical of an insulator or semiconductor in the range of energy near the band gap. Below the band gap, transmission dominates with a tiny extinction coefficient. As the band gap energy is approached from below, both n and k increase with k approaches a resonance characterized by the oscillator in the Lorentz model. It indicates that k is getting steeper toward higher photon energy with annealing duration.

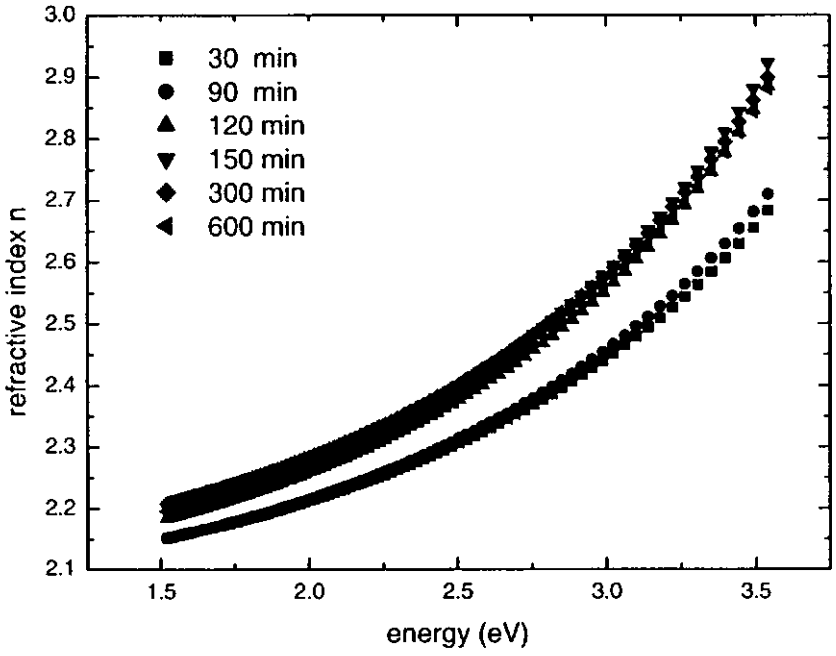

Fig. 6.2.2.2 Dispersion spectra of refractive indices of SBN60 films with different annealing durations. The fittings are based on the graded triple-layer Lorentz model.

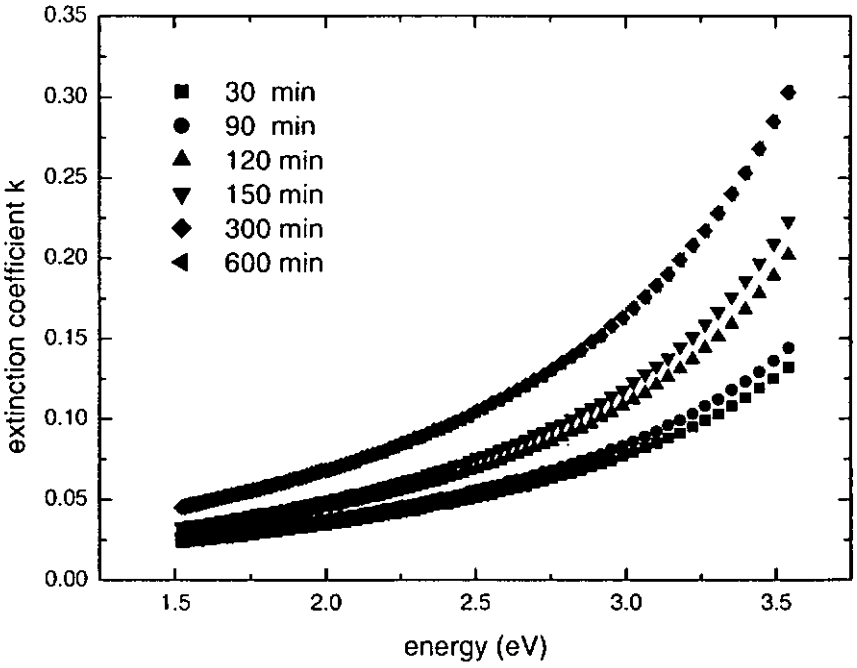

Fig. 6.2.2.3 Dispersion spectra of extinction coefficients of SBN60 films with different annealing durations. The fitting are based on the graded triple-layer Lorentz model.

6.2.3 Surface Morphology

In order to verify the thickness profile of SBN60 films obtained by SE, the thickness of films were obtained by using cross-section images of scanning electron microscopy (SEM). Moreover, the surface roughness was characterized by using atomic force microscopy (AFM).

Figures 6.2.3.1 and 6.2.3.2 show cross-section and surface profiles of the sample annealed for 150 min respectively. The thickness and root mean square (rms) roughness are about 84 nm and 9.4 nm respectively. These values are very close to those obtained by SE ($d_1 + d_2 + d_3 = 79.8$ nm and $d_3 = 9.5$ nm). For comparison, the films thickness and the surface roughness obtained by different techniques are listed in Table 6.2.3.1 and 6.2.3.2. As noticed in the Tables, the film thickness and roughness obtained by SE are in good agreements with those obtained by SEM and AFM.

Fig. 6.2.3.1 SEM micrograph showing the cross-section of SBN60 film grown on Si substrate annealed at 700°C for 150 min.

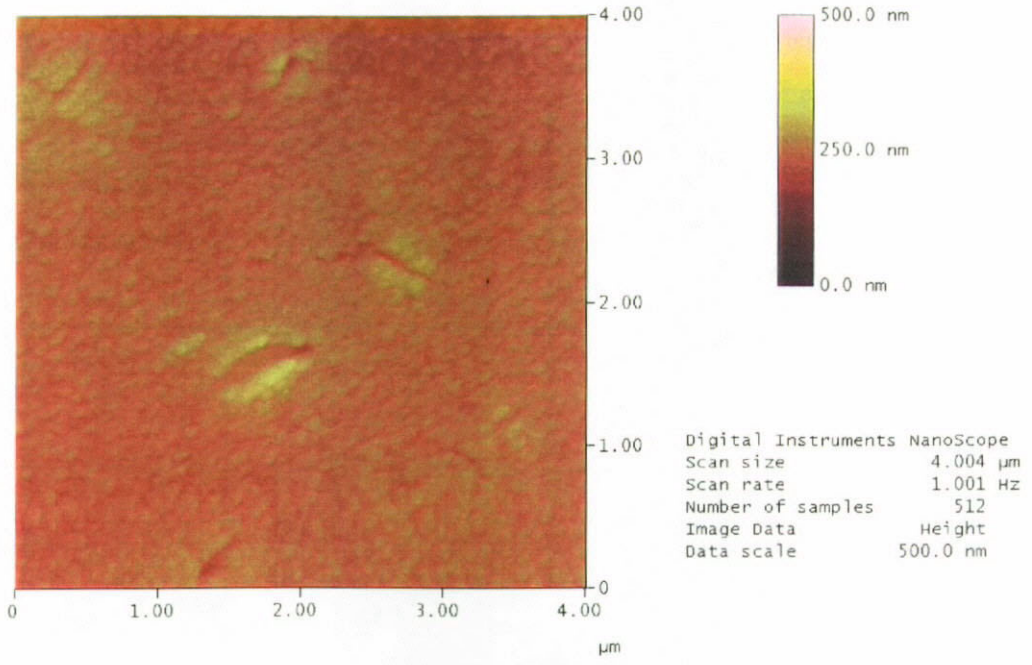

Fig. 6.2.3.2 AFM micrograph of SBN60 film grown on Si substrate annealed at 700°C for 150 min.

Table 6.2.3.1 Film thickness of SBN60 films obtained by SE and SEM.

Annealing Duration / min	SE $d_1 + d_2 + d_3$ (nm)	SEM d (nm)	% Error $\left(1-\frac{SE\ (d_1+d_2+d_3)}{SEM\ \ d}\right)\times 100\%$
30	87.5	94	6.9
90	84.2	88	4.3
120	85.4	90	5.1
150	79.8	79	1.0
300	80.5	88	8.5
600	89.0	88	1.1

Table 6.2.3.2 Surface roughness of SBN60 films obtained by SE and AFM.

Annealing Duration / min	SE d_3 (nm)	AFM d (nm)	% Error $\left(1-\frac{SE\ (d_3)}{AFM\ \ d}\right)\times 100\%$
30	17	16.3	4.3
90	9.5	9.4	1.1
120	12	11.9	0.8
150	9.5	9.4	1.1
300	17	17.8	4.5
600	10	10.2	2.0

CHAPTER 7 CONCLUSIONS AND FUTURE WORK

7.1 CONCLUSIONS

(1-x)PMN–xPT films with x = 0, 0.1, 0.3, 0.35 and 0.4 have been fabricated on MgO single crystal substrates by PLD. Spectroscopic ellipsometer (SE) was used to characterize the depth-profile and refractive index of these films. It is found that the refractive index of (1-x)PMN–xPT films increases with PT content. Meanwhile, the extinction coefficient of (1-x)PMN–xPT film is small in the visible region and increases as the energy increases. The surface roughness and the film thickness obtained from double-layer Lorentz model are consistent with those measured by SEM and AFM. The transmittance results show that the optical band gap energy of (1-x)PMN–xPT film is composition-dependent and decreases with PT content. A reduced band gap with higher PT content leads to a higher refractive index at energies below the gap for films with higher PT content.

The refractive index of 0.65PMN–0.35PT films was maximized at a deposition temperature of 670°C and decreased at higher deposition temperature. Its extinction coefficient is the largest at a temperature of 710°C. The surface roughness and the film thickness of the films obtained from double-layer Lorentz model are consistent with those measured by SEM and AFM. The transmittance results show that the change in

the optical band gap energy of 0.65PMN–0.35PT films of different deposition temperatures is less sensitive as compared to that of composition.

On the other hand, for SBN60 ($Sr_{0.6}Ba_{0.4}Nb_2O_6$) films, SE measurements also revealed that the refractive indices of SBN60 films increase with annealing temperature. The increase is more significant at around the crystallization temperature of the films, i.e. between 500°C and 600°C. The extinction coefficients also possess a similar trend showing zero values for amorphous films and large values (for example, 0.1 at 2.5 eV) for films annealed above 600°C. Our results demonstrate that the crystallization of the films has an important influence on the refractive index as well as extinction coefficient. Although crystallization can raise the refractive index of the film because of the film densification, it also promotes grain scattering due to larger grain size. Similar phenomena are confirmed by annealing the films for different durations.

7.2 FUTURE WORK

Although several processing parameters (deposition temperature, annealing temperature and annealing duration) have been varied in order to investigate the effects on the optical properties of ferroelectric films, there are still a lot of different processing parameters needed to be studied. For examples, (i) the choice of substrate, because different substrates will lead to different degree of lattice mismatching, etc. (ii) the heating rate of the annealing process which affects the grain size of the samples. The other direction is to study epitaxial SBN60 films grown on Si substrate and its optical

properties. However, epitaxial SBN60 films cannot be fabricated directly on Si substrate. This may be due to polar (SBN60) on non-polar growth (Si is a non-polar substrate). In order to overcome this problem, buffer layers have to be employed.

REFERENCES

Adachi H., Mitsuyu T., Yamazaki O. and Wasa K., J. Appl. Phys., **60** (1986) 736

Aspnes D. E., Theeten J. B. and Hottier F., Phys. Rev. B, **20** (1979) 3292

Azzam R. M. A. and Bashara N. M., Ellipsometry and Polarized Light, North-Holland, Amsterdam (1977)

Beerman H. P., Ferroelectrics, **2** (1971) 123

Bing Y. H., Guo R. and Bhalla A. S., Ferroelectric, **242** (2000) 1

Bruggeman D. A. G., Ann. Phys. (Leipzig), **24** (1935) 636

Chen C. J., Xu Y., Xu R. and Mackenzie J. D., J. Appl. Phys., **69** (1991) 1763

Choi S. W., Shrout T. R., Jang S. J. and Bhalla A. S., Ferroelectrics, **100** (1989) 29

Crewe A. V., J. Microsc., **100** (1974) 247

Cross L. E., Ferroelectrics, **76** (1987) 241

Devore J., Probability and Statistics for Engineering and the Sciences, Monterey CA: Brooks/ Cole, (1982) 640

DiDomenico M. J. and Wemple S. H., J. Appl. Phys., **40** (1969) 720

Fox G. R. and Krupanidhi S. B., Mater J. Res., **7** (1992) 3039

Frederick Wooten, Optical Properties of Solid (Academic Press, New York and London, 1972) 43

Fujita H., Ura K., Mori H. (eds.) Ultramicropy, **39** (1991) 1

Glass A. M., J. Appl. Phys., **40** (1969) 4699

Glass A. M., J. Appl. Phys., **41** (1970) 2268

Glass A. M., Science, **235** (1987) 1001

Haertling G. H. and Land C. E., J. Am. Ceram. Soc., **54** (1971) 1

Harland G. Tompkins and William A. McGahan, Spectroscopic Ellipsometry and Reflectometry: a user's guide (1999)

Jaffe B., Cook Jr. W. R. and Jaffe H., Piezoelectric Ceramics, (Academic Press, New York, 1971) 213

Jamieson P. B., Abrahams S. C. and Bernstein J. L.: J. Chem. Phys., **48** (1968) 5048

Jesperson S. N. and Schnatterly S. E., Rev. Sci. Instrum., **40** (1969) 761

Jobin Yvon-Spex Instrumrnts S.A., Inc., User Handbook: DeltaPsi 2

Koh J., Lu Y., Wronski C. R., Kuang Y., Collins R. W., Tsong T. T. and Strausser Y. E., Appl. Phys. Lett., **69** (9), (1996) 1297

Landolt-Börnstein, Ferroelectric and Related Substances (Springer-Verlag, Berlin, 1981) 16

Li J. -F. and Viehland D., J. Appl. Phys., **80** (1996) 3451

Li S. T., Liu G. K., Liu H. and Fernandez F. E., J. Alloys Compd. **303-304** (2000) 360

Lu Y. H., Wang F. L., Wang S. –Q., Appl. Phys. Lett., **74**, 20 (1999) 3038

Lu Y. H., Zheng J. J., Wang F. L., Appl. Phys. Lett., **74**, 25 (1999) 3764

Mah S. B., Jang N. W., Park J. H., Paik D. S. and Park C. Y., Materials Research Bulletin, **35** (2000) 1113

Maria J. P., Hackenberger and Trolier-Mckinstry W. S., J. Appl. Phys., **84** (1998) 5147

Maxwell Garnett J. C., Philos. Trans. R. Soc. London, **203** (1904) 385

McHenry D. A., Giniewicz J. R., Shrout T. R., Jang S. J. and Bhalla A. S., Ferroelectric, **102** (1990) 160

McHenry D. A., Ph. D. thesis, The Penn. State University, (1992)

Nagarajan V., Alpay S. P., Ganpule C. S., Nagaraj B. K., and Aggarwal S., Appl. Phys. Lett. **77**, 3 (2000) 438

Neurgaonkar R. R. and Cory W. K., J. Opt. Soc., Am. B, Opt. Phys., **3** (1986) 274

Neurgaonkar R. R., Kalisher M. H., Lim T. C., Staples E. J. and Keester K. I., Mater. Res. Bull., **15** (1980) 1235

Newnham R. E., Udayakumar K. R., and Trolier Mckinstry S., Chemical Processing of Advanced Materials, Hench L. L. and West J. K., eds., (1997)

Noblanc O., Guacher P. and Calvarin G., J Appl. Phys., **79** (1996) 4291

Nystrom M. J., Weesels B. W., Lin W. P., Wong G. K., Neumayer D. A. and Marks T. J., Appl. Phys. Lett., **66** (1995) 1726

Park J. H., Kim B. K., Song K. H., and Park S. J., Materials Research Bull., **30** (1995) 435

Prokhorov A. M. and Kuz'minov Y. S., Ferroelectric Crystals for Laser Radiation Control, (Adam Hilger, Bristol), (1991) 81

Repelin Y., Husson E. and Brusset H., Spectrochimica Acta, **35** (1979) 937

Shirane G. and Hoshino S., J. Phys. Soc. Jpn., **6** (1951) 265

Shrout T. R., Chang Z. P., Kim N. and Markgraf S., Ferroelectrics, **229** (1990) 223

Smolensky G. A., J. Phys. Soc. Jpn., **28** (1970) 26

Stephens R. E. and Maalitson I. H., J. Nat. Bur. Stand., **49** (1952) 249

Swartz S. L., Shrout T. R., Schulze W. A. and Cross L. E., J. Am. Ceram. Soc., **67** (1984) 311

Tantigate C., Lee, J. and Safari A., Appl. Phys. Lett., **66** (1995) 1611

Tauc J. C., Optical Properties of Solids (North-Holland, Amsterdam, 1972) 372

Thöny S. S., Youden K. E., Harris, Jr. J. S. and Hesselink L., Appl. Phys. Lett., **65** (1994) 2018

Tian H. Y., Luo W. G., Pu X. H., He X. Y., Qiu P. S., Ding A. L., Yang S. H. and Mo D., J. Phys.: Condens. Matter, **13** (2001) 4065

Tyunina M., Levoska J., Sternberg A. and Leppävuori S., J. Appl. Phys., **86**, 9 (1999) 5179

Uchino K., Ceramics Bulletin, **65** (1986) 647

Uchino K., Ceramics International, **21** (1995) 309

Udayakumar K. R., Schuele D. J., Chen J., Krupanidhi S. B. and Cross L. E., J. Appl. Phys., **77** (1995) 3981

VanDamme N. S., Sutherland A. E., Jones L., Bridger K. and Winzer S. R., J. Am. Ceram. Soc., **74** (1991) 1785

Volk T. R., Kovalevich V. I. and Kuzminov Yu S., Ferroelectrics, **22** (1978) 659

Wu A. Y., Wang F., Juang C. -B., Bustamante C., Yeh H. -Y. and Diels J. C., IEEE 7th International Symposium on the Applications of Ferroelectrics, (1990) 135

Xu R., Xu Y., Chen C. J. and Mackenzie J. D., J. Mater. Res., **5** (1990) 916

Xu Y., Ferroelectric Materials and Their Applications, North-Holland, Amsterdam, The Netherlands, (1991) 254

Xu Y., Chen C. J., Xu R. and Mackenzie J. D., Phys Rev. B., **44** (1991) 35

Zeinally A. H., Lebedeva N. N., Agaronov B. C. and Sheinkman M. K., Ferroelectrics, **18** (1978) 141

Zhdanov V. G., Spencer E. G. and Ballman A. A., Appl. Phys. Lett., **11** (1967) 23